



HAL
open science

Ultra-high carrier modulation in two dimensions through space charge doping: graphene and zinc oxide

Andrea Paradisi

► **To cite this version:**

Andrea Paradisi. Ultra-high carrier modulation in two dimensions through space charge doping: graphene and zinc oxide. Physics [physics]. Université Pierre et Marie Curie - Paris VI, 2016. English. NNT : 2016PA066297 . tel-01467077

HAL Id: tel-01467077

<https://theses.hal.science/tel-01467077>

Submitted on 14 Feb 2017

HAL is a multi-disciplinary open access archive for the deposit and dissemination of scientific research documents, whether they are published or not. The documents may come from teaching and research institutions in France or abroad, or from public or private research centers.

L'archive ouverte pluridisciplinaire **HAL**, est destinée au dépôt et à la diffusion de documents scientifiques de niveau recherche, publiés ou non, émanant des établissements d'enseignement et de recherche français ou étrangers, des laboratoires publics ou privés.

**THÈSE DE DOCTORAT DE
L'UNIVERSITÉ PIERRE ET MARIE CURIE**

Spécialité

Physique

École Doctorale de Physique et Chimie des Matériaux - ED 397

Présentée par

Andrea PARADISI

Pour obtenir le grade de

DOCTEUR de l'UNIVERSITÉ PIERRE ET MARIE CURIE

Sujet de la thèse :

**Ultra-high carrier modulation in two
dimensions through Space Charge Doping:
graphene and zinc oxide**

Dirigée par Abhay SHUKLA

Soutenue le 3 novembre 2016

devant le jury composé de :

| | | | |
|-----------------|------------------------|--|--------------------|
| M ^{me} | Sophie GUERON | Université Paris-Sud | Rapportrice |
| M. | Javier VILLEGAS | Unité Mixte de Physique CNRS/Thales | Rapporteur |
| M. | Massimiliano MARANGOLO | INSP - UPMC | Examineur |
| M. | Luca PERFETTI | École Polytechnique | Examineur |
| M. | Abhay SHUKLA | IMPMC - UPMC | Directeur de thèse |

“Troveremo una soluzione!”

Sig. Bontempi

Acknowledgements

Versione italiana

Vorrei ringraziare prima di tutti il Professor Abhay Shukla. Grazie a lui ho avuto la possibilità di fare prima lo stage e successivamente il dottorato all'UPMC. Nei quasi quattro anni di lavoro insieme ho imparato moltissime cose da lui e ricevuto il massimo sostegno, specialmente nei momenti più difficili. Ha rappresentato per me un vero esempio da seguire. Abbiamo discusso di molte cose ma soprattutto ci siamo divertiti nel fare ricerca, e questa è una cosa che non dimenticherò mai.

Ringrazio anche tutto il mio team, a partire da Johan Biscaras per tutto ciò che mi ha insegnato e per il lavoro fatto insieme per tre anni; ringrazio Zhesheng Chen, per l'aiuto in laboratorio e per il tempo passato insieme; un ringraziamento particolare va a Edoardo Sterpetti, che non esito a definire un amico ritrovato, ma anche un valido e fidato collega di lavoro che mi ha aiutato sia nel mio lavoro di tesi sia nel sollevare pesi. Ringrazio di cuore anche Mario Dagrada, il migliore dei compagni d'ufficio ma soprattutto un grande amico. Ringrazio tutti i miei colleghi dell'IMPMC, in particolare Guilherme Ribeiro e tutti gli altri dottorandi.

Ringrazio tutti gli amici Paridini che hanno contribuito (e continueranno a farlo) a rendere la mia vita parigina un po' più italiana: Alessandro, Giulio e Serena, Luca, Flavia. Ovviamente ringrazio Achille. Potrei scrivere varie pagine di ringraziamenti per lui ma mi limito a dire solamente "sei un zozzo, sei un delinquente". Grazie anche ad Andrea, amico sempre presente ma purtroppo lontano.

Ringrazio la famiglia di Francesca che, oltre ad accogliermi in casa loro come un figlio, mi hanno sempre sostenuto e incoraggiato.

Ringrazio con tutto il cuore i miei genitori e le mie sorelle. Nonostante qualche incomprensione in passato ho sempre ricevuto il massimo affetto e sostegno da tutti loro ed è sicuramente merito loro se sono arrivato fin qui oggi.

Infine, il mio ringraziamento più grande va a Francesca, non solo per il

suo grande sacrificio di trasferirsi a Parigi, ma anche per tutto il supporto, la pazienza e l'amore che mi dimostra ogni giorno.

English version

First of all, I want to thank Professor Abhay Shukla. He gave me the opportunity to do the internship and the Ph.D. at the UPMC university. In the almost four year we worked together I learned many things from him and received all his support, especially in the most difficult times. He was for me a real example to follow. We discussed about many things, but most importantly we had fun doing scientific research, which is something I'll never forget.

I thank all my team, starting from Johan Biscaras for the things I learned from him and for the work done together for three years; I thank Zhesheng Chen, for his help in the laboratory and the time we passed together; a special thank goes to Edoardo Sterpetti, which I don't hesitate to define an rediscovered friend, but also a valuable and trusted colleague who helped me with my work but also in lifting weights. I deeply thank Mario Dagrada, a great officemate but most of all a great friend. I thank all my colleagues from the IMPMC institute, in particular Guilherme Ribeiro and all the other Ph.D. students.

I thank all the Paridini friends who contributed (and will continue to contribute) to make my life in Paris a little more Italian: Alessandro, Giulio and Serena, Luca, Flavia. I obviously thank Achille. I could write many pages of acknowledgements for him but I will only say "sei un zozzo, sei un delinquente". Thanks to Andrea, a friend always present but unfortunately far.

I thank Francesca's family who welcomed me as a son and have always supported and encouraged me.

I thank my parents and my sisters with all my hearth. Despite some misunderstanding in the past I have always received love and support from all of them and it is surely thanks to them that I'm here today.

Finally, my biggest thanks goes to Francesca, not only for her sacrifice to move in Paris, but also for her support, patience and love that she shows me every day.

Abstract

English version

Carrier modulation is an important parameter in the study of the electronic phase transitions and the electronic properties of materials and at the basis for many applications in microelectronics. The tuning of charge carrier density (doping) can be achieved chemically, by adding foreign atoms to the crystal structure of the material or electrostatically, by inducing a charge accumulation like in a Field Effect Transistor device. The latter method is reversible and particularly indicated for use in two dimensional (2D) materials or ultra-thin films.

Space Charge Doping is a new technique invented and developed during this thesis for the electrostatic doping of such materials deposited on a glass surface. A space charge is created at the surface by causing sodium ions contained in glass to drift under the effect of heat and an external electric field. This space charge in turn induces a charge accumulation in the material deposited on the glass surface which can be higher than 10^{14} cm^{-2} . Detailed characterization using transport, Hall effect, Raman and AFM measurements shows that the doping is reversible, ambipolar and does not induce chemical changes. It can be applied to large areas as shown with CVD graphene.

In a second phase the space charge doping method is applied to polycrystalline ultra-thin films ($< 40 \text{ nm}$) of ZnO_{1-x} . A lowering of sheet resistance over 5 orders of magnitude is obtained. Low temperature magneto-transport measurements reveal that doped electrons are confined in two dimensions. A remarkable transition between weak localization and anti-localization is observed as a function of doping and temperature and conclusions are drawn concerning the scattering phenomena governing electronic transport under different conditions in this material.

Version française

La modulation de la densité de charge est un aspect important de l'étude de les transitions de phase électroniques ainsi que des propriétés électroniques des matériaux et il est à la base de plusieurs applications dans la micro-électronique. L'ajustement de la densité des porteurs de charge (dopage) peut être fait par voie chimique, en ajoutant des atomes étrangers au réseau cristallin du matériau ou électrostatiquement, en créant une accumulation de charge comme dans un Transistor à Effet de Champ. Cette dernière méthode est réversible et particulièrement appropriée pour les matériaux bidimensionnels (2D) ou pour des couches ultra-minces.

Le Dopage par Charge d'Espace est une nouvelle technique inventée et développée au cours de ce travail de thèse pour le dopage électrostatique de matériaux déposés sur la surface du verre. Une charge d'espace est créée à la surface en provoquant le mouvement des ions sodium présents dans le verre sous l'effet de la chaleur et d'un champ électrique extérieur. Cette charge induit une accumulation de charge dans le matériau déposé sur la surface du verre, ce qui peut être supérieure à 10^{14} cm^{-2} . Une caractérisation détaillée faite avec mesures de transport, effet Hall, mesures Raman et mesures de Microscopie à Force Atomique (AFM) montrent que le dopage est réversible, bipolaire et il ne provoque pas des modifications chimiques. Cette technique peut être appliquée à des grandes surfaces, comme il est montré pour le cas du graphène CVD.

Dans une deuxième partie le dopage par espace de charge est appliqué à des couches ultra-minces ($< 40 \text{ nm}$) de ZnO_{1-x} . Le résultat est un abaissement de la résistance par carré de 5 ordres de grandeur. Les mesures de magnéto-transport faites à basse température montrent que les électrons dopés sont confinés en deux dimensions. Une transition remarquable de la localisation faible à l'anti-localisation est observée en fonction du dopage et de la température et des conclusions sont tirées à propos des phénomènes de diffusion qui gouverne le transport électronique dans des différentes conditions dans ce matériau.

Contents

Acknowledgments

Abstract

| | | |
|----------|--|----------|
| 1 | 2D materials and doping | 1 |
| 1.1 | Introduction | 1 |
| 1.2 | Electrostatic doping | 2 |
| 1.3 | Graphene | 4 |
| 1.3.1 | Electronic structure | 4 |
| 1.3.2 | Synthesis | 6 |
| 1.3.3 | Graphene characterization | 8 |
| 1.3.4 | Electronic transport properties | 10 |
| | Scattering mechanisms and mobility | 11 |
| | Mobility | 12 |
| | Magnetotransport | 13 |
| 1.3.5 | Doping of graphene | 13 |
| | Electrostatic doping | 14 |
| | Chemical and substitutional doping | 14 |
| 1.3.6 | Graphene as transparent conducting electrode | 15 |
| 1.4 | Zinc oxide | 16 |
| 1.4.1 | Crystal and electronic structure | 16 |
| 1.4.2 | Crystal growth | 17 |
| | RF magnetron sputtering | 17 |
| | Other deposition techniques | 18 |
| 1.4.3 | Characterization of ZnO | 19 |
| | X-ray diffraction spectrum of ZnO | 19 |
| | AFM | 20 |
| 1.4.4 | Doping of ZnO | 21 |
| | <i>n</i> -doping | 21 |

| | | |
|----------|--|-----------|
| | <i>p</i> -doping | 22 |
| 1.4.5 | Magneto-transport properties | 22 |
| 1.4.6 | ZnO as TCE | 23 |
| 2 | Experimental | 25 |
| 2.1 | Samples fabrication | 25 |
| 2.1.1 | Glass substrates involved | 25 |
| 2.1.2 | Graphene | 26 |
| 2.1.3 | Zinc oxide | 30 |
| 2.2 | Characterization methods | 31 |
| 2.2.1 | Optical microscope | 31 |
| 2.2.2 | Atomic Force Microscopy | 31 |
| 2.2.3 | Raman Spectroscopy | 33 |
| | The principles of Raman scattering | 33 |
| | Raman microscopy in 2D materials | 35 |
| 2.2.4 | X-ray diffraction | 37 |
| 2.3 | Device fabrication | 39 |
| 2.3.1 | Van der Pauw method | 40 |
| 2.3.2 | Contact deposition | 41 |
| 2.3.3 | Sample shaping | 42 |
| 2.4 | Electronic transport measurements setup | 44 |
| 3 | Space Charge Doping | 45 |
| 3.1 | The principles of space charge doping | 46 |
| 3.1.1 | Glass atomic structure | 46 |
| 3.1.2 | Ionic drift | 47 |
| 3.2 | Space charge doping applied to graphene | 49 |
| 3.2.1 | Fabrication of the graphene samples | 50 |
| | CVD graphene | 50 |
| | Anodic Bonded graphene | 51 |
| | Contact deposition and shaping | 55 |
| 3.2.2 | Results | 56 |
| | Ambipolar doping | 56 |
| | Fine doping and doping limit | 59 |
| | Reversibility | 63 |
| | Substrate surface quality | 63 |
| | Transmittance | 66 |
| | Quality of the doped samples | 68 |
| 3.3 | Comparison with other doping methods | 69 |
| 3.4 | Control measurement on quartz | 72 |
| 3.5 | Conclusions on space charge doping | 72 |

| | | |
|----------|--|------------|
| 4 | Ultra-high doping of ZnO_{1-x} thin films | 75 |
| 4.1 | ZnO _{1-x} device fabrication | 76 |
| 4.1.1 | Zinc oxide deposition on glass | 77 |
| 4.1.2 | X-ray diffraction, AFM and transmittance | 78 |
| 4.1.3 | Sample shaping and contact deposition | 83 |
| 4.2 | Space Charge Doping applied to the ZnO thin film | 84 |
| 4.2.1 | Fine control of doping in the thin film | 84 |
| 4.2.2 | Carrier scattering mechanism | 88 |
| | Lattice phonon scattering | 89 |
| | Grain boundary scattering | 89 |
| | Ionized impurity scattering | 90 |
| 4.3 | Variable Range Hopping and mobility edge | 91 |
| 4.3.1 | Variable range hopping in ZnO thin films | 93 |
| 4.3.2 | Mobility edge | 94 |
| 4.3.3 | 2D nature of the doped film | 96 |
| 4.4 | Conclusions on space charge doping of ZnO | 97 |
| 5 | Magneto-transport and spin orbit coupling | 99 |
| 5.1 | Weak localization | 100 |
| 5.1.1 | Backscattering | 101 |
| 5.1.2 | Temperature dependence of the conductivity | 101 |
| 5.2 | Magneto-conductivity | 103 |
| 5.2.1 | Theoretical considerations | 103 |
| | Effect of the weak localization | 103 |
| | Influence of spin-orbit coupling on the magneto-con- | |
| | ductivity | 104 |
| 5.2.2 | Magneto-conductivity of ZnO | 106 |
| | WL to WAL transition as a function of temperature . | 106 |
| | WL to WAL transition as a function of carrier con- | |
| | centration | 110 |
| | Considerations on the characteristic transport lengths | 113 |
| 5.3 | Origin of the spin-orbit coupling | 114 |
| 5.3.1 | D'Yakonov-Perel' mechanism | 114 |
| 5.3.2 | Rashba effect | 115 |
| 5.3.3 | Elliott-Yafet mechanism | 116 |
| 5.4 | Considerations on the metal-insulator transition | 118 |
| 5.5 | Conclusions of the magneto-transport in ZnO | 119 |
| 6 | Conclusions and perspectives | 121 |
| | List of abbreviations and symbols | 125 |

Chapter 1

2D materials and doping

1.1 Introduction

The modulation of the electronic properties of a material with the eventual generation of electronic phase transitions is the driving force behind a variety of discoveries and inventions in condensed matter physics and chemistry and materials science. It is for example a key requirement for the use of a material in electronics. In semiconductors this is usually achieved by chemical means, by introducing a precise amount of impurities in a pure crystal and changing the charge carrier density. This process, known as chemical doping, is widely used to change material properties, for example to introduce a metallic or superconducting transition in a host material. If the introduced charge carriers are electrons, the doping is of type n , while we would have p -doping if the doped charge carriers are holes.

Modulating the charge carrier density in a very thin or surface layer can be also achieved electrostatically through the application of an electric field. The usual way to perform this kind of doping is through a metal-insulator-semiconductor sandwich known as a field effect transistor. If a potential difference is applied between the metal and the semiconductor through the intermediary insulator, the corresponding band bending produced at the interface between the insulator and the semiconductor will create an accumulation of charge carriers (the sign of the charges depends on the polarity of the potential difference). This metal-insulator-semiconductor field effect transistor is a ubiquitous component, with dynamic or static attributes, of all microelectronic devices.

In recent years there has been a growing interest in the study of two-dimensional materials. Very generally a two-dimensional (2D) system in condensed matter physics can be considered as a system where one dimension is much smaller than some typical coherence length. Thus, in very pure semiconductor heterostructures (for example the two-dimensional electron gas (2DEG) found in a Si inversion layers using a metal-oxide-semiconductor

(MOS) structure [1]), a channel several tens of nanometers thick containing mobile carriers with a mean free path which is ten times larger, is still 2D. More recently, 2D materials have come to mean few atomic layer materials, usually exfoliated from bulk layered precursors [2]. This technique is based on the fact that some materials are formed in layers, with strong adhesion of the atoms within the layer and weak attraction (van der Waals forces) between adjacent layers so that it is possible to separate and isolate few layers or even a single atomic layer of material. Several other techniques are now used for fabricating 2D materials like chemical vapour deposition (CVD) [3] or anodic bonding [4]. They hold promise from an industrial point of view for example a 2D material could provide ways for increasing device density in microelectronics. From the point of view of fundamental research, a 2D material could present some unique features which are not observed in three-dimensional systems as a direct consequence of the quantization of the energy levels or for topological reasons. For our purposes 2D materials are ideal for the application of electrostatic doping since, as we point out above, this method is applicable to ultra-thin layers. However limited options exist to do this, especially to ultra-high carrier concentrations.

In this thesis, a new technique called *Space Charge Doping* for electrostatically doping materials deposited on glass has been developed. The technique exploits an intrinsic feature of glass in order to create a space charge at the interface between the glass and the material and was applied to two different materials: graphene and ultra-thin films of zinc oxide. The first tests on the space charge doping were done on graphene as it is a 2D material that can be produced relatively easily and can be doped *n* or *p*. It has also potential applications as a transparent conducting electrode (TCE). We then applied the space charge doping to ZnO in order to validate the technique for thin-films (thus not an intrinsically two-dimensional material) and to study the properties of this material when it is highly doped. ZnO can also be potentially used as a TCE material and also has been investigated for other applications which involve doping, for example spintronics.

In this chapter an overview of the electronic properties, synthesis methods, applications and doping techniques of graphene and zinc oxide will be given in order to prepare the ground for the results which will be presented in the rest of this thesis.

1.2 Electrostatic doping

A central result of this thesis is the development of a new and original electrostatic doping technique. Electrostatic doping is crucial for microelectronics since it is the basic working principle of the metal-oxide-semiconductor field effect transistor (MOSFET). In fundamental research it is progressively being used as a powerful and reversible tool for inducing electronic phase

transitions in a number of materials [5]. Here we give a brief description of the basic concepts of the electrostatic doping.

A MOSFET is composed of a conducting channel, drain and source contacts placed at the channel edges and a gate contact placed on top of the channel and separated from it by a dielectric layer. The gate electrode is used to modulate the conductivity of the channel (Figure 1.1). The channel and the gate electrode behave like the two conducting faces of a capacitor. Thus the application of a gate voltage V_G will cause an accumulation of charges at the semiconductor-oxide interface which is the channel. The electric field generated by the gate electrode penetrates into the channel and causes a shift in the energy spectrum at the interface with the oxide. The relative shift of the energy bands of the semiconductor with respect to the Fermi energy of the whole device causes a change in the carrier concentration at the semiconductor/oxide interface. We could thus create an accumulation, depletion or inversion layer if, respectively, the density of charge carriers is augmented, reduced or reversed in sign [5]. This is schematically shown in Figure 1.1. In this particular case, depending on the polarity and magni-

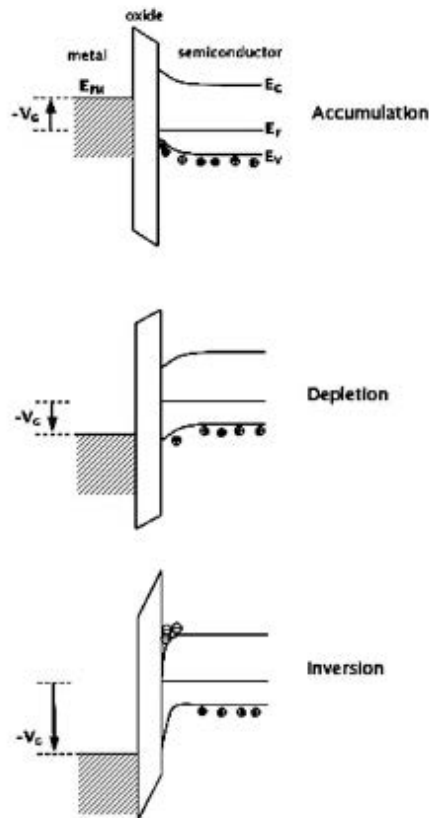


Figure 1.1: Schematization of the field effect in a metal-oxide-semiconductor structure in the particular case of a p -doped semiconductor. Re-printed from 1.1

tude of V_G , in a p -doped semiconductor one can induce an enhancement or reduction of the hole concentration at the interface or, if the polarity of V_G is reversed, an electron concentration. Moreover, like in a capacitor, the higher the capacitance associated with the MOS structure, the higher the carrier accumulation at the interface. This can be achieved with oxides or dielectrics with a high dielectric constant or with thinner oxides. Typical surface carrier density attainable with this method is of the order of $10^{12} - 10^{13} \text{ cm}^{-2}$.

This basic doping principle has been used not only to fabricate devices for electronics applications but also, for example, to induce insulating-superconducting transitions [6] or in a more exotic implementation through the use of liquid electrolytes [7] used to significantly increase the associated capacitance of the gate electrode.

This principle of modification of electronic properties at the interface has been exploited in this thesis to develop our original doping method capable of reaching considerably higher doping than the MOSFET structure in a reversible and reliable way.

1.3 Graphene

1.3.1 Electronic structure

Graphene is a single layer crystal of carbon atoms disposed in an hexagonal geometry. This hexagonal structure can also be seen as two compenetrating triangular lattices A and B [8], as shown in Figure 1.2. The 2D lattice vectors of the unit cell are $\mathbf{a}_1 = (a/2)(3, \sqrt{3})$ and $\mathbf{a}_2 = (a/2)(3, -\sqrt{3})$ with $a \approx 0.142 \text{ nm}$ the carbon-carbon distance. The atoms are bond together with strong σ bonds with their three neighbours. The fourth bond is a π bond lying perpendicular to the graphene plane. The π bond can be seen as two lobes which are centred in the nucleus; each atom has it and they hybridize together to form what is called the π and the π^* bands. Thanks to this particular atomic arrangement graphene has some unique properties in terms of electronic transport and mechanical properties.

The energy dispersion of a single layer graphene was calculated in 1947 by Wallace [9] with the tight-binding approximation for a single layer of graphite and the result of the calculation is shown in Figure 1.3. At the edge of the first Brillouin zone there are what are called the Dirac points (\mathbf{K} and \mathbf{K}'), with coordinates

$$\mathbf{K} = \left(2\pi / (3a), 2\pi / (3\sqrt{3}a) \right) \quad (1.1)$$

and

$$\mathbf{K}' = \left(2\pi / (3a), -2\pi / (3\sqrt{3}a) \right). \quad (1.2)$$

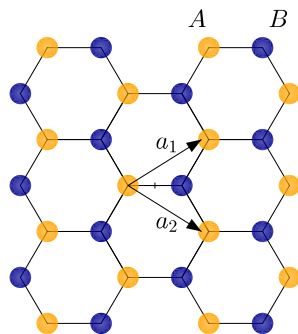


Figure 1.2: Graphene hexagonal atomic structure. The two triangular sub-lattices are highlighted in blue and yellow.

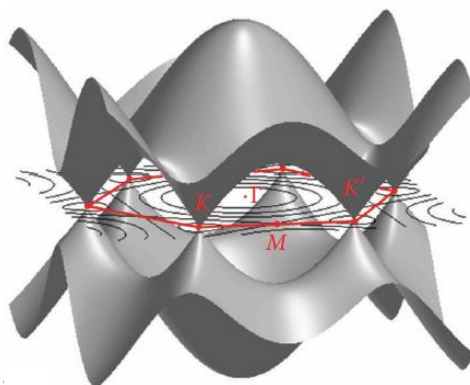


Figure 1.3: Graphene energy dispersion relation with highlighted the K and K' points. Readapted from [10].

There exist two sets of three non-equivalent Dirac points, each set coming from one of the two triangular sub-lattices of graphene, giving a valley degeneracy $g_v = 2$. In \mathbf{K} and \mathbf{K}' the conduction and valence band meet, making graphene a zero-gap semiconductor, which is why it is often referred to as a semi-metal. In neutral conditions, the Fermi energy lies and the meeting point of the two bands. The most important remark is that charges in the region within 1 eV from the Dirac energy have a linear dispersion relation

(Figure 1.4), as described by the Dirac equation for massless fermions:

$$E_{\pm}(k) \approx \pm \hbar v_F |k - K| \quad (1.3)$$

with the Fermi velocity $v_F \approx 10^6$ m/s or $1/300^{\text{th}}$ the speed of light in vacuum and \hbar is the reduced Planck constant.

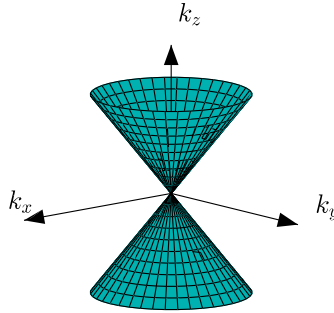


Figure 1.4: Linear dispersion relation of graphene at the Dirac point.

1.3.2 Synthesis

There exist nowadays several techniques for the fabrication of graphene. The aim is to produce graphene with the least possible concentration of defects and the largest possible area. The synthesis techniques discussed in the following in general either do one or the other.

Mechanical exfoliation The mechanical exfoliation technique led to the isolation of the first graphene sample [2]. A piece of highly oriented pyrolytic graphite (HOPG) or natural graphite is peeled off repeatedly with adhesive tape until really thin flakes of graphite are isolated. They are then deposited on the Si/SiO₂ surface. This technique generates samples of excellent quality, with typical lateral size of a few tens of microns and it is thus well suited for fundamental research but not for a large scale production.

Chemical Vapour Deposition (CVD) Chemical vapour deposition has shown to be a promising technique for the production of large area graphene samples. The deposition of graphene is due to the decomposition of a carbon carrier gas at high temperature (~ 1000 °C) onto the surface of a metal substrate (typically nickel or copper [11]). The atmosphere in which such a

process is usually carried out is CH_4 (the carbon carrier) and hydrogen. The work done in Reference [12] revealed that the number of layers of graphene growth on nickel is dependent by the cooling rate giving a monolayer only at a certain cooling rate. On the other hand, the growth of graphene on copper is self limiting and the number of layers is independent on the cooling rate [11]. Copper substrates are generally preferred for the low C solubility in Cu. The final product is a metal substrate (Cu or Ni) entirely covered with graphene on both sides. The quality of the obtained films is good, but still not comparable to the exfoliated graphene flakes.

Despite the good quality and large area, as grown CVD graphene is not ready to be used for applications in electronics because of the metal substrate on which it is deposited. Thus, a transfer step onto an insulating substrate is necessary. The most widely used technique is the polymer assisted transfer: the graphene on the metal substrate (copper for example) is covered with a polymer film (usually polymethyl-methacrylate, PMMA) which is used as mechanical support [11]. The graphene layer on the other side is etched away and the Cu/graphene/PMMA stack is let float on the surface of an etchant solution for copper. After copper is removed, the floating polymer/graphene film is then rinsed several times in de-ionized water to remove the residues of the etching solution and finally it is “fished” with the final substrate. It is then let it dry in air and after a baking in air used to soften the polymer and enhance the adhesion on the substrate, the substrate/graphene/polymer is immersed in acetone to dissolve the polymer. The copper etchants usually involved are iron nitrate [13], iron chloride or ammonium persulfate [3]. An interesting technique for industrial application of CVD graphene was proposed by Bae *et al.* [14] where a roll-to-roll technique is used to transfer really large area of graphene on a PET substrate.

Thermal decomposition of SiC Another graphene synthesis method which is for production of large area graphene is the thermal decomposition of silicon carbide. Basically, this technique involves a substrate of SiC heated at really high temperatures ($1000 \leq T \leq 1500$ °C) in ultra-high vacuum (UHV). The preferred forms of SiC which are involved are the hexagonal 4H- and 6H-SiC and the growth of graphene can be done on the silicon face or the carbon face of the substrate. The difference between the growth on the two faces are in terms of the growth rate and the crystalline orientation of the graphene film (better on the Si-face than the C-face) [15].

Anodic Bonding *Anodic Bonding* is a welding technique developed in 1969 by Wallis [16] used to seal silicon to glass without the addition of intermediate layers (such as glue). Glasses are formed by an amorphous network of SiO_2 . The introduction of Na_2O and CaO breaks some Si-O-Si bridges and the non-bridging oxygen atoms serves as anions for the Na and

Ca cations. It is found that sodium ions mobility is much higher than the calcium ions mobility [17] at high temperature and an applied electric field causes sodium ions drift. The anodic bonding technique exploits the sodium ions drift to deplete the glass/material interface of Na^+ ions which leave and uncompensated oxygen ions space charge which forms a strong electrostatic bond with the silicon sealing them together. The same principle has been applied to 2D materials [4, 18, 19, 20], and in particular to graphene. A thin piece of graphite is deposited on a glass substrate. It is then heated at temperatures up to 290 °C and a voltage $V_G \leq 2$ kV is applied and leaved for 10 to 30 minutes. In this time the space charge at the interface is created and, when the sample is cooled down, the top layers are removed with the help of adhesive tape leaving from one to few layer of material on the glass surface. With graphene, high quality samples are obtained with typical lateral size ranging from 50 to 200 μm . The anodic bonding technique will be described in details in Chapter 2.

1.3.3 Graphene characterization

Many techniques are used for characterizing graphene. For device fabrication, the most important things to know about a graphene sample are its effective number of layers and its quality. The most widely used characterization methods, which are the ones used in this thesis, are optical characterization, Raman spectroscopy and atomic force microscopy (AFM).

Optical microscopy The optical microscope is the first characterization tool which is usually involved in the identification of a graphene sample. Graphene is almost transparent, with $\sim 97\%$ of transmittance in the visible range [13]. However, when graphene is deposited on SiO_2 it is possible to vary the contrast by changing the light source wavelength and its intensity. The contrast increases also with the number of layers, making a monolayer sample to be recognizable with respect to a bi-layer or a multi-layer graphene. The same considerations are valid also for other substrates such as glass, which is the substrate used in this thesis for our studies on graphene. The optical contrast of graphene deposited on glass is lower with respect to a sample deposited on SiO_2 , but it is still sufficient to uniquely recognize a monolayer graphene sample.

Raman spectroscopy Raman spectroscopy has been proven to be an essential tool in the characterization of graphene. From the Raman spectra of graphene it is possible to count the number of layers of graphene and check its quality [21, 22]. A characteristic graphene Raman spectrum is showed in Figure 1.5, where the three main peaks of graphene are showed: the G band at $\sim 1580 \text{ cm}^{-1}$, the G' band (often called 2D band) at $\sim 2680 \text{ cm}^{-1}$ and the D band at $\sim 1350 \text{ cm}^{-1}$. The Raman spectrum of

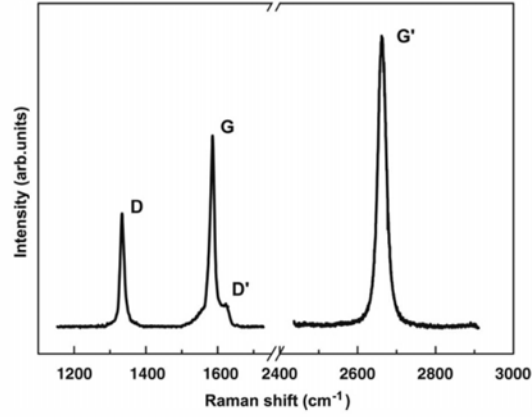


Figure 1.5: Raman spectrum of a graphene sample with defects. Re-printed from [21].

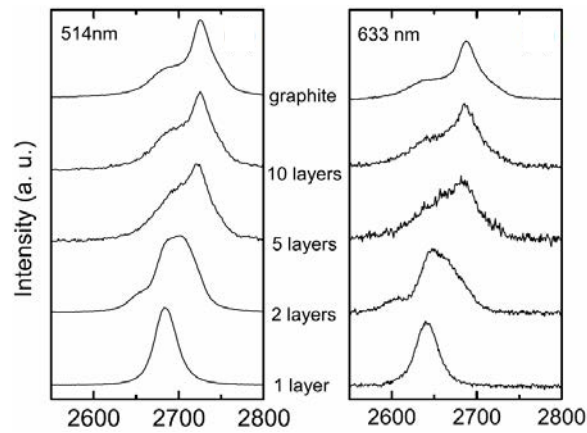


Figure 1.6: 2D peak evolution with the number of layers for different laser excitations. Re-adapted from [22].

graphene contains precious information: the G band comes from the in-plane vibration of sp^2 carbon atoms and is the most prominent resonant phenomenon in graphitic materials. The 2D band comes from a mechanism of double resonance between the excited electron and the phonons near \mathbf{K} , as explained in Reference [22]. This peak is the fingerprint of graphene as in the monolayer it is a single, sharp and symmetric peak with a higher intensity

with respect to the G peak. Moreover, the shape on the 2D peak evolves with the number of layers (becoming asymmetrical), as shown in Figure 1.6. Finally, the D peak arises from the breaking of the double resonance and, thus, from the defects in graphene. From Raman spectroscopy it is also possible to get some information about the carrier concentration. In fact, as reported in Reference [23], the position of the 2D and G peak, as well as the ratio of their intensities, changes significantly with the concentration of charge carriers in the graphene sheet. Raman spectroscopy is thus a powerful tool for the characterization of a graphene sample because it gives unambiguous information in terms of the number of layers, quality and doping.

Atomic force microscopy (AFM) AFM topography is another essential tool for the study of graphene. First of all, with AFM it is possible to count (or confirm) the number of layers of the studied sample. AFM offers an extremely accurate measure of the thickness of the sample and of the quality of its surface, indicating if the surface of the graphene sample is contaminated or not (which is useful information for the contact deposition).

Other techniques Some other techniques (not used in this thesis) are widely used for the characterization of graphene. We briefly cite transmission electron microscopy (TEM) and angle-resolved photoemission spectroscopy (ARPES). Electron microscopy has been used to see grain boundaries in CVD graphene transferred on a TEM grid [24]. It has been shown that the different grains of graphene are connected together with distortion of the hexagonal lattice of graphene *i.e.* with pentagon-heptagon pairs or with distorted hexagons. These considerations are important in the understanding of the scattering mechanisms which dominates the electronic transport in graphene. On the other hand, ARPES measurements provide a direct measure of the electronic band structure through the analysis of the electrons emitted from the graphene sheet as a function of the direction of emission and their energy. An example of the measured electronic band structure of a multi-layer graphene can be found in Reference [25].

1.3.4 Electronic transport properties

The motion of charge carriers in graphene has some unique properties as a consequence of its electronics band structure, such as the ambipolar field effect and minimum conductivity. This phenomenon can be seen if graphene is put in a field effect transistor configuration. What is usually done is to deposit a monolayer graphene sample on an oxidized Si substrate (which serves also as gate electrode) and it is then contacted for electrical measurements, usually with gold electrodes. The variation of the gate voltage induces a change in the carrier concentration in graphene (exactly like in a

MOSFET) by moving the Fermi level from the equilibrium condition in the conduction or the valence band. Thus the gate voltage performs an electron (n) or hole (p) doping, depending on its polarity [2]. Figure 1.7 shows the ambipolar field effect of graphene deposited on SiO_2 .

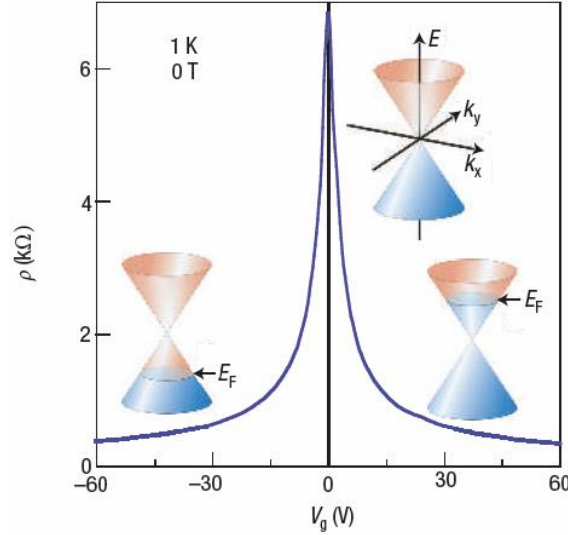


Figure 1.7: Graphene ambipolar conductivity as a function of the gate voltage. Re-printed from [26].

The minimum conductivity is another interesting phenomenon: in fact, unlike conventional semiconductors, graphene conductivity σ does not vanish at zero field and it shows a minimum value. The value of σ_{min} is of the order e^2/h but it is unclear whether there is a universal prefactor to it [27].

Scattering mechanisms and mobility

The electronic transport is determined by many factors such as: defects in the crystal structure, impurities, interaction with the substrate and phonons. All these factors produce inhomogeneities in the charge carrier distribution in the device for low values of the carrier density or reduce the mean free path l at high carrier density. From a theoretical point of view, two transport regimes can be distinguished, depending on the amplitude of l and the graphene device size L . When $l > L$ the transport is said to be in the ballistic regime since the charge carriers can travel all along the device at the Fermi velocity v_F without scattering. Transport is then described by the Landauer formalism as

$$\sigma_{ball} = \frac{L}{W} \frac{4e^2}{h} \sum_{n=1}^{\infty} T_n \quad (1.4)$$

where the T_n are transmission probabilities of all the possible transport modes [28]. At the Dirac point, the theory predicts that the minimum conductivity has the value

$$\sigma_{min} = \frac{4e^2}{\pi h} = 4.92 \times 10^{-5} \Omega^{-1} \quad (1.5)$$

but experimental observations showed that this value can vary from device to device [27]. For the case $l < L$, the charge carriers experience the elastic and inelastic scattering mechanisms and the system undergoes in the diffusive regime. The semiclassical Boltzmann transport theory comes into play [8] and the transport at low temperature can be expressed as

$$\sigma_{sc} = \frac{e^2 v_F \tau}{\hbar} \sqrt{\frac{n}{\pi}} \quad (1.6)$$

where τ depends on the scattering mechanism. The main scattering processes active in graphene are reviewed in Reference [10] and briefly reported in the following:

- **Phonon scattering:** phonons are an intrinsic source of scattering at finite temperature even when all other scattering processes are suppressed. Longitudinal acoustic (LA) phonons are known to have the highest cross section with respect to the other vibrational modes and they also produce an elastic source of scattering. The contribution of the phonons to the resistivity of graphene can be recognized by the temperature dependence of the resistivity, being linear for high temperature and like $\sim T^4$ at low temperature.
- **Coulomb scattering:** another important scattering phenomenon is represented by charged impurities (ions) trapped between the graphene sheet and the substrate. Those impurities act as a long range Coulomb scatterers which, for low charge carriers concentration ($n \ll n_i$, with n_i the impurity concentration) bring to the formation of puddles of electrons and holes across the sample [29]. At high carrier density and for randomly distributed impurities the conductivity decreases as n_i increases ($\sigma \propto 1/n_i$).
- **Short-range scattering:** short range scatterers are responsible for the formation of mid-gap states. Those scattering centres are represented by cracks, edges and vacancies but they all can be modelled as vacancies of effective radius R [28].

Mobility

Mobility in graphene can reach the value of $\mu = 350000 \text{ cm}^2\text{V}^{-1}\text{s}^{-1}$ [30], which is quite surprising compared to other semiconductors. Having an

electronic device which such a mobility would lead to a much faster electronics compared to the silicon based devices. But in the practice reaching values of mobilities so high is quite hard. Bolotin *et al.* measured $\mu \sim 170000 \text{ cm}^2\text{V}^{-1}\text{s}^{-1}$ in a ballistic transport regime [31]. To do that, they fabricated suspended graphene devices by etching the substrate underlying the graphene sample and performing a current annealing to clean the device. Of course this is not of a practical use because for electronics applications since graphene needs to be in contact with a substrate and eventually an insulator to ensure the field effect. For this purpose, another type of substrate is often used: hexagonal boron nitride (h-BN). Boron nitride is a wide band-gap semiconductor (5.97 eV) with the same crystal structure of graphene, with B and N atoms occupying the A and B sites of the graphene lattice. Moreover, there is a good lattice matching between graphene and h-BN, which makes it a really good substrate for graphene. h-BN has also been used for packaging graphene for high-frequency applications [32] reaching a cut-off frequency of several GHz or for obtaining high mobility graphene devices, reaching the stunning value of $350000 \text{ cm}^2\text{V}^{-1}\text{s}^{-1}$ [30].

Magnetotransport

Magnetotransport in graphene is a really important topic for many reasons: it is an essential tool for measuring the carrier density in graphene through the Hall effect and it shows really important phenomenons related to the 2D nature of graphene, the Quantum Hall Effect.

The Hall effect is a phenomenon observed when charge carriers travelling inside a material are subjected to an external magnetic field. If a current is passed inside a device and a magnetic field is applied perpendicular to the current flow, the charges will experience the Lorentz force in the direction perpendicular to the current flow and to the magnetic field. As a consequence, a certain number of charge carriers will accumulate at the edge of the device and a transversal voltage will appear. For small magnetic fields, it is possible to define a *Hall resistance* defined as $R_{xy} = IBR_H$, with I the current flowing in the device, B the applied electric field and $R_H = 1/ne$ the Hall coefficient (e is the electrical charge and n the charge density). So, by plotting the value of R_{xy} as a function of B it is possible to evaluate the charge density n in the material. In high mobility graphene and at high magnetic fields allowed energy levels for electrons split, forming the so called *Landau levels* [33] and resistivity plateaux.

1.3.5 Doping of graphene

We show in Chapter 3 that we used the technique of the space charge doping to dope graphene with much better doping performances than conventional methods. A review of the commonly used doping technique in graphene is

thus necessary.

Doping in graphene can be achieved in several ways. The first thing to mention is that, since graphene is only a one atom thick it is very sensible to air pollution and it is very easy to obtain some unwanted doping due to the air. Moreover, the transfer techniques used to deposit graphene onto different substrates introduce a certain density of charged impurities between the graphene layer and the substrate [34] which, again, induces an unwanted doping. These aspects have to be taken into account in our experimental study of graphene.

The study of the properties of graphene requires that the carrier concentration must be precisely controlled [2, 23, 35]. In the following, an overview of the doping technique usually involved to dope graphene is given.

Electrostatic doping

The first technique to be used for the modulation of the carrier concentration in graphene is through the field effect [2]. This technique is extensively used since it allows a fine control of the charge density in a reversible way, both in the electron and the hole side. The most straightforward way to build a transistor with graphene is by depositing it on an Si/SiO₂ substrate and deposit metal contacts on it. The Si/SiO₂ substrate serves as gate electrode and, depending on the polarity of the voltage applied to the silicon, an electron or hole concentration can be induced in graphene [36]. This method has the disadvantage of not inducing very high carrier concentration because of the low capacitance associated with the Si/SiO₂/Graphene structure (the thickness of the SiO₂ layer is ≈ 200 nm). Alternatively, the capacitance associated to the gate electrode can be increased by diminishing the thickness of the dielectric. In this case, top-gated or bottom-gated graphene transistor have been realised with the used of dielectrics like boron nitride [37], oxides [38, 39, 40], ionic liquids [41] or polymers [42].

Electrostatic doping is a reliable way of doping graphene. However, it presents some disadvantages like the maximum reachable carrier density and the fact that graphene transport properties can be strongly affected by the presence of the substrate and eventually the top dielectric.

Chemical and substitutional doping

Another way to dope graphene is through the addition of foreign atoms to the atomic structure of graphene or placed on its surface which serve as donors or acceptors. One interesting method has been proposed by Bae *et al.* [14]. Here, a roll-to-roll technique is used to transfer a large area (~ 80 cm in diagonal size) graphene sheet onto a PET substrate while at the same time it is doped with nitric acid (HNO₃). The result is a *p*-doped graphene sheet, but the doping has been found to be unstable in time.

Another way to chemically dope graphene can be achieved, for example, with AuCl_3 deposited on the graphene surface [43, 44], but the authors found that this technique is not 100% reproducible. Aromatic molecules deposited on the surface of graphene have also been used [44, 45], but also in this case problems regarding the stability of the doping have been met.

Substitutional doping is another interesting way for doping graphene. To perform *n*-doping, nitrogen can be used during the synthesis of CVD graphene [46, 47] or during the decomposition of SiC into graphene [48], while for *p*-doping it has been proposed the use of boron [49]. However, this kind of doping can induce defects in the graphene structure, can be unstable and it is not reversible.

1.3.6 Graphene as transparent conducting electrode

Most of the techniques described above have been used to try to transform the graphene sheet in a transparent conducting electrode (TCE). Graphene is very promising for this kind of application because of its transparency and its impressive transport properties. However, undoped (or slightly doped) graphene has a sheet resistance too high for TCE applications and doping is thus necessary to increase its carrier density and lower R_S . Electrostatic doping performed with conventional techniques, like shown in References [37, 38, 39, 40, 41, 42], is not suitable for TCE applications because it involves the use of other materials deposited on the graphene sheet which lower its transparency and may not reach very high doping. Moreover, the depositing materials on graphene significantly alter its electronic transport properties.

Chemical doping has been successfully used to dope graphene for TCE applications. For example, in Reference [14] CVD graphene doped with nitric acid is used as TCE for display and touchscreen applications, while in References [43, 44] graphene doped with AuCl_3 is used for the fabrication of solar cells. As mentioned before, chemical doping has some important and not negligible issues in terms of time stability of the carrier concentration.

Another attempt to produce TCE with graphene is by using multi-layer graphene. If more layers of graphene are stuck together the resulting conductivity can be significantly enhanced with respect to the monolayer, still maintaining the transmittance above to 90% in the visible range [43]. In Reference [50] multi-layer graphene for the fabrication of LEDs has been demonstrated. However, this technique very is inconvenient to use because it involves many transfer processes in order to obtain the desired multi-layer graphene structure with the risk of damaging the whole device at every transfer step.

As we will show later in this thesis, space charge doping can overcome many of these problems and can have thus potential applications in the field of TCEs.

1.4 Zinc oxide

Zinc oxide (ZnO) is a wide band-gap semiconductor with a direct gap of ~ 3.3 eV at 300 K [51]. It is a widely studied material since many decades for its electronic, optical and piezoelectric properties. In optoelectronics it has a number of features which overlap with GaN but ZnO presents some advantages also in terms of availability of high quality bulk crystals.

The space charge doping technique should be readily applicable to a well-defined single crystalline layer deposited onto a substrate, which is the case of graphene. But if our doping technique is versatile, we should be able to apply it to a variety of polycrystalline thin films deposited on glass by standard deposition techniques. This was the reason to choose a large gap semiconductor like ZnO which is quite different from graphene as far as material and electronic properties are concerned. Moreover we had the possibility to produce high quality samples thanks to the magnetron sputtering facility at the Institut des NanoSciences de Paris. Finally, doped ZnO, like graphene is a widely studied material in many fields and in particular in the field of Transparent Conducting Electrodes (TCEs) and spintronics, making it easy to compare results obtained by our method with other results in literature.

1.4.1 Crystal and electronic structure

ZnO can crystallize in three different forms: wurtzite, zinc blende, and rocksalt [52] as shown schematically in Figure 1.8. The thermodynamically stable crystal structure in ambient conditions is the wurtzite phase and its corresponding band structure is presented in Figure 1.9.

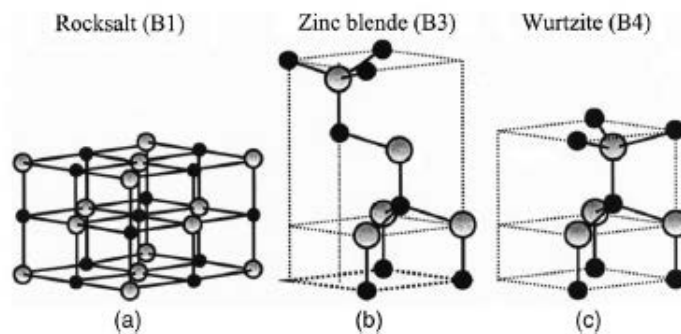


Figure 1.8: The three different crystal structure of ZnO. Re-printed from [52].

ZnO has been widely studied in the past because it possesses some very interesting properties and it can be a promising and cheap substitute for GaN. Its large and *direct* band-gap (as shown in Figure 1.9) makes ZnO

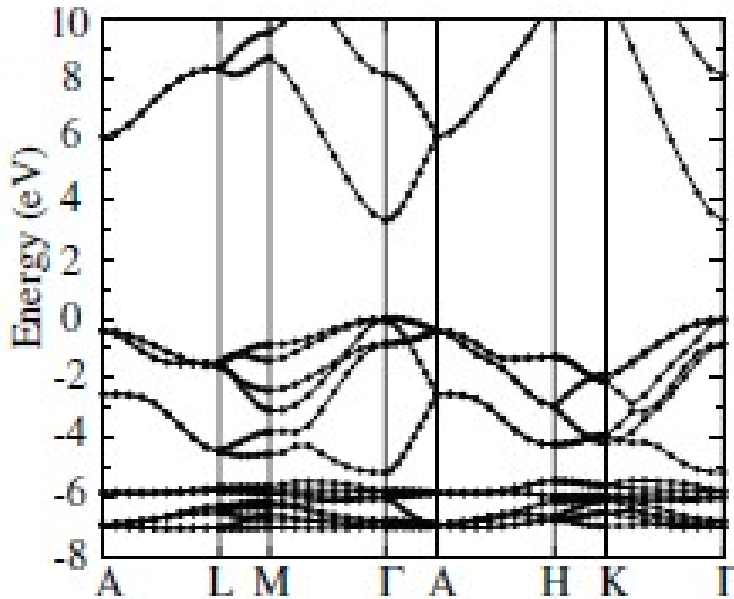


Figure 1.9: Electronic band structure of ZnO. Re-printed from [51].

suitable for optoelectronics applications in the blue/UV region like light-emitting diodes, lasers and photodetectors. However, nowadays its use is limited because of the inability to produce high quality *p*-type crystals. In fact, while it is relatively easy to grow high quality *n*-type ZnO, the hole-doped crystal has not yet demonstrated to be reproducible, requiring the use of heterostructure with other materials like Cu₂O in order to realize a *p-n* junction [53]. However, ZnO is widely used for its piezoelectricity [54] or as transparent conductor when it is heavily *n*-doped with foreign atoms like aluminium [55].

1.4.2 Crystal growth

The most used technique for the growth of high quality ZnO films is RF magnetron sputtering. However, many techniques are used to produce high quality samples such as molecular beam epitaxy, pulsed laser deposition, chemical vapour deposition or sol-gel.

RF magnetron sputtering

Sputtering is one of the most used techniques for the production of high quality ZnO thanks to its low cost, low operating temperature and simplicity. The deposition is carried out in a chamber where a mixture of oxygen and argon is injected in a precise proportion. The RF power is then activated and the deposition of ZnO takes place thanks to the Ar plasma generated in

the chamber. Ar is used as sputtering enhancing gas while O is used for the reaction. The RF power activates the Ar plasma causing Ar^+ ions to hit the Zn or ZnO target. The extracted atoms travel towards the substrate facing the target through the O atmosphere and deposit as ZnO. In this thesis, a Zn target was used.

The choice of the substrate is important for the final orientation of the crystal and usually substrates such as diamond, glass, GaAs and Si are used [52], while the temperature can be varied from room temperature up to 400°C . The choice of the O/Ar ratio is very important. In fact, the oxygen content in the deposition chamber determines the stoichiometry of the deposited film [56] and depending on the value of the O/Ar ratio the ZnO film presents more or less oxygen vacancies which are important for its electronic transport properties.

Other deposition techniques

A review of the most used deposition methods for ZnO can be found in Reference [52]. Here we give a brief description of some of these.

Molecular beam epitaxy The advantage of using molecular beam epitaxy (MBE) is in the extremely precise control *in situ* of the growth parameters. Pure Zn is evaporated towards the substrate while oxygen flows on its surface, thus maximizing the oxidation of Zn. The deposition is controlled with reflection high-energy electron diffraction (RHEED), which gives a feedback for the adjustment of the deposition parameters. While it permits the deposition of high quality films, MBE is an expensive method and not as straightforward as RF magnetron sputtering.

Pulsed laser deposition The principle of the pulsed laser deposition method is to illuminate a target material with a high intensity pulsed laser in order to evaporate the material and create a jet of particles directed normal to the surface. The pulsed laser is chosen such that the stoichiometry of the evaporated material is preserved. A substrate is placed in front of the target so that the evaporated material can sublimate on its surface. In the case of ZnO, a zinc oxide target obtained from pressed ZnO powder is used and temperature between 200 and 800°C are involved.

Chemical vapour deposition Chemical vapour deposition (CVD) is an interesting deposition technique which allows the production of thin-films on a large scale. Generally speaking, the deposition takes place as the consequence of a chemical reaction. The precursors (in this case Zn and O) are transported in the reaction chamber by carrier gasses while a temperature gradient causes the chemical reaction which brings to the deposition of ZnO on the substrate.

Sol-gel Another widely used technique for the production of ZnO thin-films is by spin-coating a solution containing ZnO onto a substrate. It is then let dry with the help of heat and a thin-film of ZnO is then obtained [57, 58]. A heat treatment will then give crystallinity to the film.

1.4.3 Characterization of ZnO

Zinc oxide thin-film characterization is done mainly with two techniques: X-ray diffraction and atomic force microscopy. The first, gives informations about the size of the grains forming the film and their orientation, while the AFM is used to scan the surface in order to obtain a topography which also gives informations about the grain size. In this thesis the two techniques are used to characterize our ZnO samples.

X-ray diffraction spectrum of ZnO

The X-ray diffraction from ZnO powder is shown in Figure 1.10. We can see that there are several peaks corresponding to the different crystalline orientations. In the case of diffraction from thin-films, the XRD spectrum is

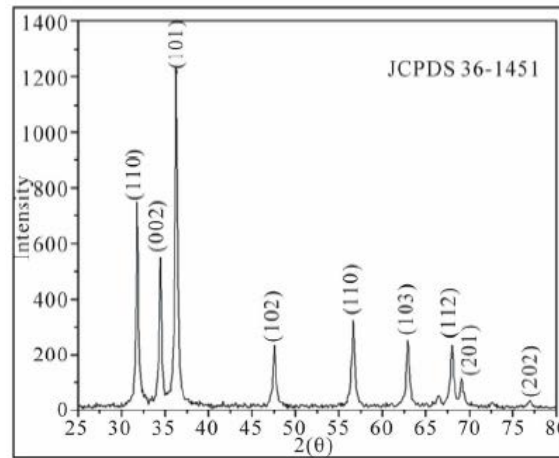


Figure 1.10: XRD spectrum obtained from ZnO powder. Re-printed from [59].

usually acquired in a grazing geometry in order to maximize the penetration of the X-ray into the material and the detector is swept in a range of angles. A typical XRD spectrum from a ZnO thin-film is shown in Figure 1.11. As it is commonly observed the film presents a preferred orientation of the grains along the $(00l)$ direction. As described in Chapter 2, the position and width of the peaks reveal the average size of the grains forming the film.

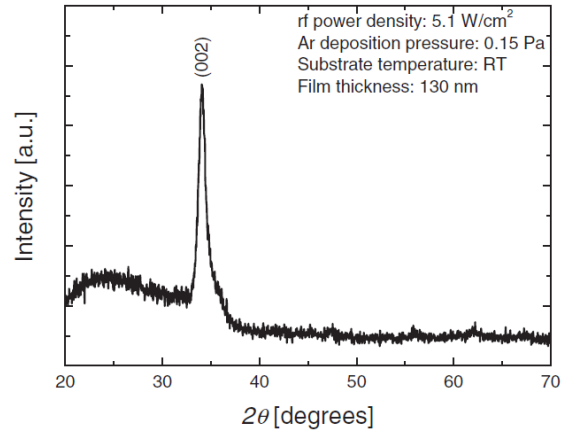


Figure 1.11: XRD spectrum obtained from a ZnO thin-film of ~ 130 nm in thickness deposited on glass. Re-printed from [60].

AFM

AFM scan of ZnO surface can give useful informations about the grain size which can be compared to the results obtained from the XRD data. An example of this kind of topography is shown in Figure 1.12.

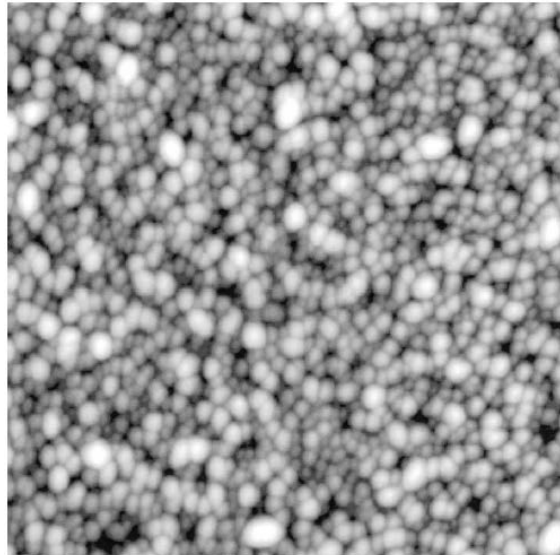


Figure 1.12: AFM scan of a ZnO thin-film deposited on a Si substrate. The film thickness is 108 nm. Re-printed from [61].

1.4.4 Doping of ZnO

For electronics applications doping of ZnO is an essential issue. It is relatively easy to dope ZnO with electrons and several techniques are used both for device applications or to create very highly doped surface layers. On the other hand the *p*-type doping is difficult to obtain in a reproducible way.

In the following, a description of the most used methods for the *n*-doping of ZnO and a brief mention to the attempts to *p*-doping will be given.

n-doping

Intrinsic doping ZnO is a natural *n*-type semiconductor. The *n*-type conductivity originates from the non-stoichiometry of the material due to the presence of oxygen vacancies which behave like donor type impurities [62, 63, 64]. Reference [65] shows that two types of defects exist associated with oxygen vacancies in ZnO, one identified with the oxygen vacancy itself and the other to clusters of oxygen vacancies. This work indicates that these defects act as donors in ZnO. However some authors argue that these being deep defects in the band-gap of ZnO they would instead act as compensating agent for any *p*-doping [66]. Experimental evidence however overwhelmingly shows that oxygen vacancies in ZnO are effectively responsible for the *n*-type conductivity. The ZnO samples studied in this thesis are intentionally fabricated with a degree of non-stoichiometry, being deficient in oxygen, in order to induce an initial carrier density. As it will be shown later in this manuscript, the evidence we found in our samples is in agreement with the fact that the oxygen vacancies are responsible for the *n*-doping in ZnO.

Chemical doping Aluminium is known to efficiently *n*-dope ZnO. The main use of aluminium-doped ZnO (Al:ZnO) is for transparent conducting electrodes and for this reason it is often deposited on glass by sputtering a ZnO target with the addition of Al₂O₃. The resistivity of the sputtered film can be significantly lowered with respect to the non-doped crystal, down to values around 10⁻⁴ Ω · cm [67] and applications of Al:ZnO have been demonstrated in devices like organic light-emitting diodes [55] or liquid crystal displays [68]. However, the main disadvantage of this technique is that the transparency of the thin-film is strongly altered (down to 80%) being at the limit of the use of ZnO as transparent conducting electrode, and of course the crystal structure of ZnO is also altered by the Al atoms.

Electrostatic doping ZnO surface layers have been investigated for different purposes going from transparent field effect transistors to the study of two-dimensional accumulation layers (quantum wells). The use of ZnO as the active layer of a transistor has been demonstrated by using different transparent layers of materials used as electrodes and gate dielectric

[60, 61, 63, 69]. For many applications, the MOSFET configuration has the disadvantage of not achieving a very high carrier concentration in the accumulation layer and to significantly reduce the transparency of the film with the use of many layers which serve as dielectric and contacts. More exotic techniques have been also used to achieve extremely high doping electrostatically, like the use of ionic liquids [70, 71]. These liquids are characterized by the presence of ions which are mobile in the presence of an electric field. If the ionic liquid is placed on top of ZnO, the ions can be accumulated at the surface of ZnO. The electric field associated with the ions is very high and electrons concentration up to 10^{14} cm^{-2} have been measured in the associated accumulation layer. However, this technique raises some questions about eventual intercalation of the ions inside the ZnO structure and also a practical problem at lower temperatures because of the freezing of the liquid which occurs by lowering the temperature of the system.

Other techniques As said before, ZnO accumulation layers are extremely interesting from a physical point of view because of ZnO single valley conduction band [72]. We mention some efficient techniques for producing strong accumulation layers on the surface of ZnO single crystals like exposure to atomic hydrogen [73], low-energy hydrogen ion implantation [74], exposure to thermalized He^+ ions [75]. Surface electron densities up to $5 \times 10^{14} \text{ cm}^{-2}$ have been achieved. However these techniques are not reversible, thus posing severe limitations on their use in the study of the properties of ZnO quantum wells.

***p*-doping**

It has been mentioned that *p*-type doping of ZnO is a difficult task. This can be attributed to several factors like compensation of the dopants by native defects or low solubility of the impurity in ZnO. It is known that in ZnO group-I elements like Li, Na and K, Cu, Ag, Zn vacancies and group-V elements such as N, P, and As act as acceptors in ZnO. However, from theoretical calculation it comes out that these are deep acceptors and thus contribute only slightly to the *p*-type conductivity [52]. Nitrogen appears to be a good candidate for the hole doping of ZnO, but its practical application has not yet been demonstrated.

1.4.5 Magneto-transport properties

The transport properties of ZnO have been widely studied under the effect of a magnetic field. The single, parabolic conduction band of ZnO (see Figure 1.9) allows an easy interpretation of the Hall effect for the determination of the carrier density and mobility. Especially in strong accumulation layers, quantum interference phenomena have been found in ZnO and they are

studied under the effect on an applied magnetic field like the works found in References [72, 76, 77, 78], to cite a few.

1.4.6 ZnO as TCE

One of the promising application for ZnO is as transparent conducting electrode. The ability to easily produce high quality thin-films on a transparent substrate (glass or quartz for example) makes ZnO a very attractive material in this field. If its transparency is high thanks to its large band-gap, on the other hand, like in the case of graphene, its conductivity needs to be modulated with doping in order to lower the resistivity of the film. As mentioned before, Al doping is a commonly used technique for the fabrication of conductive ZnO for displays applications [68] or light emitting diodes [55]. However as said above Al doping has some drawbacks especially in terms of transparency of the doped thin-film which is significantly altered.

Chapter 2

Experimental

This chapter will describe in detail the techniques used for the fabrication of the graphene and ZnO samples, their characterization and the final device realization. The fabrication of graphene samples has been carried out with two techniques: the *anodic bonding* and the transfer of CVD graphene (commercially available) onto a glass substrate. The zinc oxide samples have been realized with the magnetron sputtering method. The samples are characterized after the production with an optical microscope, atomic force microscopy (AFM), Raman spectroscopy and X-ray diffraction (XRD). Finally the samples are contacted for electrical characterization with the evaporation of metals and shaped with different techniques. Finally, a description of the low-temperature magneto-transport system will be given.

2.1 Samples fabrication

In this section we introduce the different techniques used for the fabrication of the graphene and ZnO samples. For the production of graphene samples we used the anodic bonding method and the transfer of CVD graphene onto a glass substrate and for ZnO the radio-frequency magnetron sputtering.

2.1.1 Glass substrates involved

In this thesis two kind of glasses have been used as substrates for all experiments concerning both the sample fabrication and space charge doping: the first is SCHOTT™ D263T, a borosilicate glass, and the second is soda-lime glass also from SCHOTT™. There are differences in composition between the two types of glasses which affect the properties of the samples deposited on them (as we will see in Chapter 3), the most important being the maximum reachable carrier concentration due to space charge doping. The latter is affected by an important parameter of the glass, which is also the most relevant for our purpose, that is the sodium ion content. In the D263T

the Na^+ concentration is $\sim 1.4 \times 10^{18} \text{ cm}^{-3}$ while in the soda-lime it is $\sim 3.4 \times 10^{18} \text{ cm}^{-3}$. As will be confirmed by the experiments, this difference in concentration gives a higher doping capability to the soda-lime with respect to the borosilicate glass.

2.1.2 Graphene

Anodic Bonding

Anodic bonding is known in microelectronics to be a reliable method for sticking two surfaces without any intermediate layer like glue, provided that they are microscopically clean and polished. The original technique was used to stick silicon to a glass substrate [16, 79] or to stick two silicon surfaces with a glass layer in between. As mentioned in Chapter 1, anodic bonding can be used for the fabrication of two-dimensional materials, included graphene, in an original and reliable way [4, 18, 19, 20, 80].

Anodic bonding is based on the fact that glasses are ionic conductors at relatively high temperatures. They are formed by an amorphous network of SiO_2 and the introduction in the system of Na_2O and CaO breaks some Si-O-Si bridges. Non-bridging oxygen atoms serve as anions for Na^+ and Ca^{2+} ions. At the bonding temperature ($60^\circ\text{C} < T < 300^\circ\text{C}$) Na ions become mobile under an applied electric field (the mobility of Na^+ being much higher than the mobility of Ca^{2+} [17]) and it is possible to deplete the surface from sodium ions. A space charge of uncompensated oxygen ions (which are not mobile) is thus left at the surface of the glass which creates an electrostatic field and attraction between glass and sample. In the case of the original technique, the intimate contact generated by the strong electrostatic field between glass and silicon ultimately leads to chemical bonding between Si and O at the interface; in the case of 2D materials, as described below and for the parameters used the sticking process is purely electrostatic.

The schematics of our anodic bonding machine are depicted in Figure 2.1. It is composed of a controller (for the regulation of the heat and the voltage), an apparatus formed by a hot plate, which also serves as anode for the system, and an anvil (the cathode) at the ground potential which can be substituted by a micro-manipulator tip. Between the anode and the cathode is placed the glass substrate with the precursor of the nanomaterial to be fabricated. The choice of the precursor is a crucial step in the sample fabrication. The precursor is usually a lamellar bulk material from which are cleaved thin fresh flakes of 1 – 2 mm in lateral size with the help of adhesive tape. The precursors are placed on the surface of a glass substrate (borosilicate or soda-lime glass) which has been previously cut to $\sim 1 \text{ cm}^2$ and cleaned in a ultrasound bath at 35°C first in acetone and then in ethanol, 5 minutes each, and dried with nitrogen. The glass/precursor system is then placed on the hot plate, the anvil (or the micromanipulator tip) is put

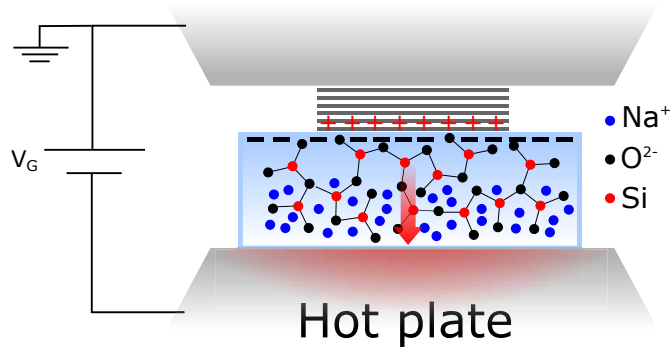


Figure 2.1: Schematics of anodic bonding. The motion of the Na^+ ions under the electric field is highlighted with the red arrow. The top anvil can be substituted by a micromanipulator tip.

on top in contact with the precursor and the voltage is applied between the anvil (tip) and the hot plate. As highlighted in Figure 2.1 this cause Na^+ ions drift towards the anode leaving a space charge of O^{2-} at the interface between the glass and the precursor. After some time, the space charge reaches its optimal magnitude such that there is a sufficient image charge in the precursor. The voltage can thus be removed with the precursor electrostatically stick to the glass. With the help of adhesive tape, the top layers of the precursor are peeled off, leaving on the surface of the glass one to few-layers of material bonded to it. This technique has a high throughput compared to the purely adhesive tape technique [2] and is capable of giving relatively big sized samples (of the order of $\sim 100 \mu\text{m}$ for graphene) of excellent quality.

Two type of glasses are used in this thesis for the fabrication of anodic bonded graphene: borosilicate glass purchased from SCHOTTTM and standard soda-lime glass, both optically polished. The ionic conductivity of the soda-lime glass (Na^+ ion concentration $3.4 \times 10^{18} \text{ mm}^{-3}$) is higher than that of borosilicate glass (Na^+ ion concentration $1.4 \times 10^{18} \text{ mm}^{-3}$) and this is also reflected on the magnitude of the parameters used for anodic bonding.

The parameters for the fabrication of 2D samples with the anodic bonding method vary from material to material. The sample is heated at a temperature of $140 - 250^\circ\text{C}$ applying a voltage of $200 - 1500 \text{ V}$ for $1 - 15$

minutes. Several samples have been fabricated during this thesis and the optimum parameters for the fabrication of graphene have been found, both for the borosilicate and soda-lime glass using the anvil or the micromanipulator tip. The details will be given in Chapter 3.

Transfer of CVD graphene

As mentioned in Chapter 1, chemical vapour deposition (CVD) is a widely used technique for the production of large surfaces of graphene. The graphene sheet is fabricated by heating a Cu foil at $\sim 1000^\circ\text{C}$ in the presence of carbon carrier gases [11]. The Cu foil acts as a catalyzer for carbon which is deposited on its surface and crystallizes into graphene. The principal advantage of using this technique is that the area of the graphene sample is only limited by the size of the copper foil. Furthermore, the quality of the graphene film produced is compatible for electronic applications, though it is still not comparable with the quality of anodic bonded graphene or graphene produced with the adhesive tape method.

As-fabricated CVD graphene cannot be used for electronics because it is grown on a conducting substrate (the Cu foil). A transfer process of graphene onto an insulating substrate is thus necessary. The *polymer assisted transfer* is the most widely used technique in research [81] and is a delicate step for the realization of electronic devices with CVD graphene. In the following, the transfer process of CVD graphene used in this thesis will be described in details.

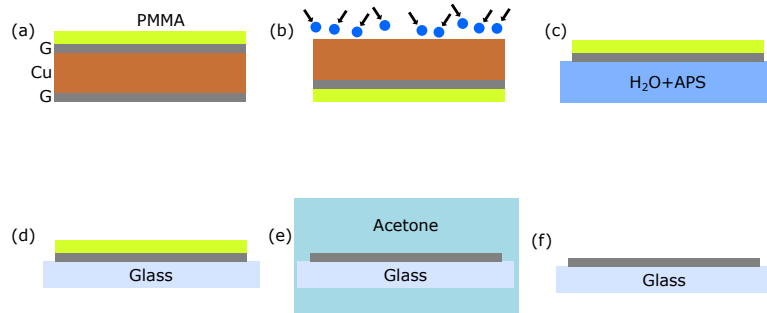


Figure 2.2: Steps of the transfer of CVD graphene onto a glass substrate. (a) PMMA is spin-coated on one side of the copper foil, covering the underlying graphene. (b) Oxygen plasma etching is performed on the back side to remove graphene not covered by the PMMA. (c) Copper is etched away in an aqueous solution of APS. (d) The floating graphene/PMMA is rinsed several times in DI water and then is “fished” with the glass substrate. (e) The glass/graphene/PMMA system is let dry in air and, after a baking to enhance adhesion, the PMMA layer is dissolved in acetone. (f) Finally, graphene has been transferred onto the glass substrate.

- A square of $\sim 1 \text{ cm}^2$ is cut from the copper foil which is covered with graphene on both sides.

- The Cu square is fixed to a kapton support with the help of adhesive tape. This step is necessary to ensure mechanical support to the sample in the next step of spin coating.
- Polymethyl methacrylate (PMMA) is spin-coated on the sample at a speed of 1000 rpm for 1 minute (Figure 2.2a) in order to create a thin film of polymer on the surface of the graphene layer. It will be used as mechanical support. The PMMA is let dry in air at room temperature for an overnight period to let evaporate the solvent.
- The kapton support is removed and a oxygen plasma etching is performed on the back side of the copper foil (the one not covered by the PMMA) to remove the graphene from that side of the copper, as showed schematically in Figure 2.2b. This step is very important to ensure the success of the copper etching step. The O₂ etching is done at 60 W for 150 seconds.
- A solution of ~ 1 g of Ammonium Persulfate (NH₄)₂S₂O₈ (APS) in 85 mL of de-ionized water is prepared (concentration of ~ 0.01 g/mL). APS is an oxidizing agent for the copper [82]. A higher concentration should not be used in order to avoid bubbles in the solution which will result to be holes in the deposited graphene. With this concentration, the etching process takes about four hours. The sample must be placed on the surface of the solution with the PMMA-face of the stack outside of it. At the end of the process, the PMMA-graphene stack should float on the surface of the solution.
- After the copper is completely etched away, the sample must be rinsed in de-ionized water. The sample is then transferred in a watch-glass (circular, slightly convex piece of glass) where de-ionized (DI) water is added and then is pumped away several times (always taking care of letting the sample float on some water) in order to remove any trace of the etchant. The sample is then placed in a DI water bath. The process is then repeated.
- A glass substrate (borosilicate or soda-lime) is cut (with an area at least 50% bigger than the PMMA area) and cleaned in ultrasound first in acetone (4 minutes, 35°C) then in ethanol (4 minutes, 35°C) and dried by blowing nitrogen.
- The floating graphene/PMMA stack is caught on the glass substrate and let dry in air for 30 minutes. A baking at 150°C for 5 to 10 minutes is then performed to enhance the adhesion of graphene to the glass surface.
- An acetone bath is warmed at $\sim 50^\circ\text{C}$ and the sample is immersed in it for 5 minutes to dissolve the PMMA layer. Then it is put in ethanol

for 3 minutes to remove the residues. This process is repeated a second time. Nitrogen gas is blown on the sample at the end of the process to dry the sample.

- A second baking is performed at 150°C for 5 minutes to further enhance the adhesion of graphene to the substrate.

After all those step the sample is ready for characterization and contacts deposition with the techniques described later in this chapter.

2.1.3 Zinc oxide

In this thesis we fabricated thin film zinc oxide on glass with the radio-frequency (RF) magnetron sputtering technique. RF magnetron sputtering is a straightforward, low cost technique from which is possible to obtain high quality ZnO films through a plasma assisted deposition method [52, 60, 61, 63].

The apparatus of the RF sputtering system is illustrated in Figure 2.3. It is composed by a vacuum chamber in which is present a high purity zinc

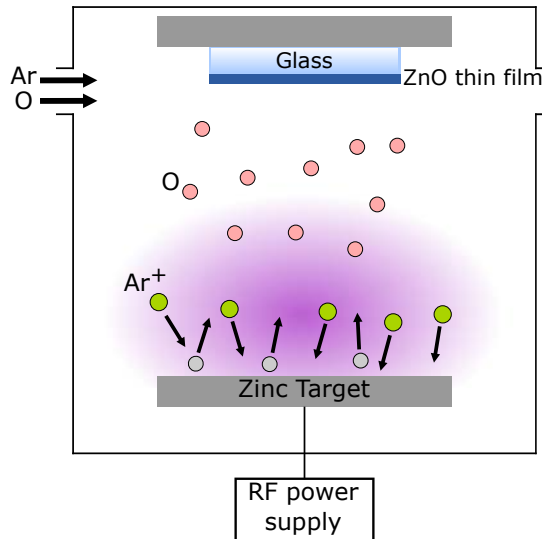


Figure 2.3: Schematization of the RF magnetron sputtering apparatus. In a high vacuum chamber, a glass substrate is placed in front of a zinc target. Argon and oxygen are introduced in the chamber and an argon plasma is activated with the RF power supply. Argon ions hit the zinc substrate expelling Zn atoms from it which travels towards the glass substrate. During their path they enter the oxygen atmosphere, oxidize and deposit onto the glass substrate in the form of ZnO.

or zinc oxide target in front of which, at a certain distance, is placed the

substrate where ZnO has to be deposited. The substrate can be eventually heated. The RF power is applied to activate the argon plasma (the pink shadow in Figure 2.3) causing Ar ions to hit the zinc target. Zn atoms are kicked away and travel towards the glass substrate. During their path they oxidize because of the oxygen atmosphere and deposit on the substrate as zinc oxide. The properties of the final ZnO film such as the stoichiometry, the crystallinity and the thickness are determined by the growth parameters: RF power, Ar and O partial pressure, substrate temperature, distance of the substrate from the target and deposition time [83]. The O/Ar ratio in the chamber is an important parameter for the determination of the stoichiometry of the deposited zinc oxide film. In particular, oxygen vacancies create mid-gap states in ZnO and contribute to the intrinsic *n*-type conductivity [65]. The substrate temperature can affect the deposition rate and the quality of the sample, in terms of grain size and crystallinity, though good results can be obtained also at room temperature.

2.2 Characterization methods

Several techniques have been used to characterize the samples fabricated during this thesis. They are: optical characterization with an optical microscope, atomic force microscopy (AFM), Raman spectroscopy and X-ray diffraction (XRD).

2.2.1 Optical microscope

The optical microscope is a useful tool for a first characterization of the graphene and ZnO samples. The images of the samples are recorded with a Leica DM2500 and a CCD camera with 5X, 10X, 50X and 100X objectives in the bright field imaging mode. For the case of anodic bonded graphene, the optical microscope characterization is useful to determine the number of layers of the sample through the optical contrast while for CVD graphene and zinc oxide it is useful to determine the quality of the surface of the sample.

2.2.2 Atomic Force Microscopy

Atomic force microscopy (AFM) was invented in 1986 [84] as an evolution of the Scanning Tunneling Microscope (STM). It is a tool which is able to scan the surface of a sample to obtain a topography at extremely high resolution. Contrary to STM which measures the tunneling current between the sample and the scanning tip, AFM measures the forces at the atomic scale and thus it makes possible to scan conductive and insulating samples [85]. The basic principles is described in the following.

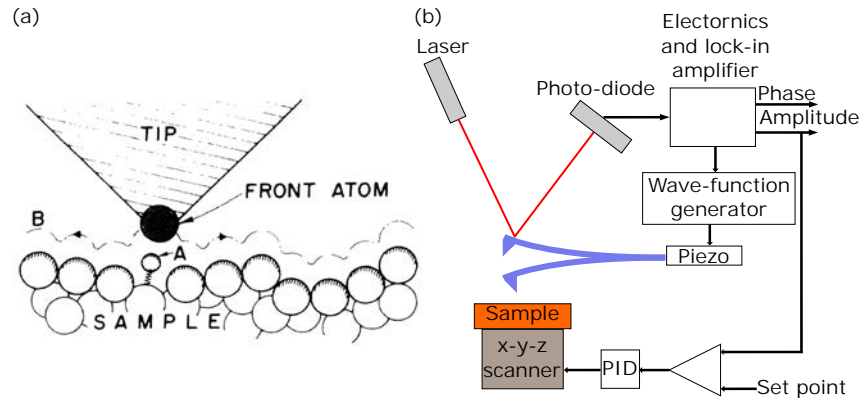


Figure 2.4: (a) Illustration of the basic principle of the AFM. The tip is ideally one atom sharp. The control system maintains a constant interaction force between the tip and the sample, following the contour B. Image reprinted from [84]. (b) Schematics of the AC operating mode of the AFM. A function generator causes the oscillation of the tip through a piezo. A laser hits the back of the cantilever and the light is reflected on a photo-diode which measures the deflection of the cantilever. A lock-in amplifier is connected to the photo-diode to measure the difference between the function generator and the actual oscillation frequency of the cantilever. The output of the amplifier is sent to the feedback loop which adjust the height of the sample.

The AFM is based on the interaction forces between the surface of the sample and a probing tip attached to a cantilever-like spring. In response to those forces the cantilever is deflected. The image of the surface of the sample is taken recording the deflection, which is shown as a z -displacement, as a function of the coordinates in the $x - y$ plane. Displacements from $1 \mu\text{m}$ to 0.1 \AA can be measured. The typical order of magnitude of the measured forces range from 10^{-6} to 10^{-11} N which makes possible to do a non-destructive scan of the surface. Three operating modes are distinguished: the contact mode, the non-contact mode and the tapping mode, also called AC mode. In the contact mode, the sample-tip separation is of the order of the \AA and the tip is sensible to the ionic forces which makes possible to reach atomic resolution under certain conditions. In the non-contact mode the tip operates at higher distance from the sample, $10 - 100 \text{ nm}$. For these two modes, the force between the tip and the surface of the sample causes the cantilever to bend until static equilibrium is reached. The scanning can be done either by maintaining the sample-tip distance constant and regulating the sample height through a feedback loop, or by recording the displacement of the cantilever in response to the interaction with the surface. Finally, in the AC mode the tip-sample distance is in between of the distances of the two previous modes and the tip vibrates at a frequency close to its resonance frequency. A distance-frequency curve dominates the system: a repulsive force will increase the resonant frequency of the cantilever, while an attractive force will decrease it. The feedback loop can keep the oscillating amplitude constant or it can maintain the frequency

constant during the scan [85], in both cases a measure of the height as a function of the position can be done.

The three operating modes have some advantages and disadvantages when applied to 2D samples and thin films of materials. With the contact mode, high speed scans and atomic resolution are possible; also, it is easier to scan rough samples. However, strong lateral forces are involved due to the proximity of the tip to the sample. In the non-contact mode the lateral forces involved are much smaller thus avoiding distortions of sample surface. However, the relatively high sample-tip separation doesn't allow a high resolution imaging. Moreover, the contact and non-contact modes are usually performed in ultrahigh vacuum to reach the atomic resolution, which is a condition not achievable on our setup. The AC mode is thus the best choice for the measures on graphene and ZnO thin films. It in fact involves small lateral forces on the sample together with high resolution and the possibility to perform the scan in ambient condition. The scan speed is however slower compared to the contact mode.

The setup used in this thesis for AFM measurements is a Scanning Probe Microscope SmartSPM-1000 instrument (AIST-NT) and the tapping mode was used in all the performed scans. In Chapter 3 and 4 will be shown the AFM images of graphene and ZnO samples.

2.2.3 Raman Spectroscopy

Raman spectroscopy is a powerful and non invasive tool for the characterization of materials. It is based on the Raman effect, a phenomenon of light scattering discovered in 1928 by C. V. Raman and K. S. Krishnan which led C. V. Raman to be awarded the Nobel prize in 1930 [86]. The origin of this phenomenon comes from the interaction of an incident light beam with the phonons in a solid or from molecular vibrations in molecules, producing inelastic scattering of light. When light hits a material, the most part of the phonons experience elastic scattering, called Rayleigh scattering and the intensity of this portion of light is $\sim 10^{-3}$ times the intensity of the incident light. The portion of light which undergoes the Raman scattering is even less, $\sim 10^{-6}$ times the intensity of the incident light. In the following, the principles of the Raman scattering will be explained.

The principles of Raman scattering

The explanation of the Raman effect can be understood in terms of the polarizability of molecules or the susceptibility of crystals. Let us consider a two-atom system. When an electromagnetic (EM) wave interacts with such a system, the electronic cloud and the nuclei will react to the incident electric field, thus inducing a change in the dipole moment

$$\mathbf{P}_D(\omega) = \alpha_0 \mathbf{E}(\omega) \quad (2.1)$$

where $E(\omega)$ is the incident radiation, α_0 is the polarizability and $P_D(\omega)$ is the dipole moment which acts as a source of evanescent EM wave. α_0 is a measure of the deformation induced in the system in the presence of an external electric field. In a solid crystal, the susceptibility tensor takes the place of α_0 .

Suppose now that the molecule is vibrating with frequency Ω and the distance between the two atoms changes periodically. Then, α_0 will be modulated and Eq. 2.1 takes the form

$$\mathbf{P}_D(\omega) = (\alpha_0 + \alpha_1 \cos(\Omega t)) \mathbf{E}_0(\omega) \cos(\omega t) \quad (2.2)$$

which, with the application of trigonometric rules, becomes

$$\mathbf{P}_D(\omega) = \alpha_0 \mathbf{E}_0 \cos(\Omega t) + (\alpha_1 \mathbf{E}_0 / 2) [\cos(\omega + \Omega) t + \cos(\omega - \Omega) t] \quad (2.3)$$

From Eq. 2.3 we see that the scattered light oscillates at the frequency of the incident light ω and at the sideband frequencies $\omega \pm \Omega$. The side band frequencies are called Raman Stokes ($\omega - \Omega$) and Raman anti-Stokes ($\omega + \Omega$) frequencies.

In a quantum-mechanical picture, the Raman scattering comes from an exchange of energy between an incident photon and a vibrating mode of the crystal, *i.e.* a phonon. The photon is absorbed by an electron which is in a ground energy state and is excited in a virtual state (Figure 2.5). When it recombines it can either return to the ground energy state and emit light at the same frequency of the incident light (Rayleigh scattering) or recombine at a different energy level and emit light at a different frequency (Raman scattering). Since the energy and momentum must be conserved, the generation or absorption of an additional quasi-particle (a phonon) is required. Figure 2.6 shows an example of a measured Raman spectrum composed by the Rayleigh scattering and the Stokes and anti-Stokes frequencies. The Raman effect is thus a consequence of the polarizability of the system and

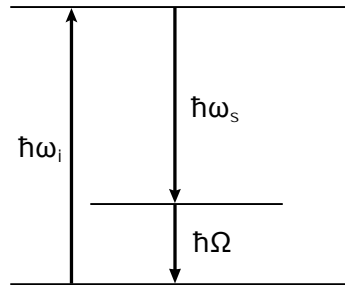


Figure 2.5: Schematics of the absorption process of a photon, re-emission of a photon with different energy due to energy exchange with a phonon.

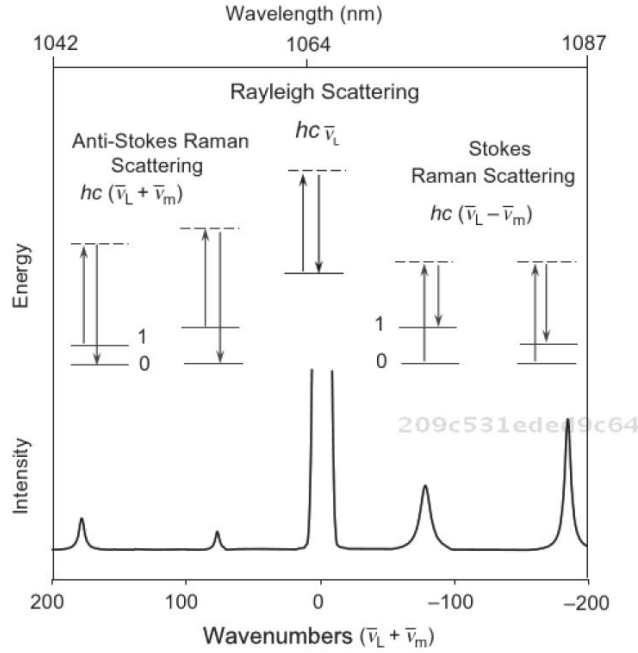


Figure 2.6: Illustration of the Rayleigh, Stokes and anti-Stokes scattering. Re-printed from [87]

if the vibration of a molecule (or a phonon mode in a crystal) is such that there is no polarizability, that vibration is said to be *Raman inactive*. Thus the condition for a vibration mode to be *Raman active* is

$$\left(\frac{d\alpha}{dQ}\right)_0 \neq 0 \quad (2.4)$$

with dQ the displacement from the equilibrium position.

Raman microscopy in 2D materials

In the case of 2D materials and thin films Raman spectroscopy represents a fast and non destructive tool for the study of the properties of the materials. From the frequency and relative intensities of the Raman peaks it is possible to characterize the quality, doping level and strain of the sample. Micro-Raman spectroscopy is the term used to indicate that the analysed area is of the order of the μm^2 and this is achieved focusing the laser with the help of a microscope objective. The Raman measurements done in this thesis were performed using our Xplora Raman spectrometer (Horiba Jobin-Yvon) in back scattering geometry in ambient conditions. In Figure 2.7 is shown the layout of the internal optical system for the detection of the Raman signal.

The main parts of the micro-Raman systems are shown: the laser, the microscope, the confocal system and the spectrograph. The lasers wavelength available are 532 and 638 nm but for our measurements we used only

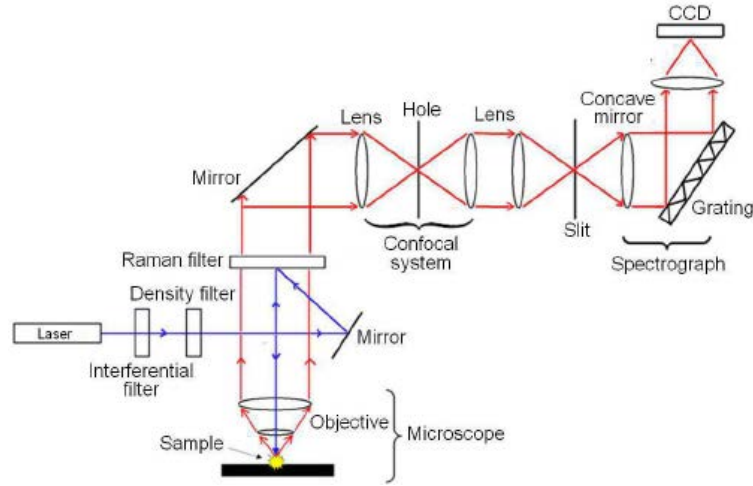


Figure 2.7: Schematic of the micro-Raman system.

532 nm. The laser power on the sample of the 532 nm laser is 12 mW, but the intensity of the radiation is often reduced to avoid heat damage on the samples. Usually, the measurements on graphene and ZnO are carried out with the 50% or 25% filters, meaning a laser power on the sample of 6 and 3 mW, respectively. The microscope part is a crucial component of the system since it is responsible for the spatial resolution of the measure. Our system is equipped with three objectives: 10X, 50X and 100X. The 100X objective has been used for all the measurements on 2D materials and thin films in this thesis because, thanks to its numerical aperture (NA) of 0.9, it is the objective with the best axial resolution, compared with the 10X and 50X. The laser spot of the 100X objective is $0.72 \mu\text{m}$ with the 532 nm laser. The confocal system is composed of a slit, a hole and various lenses. The slit is responsible for the spectral resolution and hole for the axial resolution. Finally, the spectrograph is composed by a series of lenses and a grating, which separates the different wavelengths of the Raman signal. The grating resolution can be changed, determining the number of points in the Raman spectrum. The best resolution that we can get with our system is $\sim 1.2 \text{ cm}^{-1}$. However, higher resolution means longer acquisition time because less photons hit the CCD camera resulting in a weaker signal.

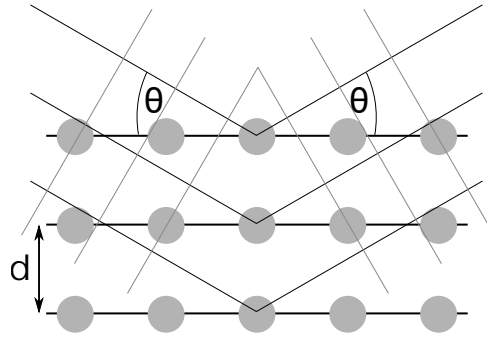


Figure 2.8: Illustration of the Bragg law.

2.2.4 X-ray diffraction

X-ray diffraction (XRD) is one of the most used tools to analyze the crystal structure of a material. Diffraction phenomena appear when an electromagnetic (EM) wave hits a periodic structure with the characteristic length of the order of the EM wave. Since in a crystal the spacing within atoms is of the order of the Ångström and the X-ray wavelength varies from 0.1 to 100 Å, the structural properties of a crystal can be studied by observing the diffraction pattern generated by a crystal when it is hit by an X-ray radiation. In the following, a quick description of the principle of XRD will be given without claiming to be complete.

We can treat a crystalline material as a set of parallel atomic planes placed at a distance d which interacts with the X-ray beam. The X-ray radiation is treated as a plane wave. When the radiation hits the sample with an angle θ (Figure 2.8) a portion of it will penetrate in the material and another portion will be reflected at the same angle of the incident wave. The reflected waves from the different planes will sum up producing constructive interference only if a certain condition is met, *i.e.* the well known Bragg's law

$$2d \sin(\theta) = n\lambda \quad (2.5)$$

where θ is the incident angle of the X-ray, d is the spacing between the atomic planes, λ is the wavelength of the incident wave and n has the meaning of

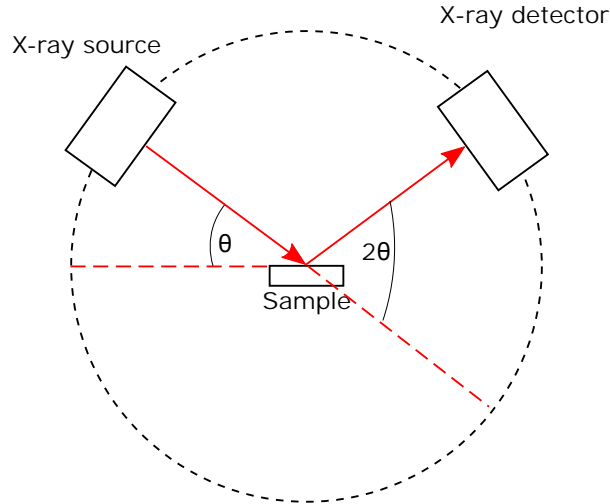


Figure 2.9: Schematization of the X-ray diffraction setup.

a reflection order. The above relation can be exploited in XRD in order to determine the crystalline orientation of the sample by sweeping in a certain range the angle of incidence of the X-ray beam and measuring the scattered waves as a function of the angle, as illustrated schematically in Figure 2.9. With this setup, the X-ray detector will measure a peak in the scattered wave only at certain angles, *i.e.* when the condition of Equation 2.5 is met.

Miller indices A convenient way to determine the orientation of the crystalline planes is represented by the *Miller indices*. A crystal can be seen as set of planes occupied by the atoms which are all parallel to each other and intersect the axes of the crystallographic unit cell. A set of indices hkl can be defined by considering the intersection points of the planes with the axis of the unit cell. The intersection points are thus a/h , b/k and c/l , with a , b and c being the axis of the unit cell. As an example, a plane identified by the Miller indices (121) will intercept the axes a , b and c of the unit cell at the coordinates 1, $1/2$ and 1 respectively. In X-ray diffraction the Miller indices are thus used to determine the different crystalline orientations present in a crystal, each peak of the diffraction pattern corresponding to a different crystalline orientation.

Grain size estimation XRD gives also information about the mean grain size of the analyzed crystal. The samples we analyze with XRD are far from

being a monocrystal, mainly because of the growth conditions, their extremely small thickness and because the substrate (the glass) is amorphous. They are instead polycrystalline, which means that they are formed by many small single crystals one close to another. Besides the orientation of the single crystals of the sample, XRD gives information also about the average size of the grains composing the sample and they are estimated with the well known *Scherrer equation* [88]

$$\tau = \frac{K\lambda}{\beta \cos \theta} \quad (2.6)$$

with τ the mean grain size, K a dimensional factor close to unity, λ the wavelength of the X-ray radiation, β the broadening of the diffraction peak at the half of his intensity, or full width half maximum (FWHM) and θ is the Bragg angle. The grain size estimated with this formula can be compared to the grain size measured with the AFM for further confirmation of the data.

Grazing geometry For samples of extremely low thickness, like is the case of our ZnO samples, the classical theta-2theta configuration in the X-ray diffraction analysis could not be sufficient to obtain a perceptible signal on the detector. In this cases a grazing geometry is used. Instead of sweeping the X-ray source together with the detector in a range of angles it is kept at a constant, small angle in order to maximize the penetration of the X-ray inside the material and enhancing the coherent diffraction signal. However, the signal which reach the detector is now the convolution of all the signals coming (in the worst case) from all the surface of the sample resulting in a broadening of the diffraction peaks [89]. For a correct estimation of the grain size it is thus not sufficient to use the FWHM of the peaks in the diffraction pattern, but instead a pseudo Voigt fit of the peak should be done and only the FWHM of the Lorentzian part of the fit should be used in the Scherrer equation (Equation 2.6).

2.3 Device fabrication

Once the materials are deposited on glass and fully characterized with the methods described above, the devices are fabricated. This in general involves two steps: first, the sample must be shaped in order to make its shape compatible with the electrical measurements and second, the metal contacts are deposited with the help of a shadow mask. The shape of the sample is an important aspect because it affects the validity of the measured resistance. We chose the van der Pauw method for the electrical measurements which is a reliable method for the measure of the sheet resistance of a thin sample. The van der Pauw method is briefly explained in the following.

2.3.1 Van der Pauw method

The van der Pauw method for resistivity and Hall measurements was developed in 1958 by L. J. van der Pauw [90] and provides a useful measurement for the determination of the resistivity thin samples of arbitrary shape, provided that there are no holes in the sample. Also, it is possible to measure the Hall effect simply by selecting specific contacts for current injection and voltage measurement. In the practice, square sample with metal contacts at the corners are often used. The contacts must also be small compared to the dimension of the sample. The contact configuration for sheet resistance (R_S) measurements is shown in Figure 2.10a. The current is injected from

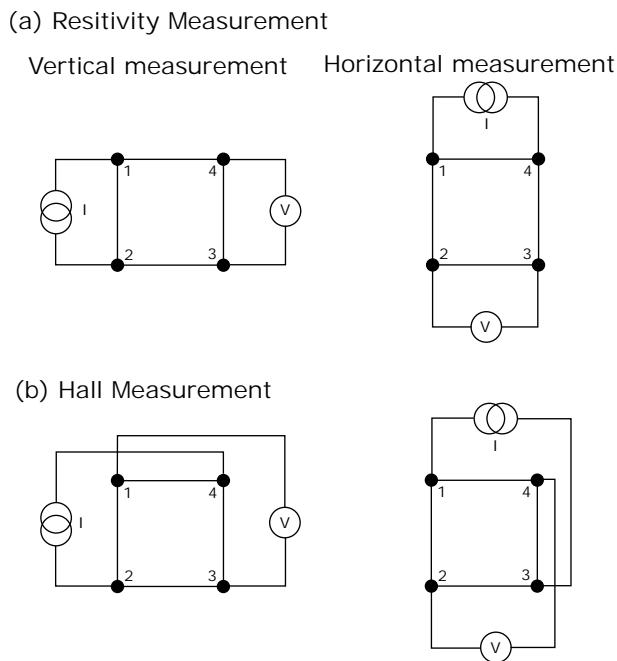


Figure 2.10: Contact configuration in the van der Pauw method for (a) R_s measurements and (b) Hall measurements.

one contact and collected from one of the adjacent contact while the voltage is measured from the opposite pair of contacts. This is repeated for all possible pairs of contacts and it is possible to define a set of resistances from the measured voltage from a pair of contacts divided by the current injected from the opposite pair of contacts. For example, the $R_{AB,DC}$ is calculated from the ratio V_{DC}/I_{AB} . Averaging between the various resistances we can finally define a vertical and a horizontal resistance resulting from the average of the resistances calculated by flowing the current in the device vertically or horizontally, respectively, denoted as R_V and R_H . From these

two values, the R_S is derived from:

$$R_S = \frac{\pi}{\ln(2)} \frac{R_V + R_H}{2} f \quad (2.7)$$

f is a correction factor which takes into account the inhomogeneity of the sample through the ratio r , which is defined as R_V/R_H if $R_V < R_H$ or R_H/R_V if $R_H < R_V$. f is thus equal to

$$\cosh\left(\frac{r-1}{r+1} \frac{\ln(2)}{f}\right) = \frac{1}{2} \exp\left(\frac{\ln(2)}{f}\right) \quad (2.8)$$

f is always equal to or smaller than 1 (it's 1 when $r = 1$) and it is not derivable analytically. In the practice for R_S measurements a polynomial approximation can be used.

Hall measurements The van der Pauw geometry is suitable also for the measurement of the carrier density and charge mobility through the Hall effect. In this case, the contact configuration used is the one depicted in Figure 2.10b. The current is applied along the diagonal of the sample and the voltage is measured on the other diagonal while the magnetic field is applied perpendicular to the sample plane and swept. In general, when a sample is crossed by a current and a magnetic field is applied perpendicular to it, a voltage (called Hall voltage) appears in the direction perpendicular to the current and to the magnetic field, whose amplitude is given by

$$R_{Hall} = \frac{V_{Hall}}{I} = \frac{B}{qn_S} \quad (2.9)$$

where n_S is the surface charge density and q is the charge of the charge carriers (+/- times the electron charge e). The sign of V_{Hall} is determined by the type of charge carrier present in the material, either electron or hole. From this measurement and the measurement of the sheet resistance at $B = 0$ it is possible to derive the Hall mobility as $\mu_H = 1/(en_S R_S)$.

In our measurement system for the study of the electronic transport it is possible to measure simultaneously R_S as a function of the magnetic field (the *magneto-resistance*) and the Hall effect as shown later in this chapter.

2.3.2 Contact deposition

The deposition of the metal contacts is done by thermal evaporation of gold through a stencil mask. This is a fast and clean method for the deposition of the contacts. The stencil mask is a steel foil on which the shape of the mask is engraved with a laser beam. The mask is aligned to the sample with the help of micromanipulators and is stuck onto it with double adhesive tape (Figure 2.11). The stencil mask method can be considered a clean method

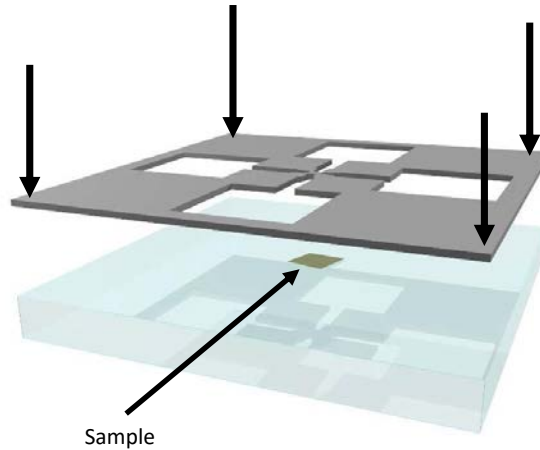


Figure 2.11: Schematization of the alignment of the stencil mask to the sample.

for the deposition of metal contacts because, contrary to photolithography or electron beam lithography, it doesn't require the deposition of a polymer on the surface of the sample, thus avoiding contamination. On the other hand, the achievable resolution for the contact dimension is much less for the stencil mask compared with the other methods, but is still acceptable for our samples. In Figure 2.12 are shown the two types of stencil mask we used, both in the van der Pauw geometry. One type of mask is for macroscopic samples and the contacts are placed 1.5 mm apart in a square geometry. This kind of mask has been used for the measurements on CVD graphene and ZnO. The other type of mask is for microscopic samples, with the contacts being at the distance of 40 μm , always in a square geometry. This kind of mask has been used for contacting anodic bonded graphene of a minimum lateral size of about 50 μm .

2.3.3 Sample shaping

As said before, the sample shape is an important factor in the electronic transport measurements. In order to properly shape our samples we used different methods, depending on the precision we wanted to achieve and the sample type. We used three techniques: shaping of graphene (CVD or anodic bonded graphene) with a micromanipulator tip, oxygen plasma etching on CVD graphene and dissolution of ZnO in HCl. All the methods

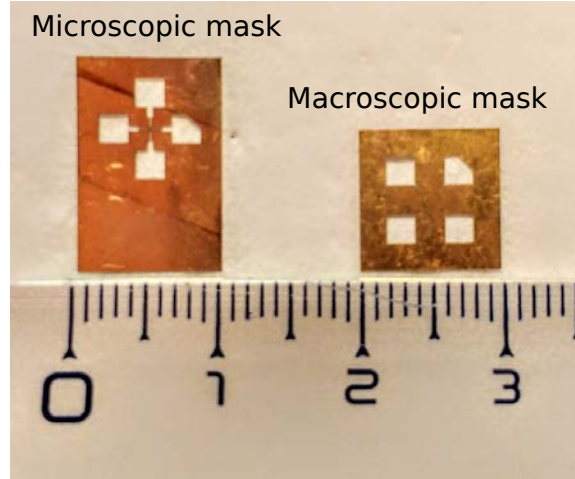


Figure 2.12: The two types of masks we used for the contact deposition. On the left is shown the mask used for contacting microscopic samples of lateral size of $50\ \mu\text{m}$. On the right, the mask used for macroscopic CVD graphene and ZnO samples is shown.

will be briefly discussed below.

Shaping with micromanipulator tip The most direct and straightforward method to shape a 2D sample is to scratch it with a micromanipulator tip in order to give it the desired shape. Of course, the achievable resolution of the scratch is limited by the precision of the movements in the xy plane of the micromanipulator and the radius of the tip. Most of the CVD graphene and all the anodic bonded graphene were shaped using this method because graphene can be scratched away relatively easily.

Plasma etching shaping Oxygen plasma etching is often used to shape graphene into Hall bars or nanoribbons [91, 92]. We performed the plasma etching in a reactive ion etching system in order to shape our CVD graphene samples for electronic transport measurements. Before the etching procedure, an electron beam lithography step is necessary. The e-beam lithography is a procedure used to create patterns in an electron-sensitive polymer (like PMMA) through the exposure to an electron beam. It is a widely used technique in research and nanotechnology because it is possible to create patterns of extremely high resolution (of the order of few nanometers). The parts of the polymer exposed to the electron beam become soluble in a proper solvent with the final result that all the sample is covered by the polymer except in the area where it was exposed to the e-beam. This technique was used to create a pattern compatible with the van der Pauw

method on our CVD graphene sample. The sample was subjected to the oxygen plasma and only the parts uncovered by the PMMA were etched away. The results will be shown in Chapter 3.

ZnO etching ZnO shaping is quite hard to achieve with the micromanipulator tip because it is a tough material. Instead, a straightforward way to etch ZnO in order to give it the proper shape is to put it in a aqueous solution of hydrochloridric acid (HCl). HCl etching of ZnO is usually performed in order to texture its surface in solar cells applications [93]. For our purpose, where we want to completely remove part of the ZnO on the glass, we used an aqueous solution of HCl at 15%. A drop of PMMA with a diameter of about 2 – 3 mm is put on the center of the glass substrate on which is deposited ZnO on the whole surface. PMMA is then left to dry in air at a temperature of ~ 50 °C for 15 minutes. Then, the substrate is put in the solution of HCl for 7 seconds letting the acid completely remove the ZnO not protected by the PMMA; it is then rinsed in de-ionized water and dried with nitrogen gas. 7 seconds is a sufficient time to completely remove the few nanometers of ZnO from the surface. PMMA is then dissolved in warm acetone (~ 50 °C) for 30 minutes.

2.4 Electronic transport measurements setup

Space charge doping, electronic transport and Hall measurements are all carried out under high vacuum ($< 10^{-6}$ mbar) in a custom made continuous He flow cryostat. It allows to control the temperature of the sample in the range 3 – 420 K, thus allowing to perform the doping of the samples and the low temperature transport measurements *in situ*. The cryostat is held inside an electromagnet capable of reaching a magnetic field of 2 T. The doping and resistivity measurements are controlled by a LabVIEW program which coordinates the measurement instruments and saves the data into a file.

Chapter 3

Space Charge Doping

This chapter is partially based on our publication: A. Paradisi, J. Biscaras and A. Shukla, Space charge induced electrostatic doping of two-dimensional materials: Graphene as a case study, Applied Physics Letters, 107, 143103 (2015) [94].

During this thesis we have developed and patented a technique called *space charge doping* for ultra-high, ambipolar, electrostatic doping of materials deposited on a glass substrate. In this chapter as well as those that follow the technique will be detailed and its application to graphene and zinc oxide will be analysed. Space charge doping was first tested on graphene for the following reasons: (i) graphene has been studied extensively and there is an extensive bibliography covering a great number of topics allowing an easier interpretation of the results; (ii) the graphene band structure, as we saw in Section 1.3.1, makes graphene a zero band-gap semiconductor and it is possible to perform electron or hole doping quite easily; (iii) it is easy to produce high quality graphene with our *Anodic Bonding* technique (Section 2.1.2) or to transfer large area of CVD graphene on a glass substrate; (iv) we wanted to investigate an alternative way to produce an efficient transparent conducting electrode (TCE) using graphene doped with space charge doping. In literature many publications work with graphene as a base material for a TCE [13, 14, 43], using different techniques for lowering graphene sheet resistance and make it more conductive through doping. In the process these works highlight several problems related, among others, to the damage to the graphene layer and instability of the doping over time. As we will see later in this chapter, space charge doping can overcome some of these problems.

In the first part of this chapter we will describe the principle of space charge doping followed by the details of the production of the graphene samples. Finally the results of space charge doping applied to graphene will be detailed and discussed.

3.1 The principles of space charge doping

To understand the working principles of space charge doping it is worthwhile to take a closer look at the structure of glasses in general and of ionic transport inside glass.

3.1.1 Glass atomic structure

It is known that glasses are formed by an amorphous network of certain glass-forming oxides which respect some rules [95]. Commercial glasses are formed by three-dimensional networks of SiO_2 , as in the case of soda-lime glass, with B_2O_3 also contributing in the borosilicate glasses. The building block of the glass atomic network is the oxygen tetrahedron which surrounds silicon atoms and each tetrahedron shares a corner with other tetrahedra. The angle between the different tetrahedra varies in an unpredictable way, and that is why the atomic structure of glass is considered amorphous. Network modifiers are added to the glass during the production in order to enhance certain properties. Sodium oxide (Na_2O) and calcium oxide (CaO) are the main compounds used as modifiers. The introduction of these species breaks some Si-O-Si bridges creating non bridging oxygen units which serve as anions for the Na^+ and Ca^{2+} cations which are incorporated in these sites. Oxygen atoms are linked covalently to the network and Ca^{2+} ions possess a very low mobility, making Na ions the most mobile species in glass. Figure 3.1 is a simplified and schematic representation of the structure of glass at the atomic level.

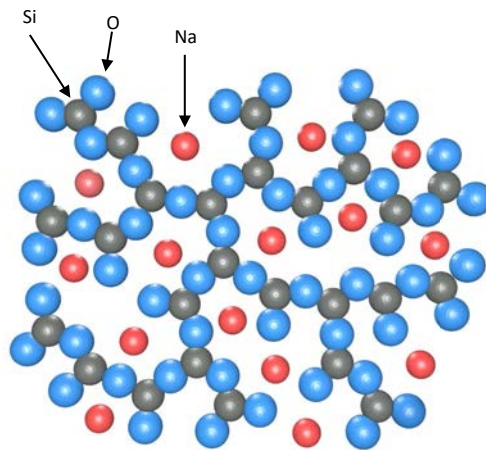


Figure 3.1: Schematization of the glass structure at the atomic level.

3.1.2 Ionic drift

In Reference [17] the mobility of Na^+ and Ca^{2+} ions in various glasses is studied, especially in soda-lime glass with a composition very close to that of our soda-lime glass. The conclusion is that Na^+ ions are the most mobile species in the glass. Figure 3.2 shows conductivity data of soda-lime glass extrapolated from Figure 2 in Reference [17] compared with our measurements on soda-lime glass used in this work. We measured glass conductivity

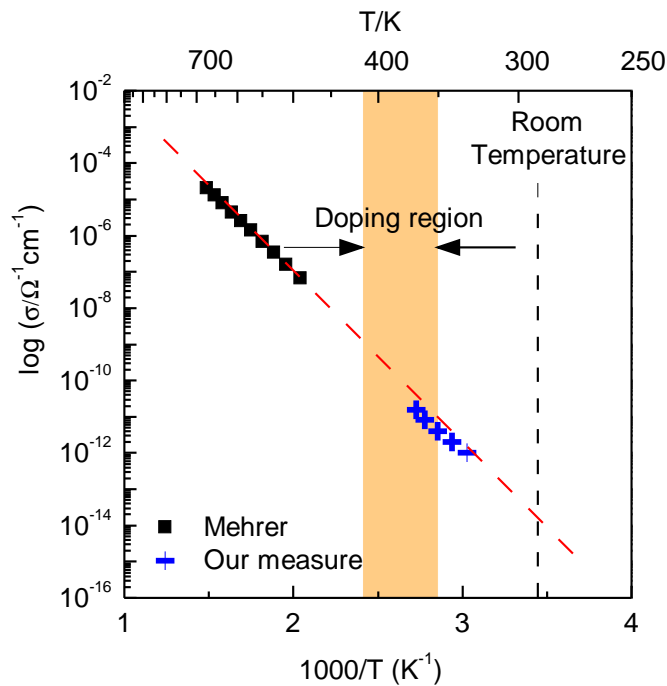


Figure 3.2: Measurements on the conductivity of our soda-lime glass with respect to temperature compared with the data in Reference [17]. The small offset of our data from the extrapolation of the published data is probably due to slight differences in the composition of the glasses.

by monitoring the DC current through glass with a constant applied voltage as temperature was increased. The data from [17] are extrapolated from the low frequency measurement of the conductivity as a function of the temperature. The first thing to notice is that our measurement is in good agreement with those from the article. The small shift of our data from the extrapolation of the published data from [17] is probably due to the small difference in composition of the two soda-lime glasses.

Another important factor for the purpose of space charge doping is that the conductivity of the glass due to Na^+ increases exponentially with the temperature, changing by several order of magnitudes from room temperature to the doping region highlighted in orange in Figure 3.2. As we can see the conductivity of Na ions is negligible at room temperature, but becomes appreciable in the doping region. In Figure 3.3 the exponential increase

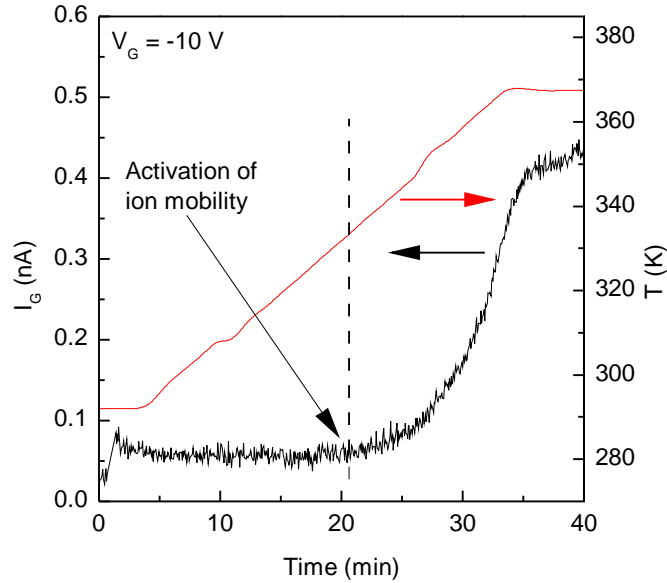


Figure 3.3: Variation of the current through soda-lime glass with a constant applied voltage of $V_G = -10$ V while temperature is swept from room temperature to ~ 370 K.

in the current through glass is shown when the temperature is varied from room temperature to ~ 370 K. The gate voltage is kept constant at -10 V. Further details about the doping region will be given later in this chapter.

Measurable ion mobility is activated above a certain temperature (~ 330 K). If an electric field is applied across the glass Na ions begin to drift and it is possible to create an accumulation of Na^+ at the interface between the glass and the cathode. At the same time, at the anode a depletion of Na^+ is induced leaving the non-bridging oxygen ions uncompensated. Thus, two space charge layers are created at the opposite faces of the glass with opposite polarity, perturbing the local electrical neutrality but still keeping the whole glass substrate electrically neutral. For a typical concentration of Na_2O of 10^{21} cm^{-3} an accumulation layer of 1 nm can create a charge imbalance on the surface of the order of 10^{14} cm^{-2} thanks to the image charge. This space charge can be generated with modest temperatures and voltages; the typical temperatures involved are between 330 K, where the ions mobility is activated, and 380 K, while the voltage can be varied between 1 and 300 V. On increasing temperature or voltage the space charge layer creation can be accelerated but care must be taken to avoid dielectric breakdown in the glass. In our case the upper limit for the voltage is technically imposed by the electronic instrumentation, but the need for higher voltage for the purpose of achieving a better doping performance has not been felt. Very rarely we have used higher temperature (up to 420 K) to perform doping on our samples, but this is a risky procedure because at this temperature applying the maximum allowed voltage can cause dielectric breakdown.

As long as the electric field is present at high temperature, the created space charge continues to increase until an equilibrium is reached, *i.e.* when the electric field of the space charge at the opposite faces of the glass compensates the external electric field. If the external voltage is turned off the Na ions tend to migrate towards the opposite face of the glass to restore the global electrical neutrality. However, if the system is cooled down fast with the voltage applied the ion mobility is rapidly suppressed and when the temperature is such that Na⁺ mobility is negligible the space charge is preserved “permanently” even if the external electric field is removed.

The electric field generated by the space charge can be thought of as the one across a dielectric in a Field Effect Transistor (FET) configuration, with the difference that in the case of space charge doping the space charge which corresponds to the charge on the gate electrode is confined very close to the surface which carries the sample. The associated capacitance is high compared to the FET thus inducing a higher image charge. A material deposited on the surface of the glass will feel the electric field of the space charge and it will thus be doped *n* in the case of Na⁺ accumulation at the interface or *p* in the case of depletion. This conceptually simple process turns out to be practically simple as well as an efficient doping method for materials deposited on the glass surface.

3.2 Space charge doping applied to graphene

There is considerable literature concerning the use of graphene as a transparent conducting electrode (TCE) [14, 96, 97]. In fact, graphene has been considered as a very promising material for this application thanks to its exceptional electronic transport properties (Section 1.3.1) and its transparency, being higher than 95% in the visible range of the light ($\sim 97\%$ at a wavelength of 550 nm). However, its resistivity is of the order of few $\text{k}\Omega/\square$ at low doping, too high to be used as a TCE. Doping is thus necessary to lower graphene sheet resistance. Several techniques have been used to dope graphene (see Section 1.3.5), but several drawbacks exist including limits on the maximum reachable carrier concentration, longer-term instability or transparency issues [23, 43, 45].

We applied the space charge doping for the first time to graphene in order to fully characterize our doping technique and in parallel investigate its applicability as a TCE. The study was performed on several graphene samples deposited on glass via polymer assisted transfer of CVD graphene or with the anodic bonding method. The experiments are carried out on microscopic samples (lateral size $l \approx 50 \mu\text{m}$), for limiting extrinsic effects and monitoring the sample area with micro-Raman spectroscopy before and after the doping, and macroscopic samples ($l \approx 1 \text{ cm}$) to validate the technique for large areas. The techniques used for the sample fabrication are described

in Chapter 2 and in the following the experimental details of the sample fabrication and characterization will be given.

3.2.1 Fabrication of the graphene samples

CVD graphene

CVD graphene we used in this study was purchased online (Graphene Supermarket, <https://graphene-supermarket.com/>). We intentionally used medium quality CVD graphene to perform our first experiments on space charge doping. The manufacturer declares that the 20 μm thick copper foil is entirely covered with a graphene layer on both sides with a small portion of bilayer islands (10 – 30%). The samples were deposited on glass (soda-lime or borosilicate) following the PMMA assisted transfer procedure described in Section 2.1.2. At the end of the process the glass surface is almost entirely covered by the graphene sheet having an effective area of the order of 1 cm^2 .

The surface of the graphene presents some impurities and little holes which arise from the transfer process, as shown in Figure 3.4. The impurities are residues of the PMMA used as mechanical support for the graphene during the transfer, while the holes can be attributed to mechanical stress during the whole process. The wrinkles which are slightly visible on the surface come from the quality of the CVD graphene we purchased. The

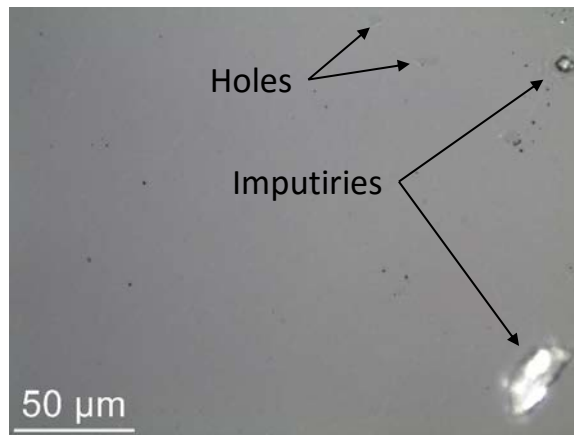


Figure 3.4: The surface of a CVD graphene sample transferred on glass. The image was taken with a 50X objective.

copper etching, the deposition of the graphene/PMMA stack and successive dry step and the first annealing have been carried out in a clean room environment.

The optical characterization of Figure 3.4 is always followed by a characterization with the μ -Raman spectroscopy, which gives detailed information about the quality of graphene through the D peak at $\sim 1350 \text{ cm}^{-1}$ (see Section 1.3.3). The absence of this peak indicates a good quality sample.

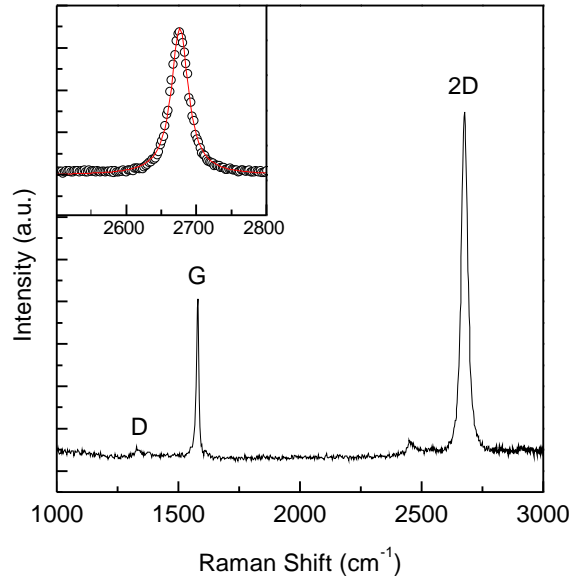


Figure 3.5: Typical Raman spectrum of a CVD graphene sample after the transfer process. The almost absent D peak suggest that the sample has a good quality. Inset: fit of the 2D peak with a single Lorentzian curve as a demonstration that the sample is a mono-layer graphene.

Figure 3.5 shows a representative Raman spectrum of CVD graphene measured just after the transfer process. The spectrum was acquired with a laser wavelength of 532 nm with a power of 3 mW, a grating of 1200 and an acquisition time of 8 seconds for 2 accumulations. The shape of the 2D peak clearly indicates that the sample is a mono-layer graphene [22] and we can see it very well from the inset in Figure 3.5 where the 2D peak has been fit with a single Lorentzian curve. Raman mapping have also been used to characterize relatively large areas of the sample surface and the results will be presented later in this chapter.

Anodic Bonded graphene

Graphene was also produced with the anodic bonding technique on soda-lime or borosilicate glass, as in the case of the CVD graphene. The detailed explanation of this method is given in Section 2.1.2. As in space charge doping, an electrostatic field is created on the glass surface but in this case the bulk precursor is electrostatically stuck to the surface of the glass by the O^{2-} space charge formed at the interface between the two. Adhesive tape is then used to remove the upper layers of the precursor leaving mono- to multilayer flakes of the sample on the glass surface. The parameters (temperature, voltage and time) for good bonding which also ensure a good yield depend on a number of factors: (i) the material which is being bonded to the glass, (ii) the glass type and (iii) if an anvil or a micromanipulator tip is used as the top electrode. Once the optimal range of parameters is found

for a given material, anodic bonding is an extremely efficient method for the production of high quality 2D samples.

During this thesis, more than 450 graphene samples have been fabricated with this method and the optimal parameters for each for each situation (borosilicate or soda-lime glass, anvil or tip) have been found. A typical sample presents several flakes of multi-layer graphene and it is possible to find few flakes of mono-layer graphene having a lateral size of $10 - 100 \mu\text{m}$. The optimal bonding parameters are listed in Table 3.1.

| | Anvil | | |
|--------------|-------------|--------------------------|----------|
| | V_G (V) | T ($^{\circ}\text{C}$) | t (min.) |
| Borosilicate | 1700 – 1800 | 250 – 230 | 10 – 20 |
| Soda-lime | 1250 | 225 | 15 |

| | Tip | | |
|--------------|-----------|--------------------------|----------|
| | V_G (V) | T ($^{\circ}\text{C}$) | t (min.) |
| Borosilicate | 1000 | 225 | 10 – 20 |
| Soda-lime | 400 – 600 | 225 | 1 – 15 |

Table 3.1: Optimal anodic bonding parameters for graphene.

Some things have to be pointed out: the parameters for sticking graphene to soda-lime are always lower than the borosilicate glass, as a consequence of the higher Na^+ concentration in the soda-lime substrate ($3.4 \times 10^{18} \text{ cm}^{-3}$ against $1.4 \times 10^{18} \text{ cm}^{-3}$); the same thing is valid if the tip is used instead of the anvil because the tip concentrates the applied electric field more efficiently on the sample area, making the bonding process more efficient; the bonding time varies between 1 and 20 minutes, but usually it has been found that 15 minutes is a good period of time for getting a good yield.

The samples are characterized with the techniques described in Chapter 2. First, the identification of the monolayer samples is done with the optical microscope. The contrast of graphene on glass is low [98], but with some experience it is easy to identify monolayer samples. In Figure 3.6 a big monolayer graphene sample deposited on soda-lime glass with the anodic bonding method is shown ($T = 225^{\circ}\text{C}$, $V = -1250 \text{ V}$, $t = 15$ minutes). The dimensions of the sample with lateral size in excess of 200 micrometers are large compared to what can be obtained with the mechanical exfoliation



Figure 3.6: Optical image of a monolayer graphene sample on soda-lime glass (highlighted with the red line). The lateral size in one direction exceeds $200\ \mu\text{m}$.

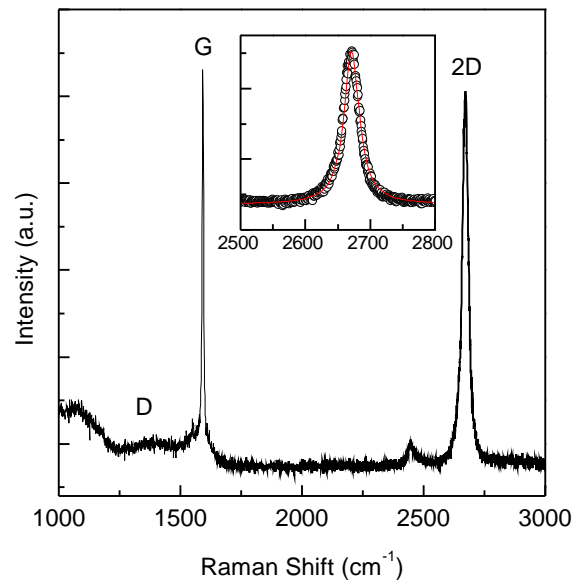


Figure 3.7: Raman spectrum of a typical anodic bonded graphene sample on glass. Again, the shape of the 2D peak (in the inset) confirms its monolayer nature and the absence of the D peak is a sign of high quality. The intensity of the 2D peak is lower than expected, compared to the G peak. This is a consequence of the doping induced by the space charge in the glass for sticking the precursor.

method. This fact, combined with the good quality and the possibility to follow up with space charge doping means that anodic bonding is the preferred method for fabricating 2D samples in our group. Raman spectroscopy

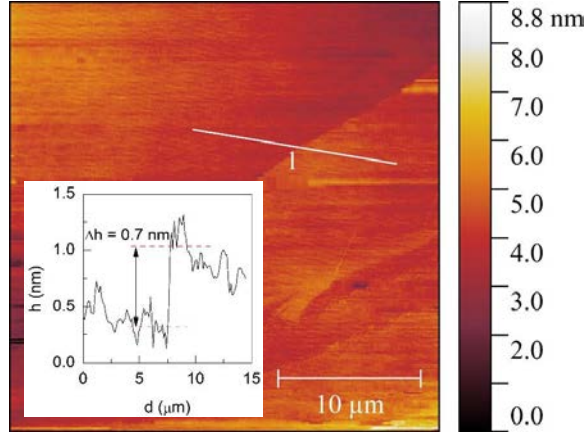


Figure 3.8: AFM scan of the edge of an anodic bonded monolayer graphene sample. The measured height of ~ 0.7 nm (in the inset) is compatible with the predicted thickness of graphene.

is then used to check the quality of the sample and verify its thickness, as showed in Figure 3.7. It is possible to note that the D peak is totally absent from this spectrum confirming that the sample is of excellent quality. However, it is known that in monolayer graphene the ratio of the intensities of the 2D over the G peaks should be around 2 or 3 [22] and this fact can be misleading in the identification of a monolayer. In the case of anodic bonded graphene it is found that the 2D/G ratio is close to unity and this is due to the fact that the graphene sheet is doped [23], as a consequence of the anodic bonding process. In undoped graphene, with the Fermi level lying at the meeting point of the valence band (VB) and conduction band (CB), an incident photon can excite an electron from the VB to the CB at any value of the \mathbf{k} vector. The 2D peak in the Raman spectrum results from a double resonance process involving two near-K point phonons (see Section 1.3.3). When the Fermi level is shifted upwards (n -doping) or downwards (p -doping) the number of possible vertical transitions in the momentum space is reduced with respect to the undoped case, thus the number of double resonance phenomena is decreased resulting in a lower 2D peak intensity [23].

Finally, AFM is used to further confirm that the sample is a monolayer. A typical AFM topography is shown in Figure 3.8, where the edge of a graphene sample is scanned in order to measure its thickness. This is a further confirmation that the sample is just one atom thick, besides the fact that it is free from surface impurities (as opposed to the CVD graphene).

Contact deposition and shaping

As described in Section 2.3.2, the contact deposition is done through a stencil mask which is carefully aligned to the desired area of the sample with the help of micromanipulators and fixed with adhesive tape. Then, gold contacts 75 – 100 nm thick are deposited by thermal evaporation.

Figure 3.9 shows an example of contact deposition on a microscopic anodic bonded sample of lateral dimension of $\sim 50 \mu\text{m}$. The smaller the

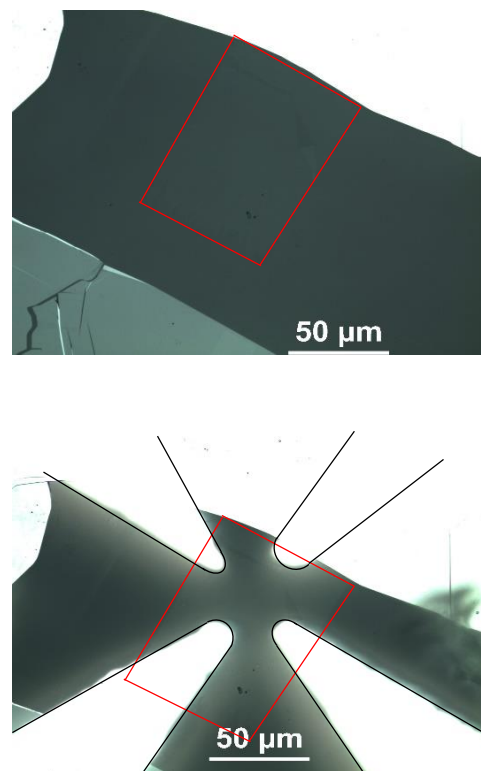


Figure 3.9: Contact deposition on an anodic bonded graphene sample with a lateral size of $\sim 50 \mu\text{m}$. The sample is highlighted in red, the gold contacts with a black line.

sample the more the alignment needs to be precise. The next step is to mechanically remove short circuits and give the sample the proper shape, compatible with the van der Pauw method. The samples are shaped by scratching the surface with a micromanipulator tip in order to remove the unwanted parts or with plasma etching as described in Section 2.3.2. A CVD graphene shaped with plasma etching is shown in Figure 3.10. The etched area leaves a square of graphene at the center of the glass. Even if the contacts are several hundreds of microns away from the square corners, the effective area which will be measured with the van der Pauw method is only the one delimited by the square itself [90].

Compared to the scratching with the micromanipulator tip, the shaping

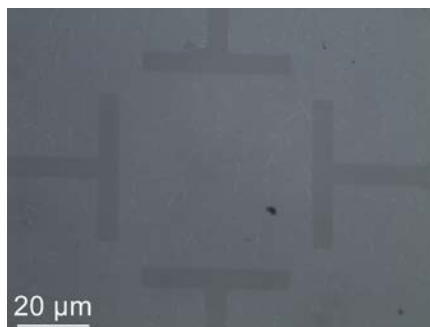


Figure 3.10: Result of the plasma etching on a macroscopic CVD graphene sample after a step of electron beam lithography. The etched part appears slightly darker whit respect to the graphene covered glass. The effective area of the sample which is measured is the area enclosed in the square.

with the plasma etching is more precise but it requires several technological steps to be performed. Moreover, it leaves residues of the polymer on the sample surface which can alter its quality and electronic transport properties.

3.2.2 Results

Space charge doping is performed in high vacuum ($p \leq 10^{-6}$ mbar) in our transport measurement setup (Section 2.4). Vacuum is important in order to not contaminate the graphene surface during the doping which, as it is a charged surface, would otherwise attract charged impurities from the air. We applied our doping technique to several graphene samples in order to characterize several aspects: the maximum achievable carrier concentration, the control we can have on the carrier density, the effects of different glasses on the maximum induced carrier concentration and transport properties, the effects of the space charge doping on the sample quality. All these aspects will be discussed in the following.

Ambipolar doping

The sample deposited on the glass surface can be thought as an electrode which is put to the ground potential. When the glass is hot, the voltage on the electrode on the opposite face of the glass determines the direction of the Na^+ ions drift. There will be accumulation of Na^+ close to the sample if $V_G > 0$, depletion of Na^+ if $V_G < 0$. This is schematized in Figure 3.11.

Before space charge doping, the sample usually has some intrinsic doping due to charged impurities on the surface caused by air exposition and/or by the CVD transfer process. For samples made by the anodic bonding process, there may be a residual space charge effect. The impurity induced doping can be as high as $\approx 10^{13} \text{ cm}^{-2}$ [34] and it is usually found to be hole doping.

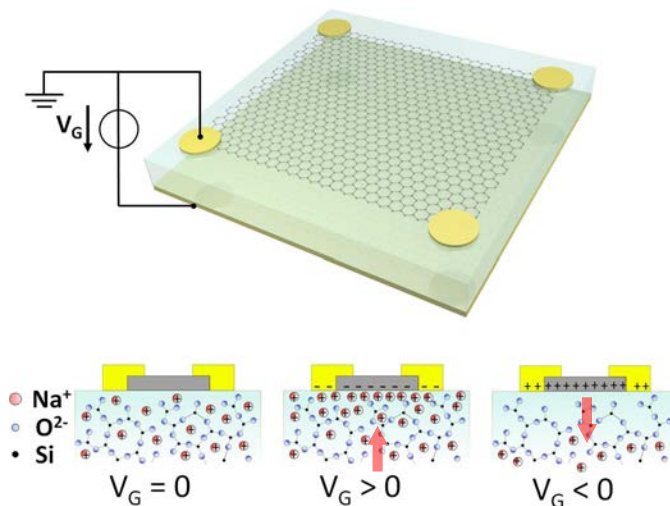


Figure 3.11: Illustration of the principle of space charge doping applied to a graphene sample. With no applied gate voltage the equilibrium in the glass is preserved but when the glass is hot (*i.e.* Na^+ mobility is activated) the polarity of V_G determines accumulation ($V_G > 0$) or depletion ($V_G < 0$) of sodium ions at the interface.

Annealing performed in vacuum (at a pressure $\leq 10^{-6}$ mbar) in the cryostat at a temperature of 420 K or in an external oven (always in high vacuum) at $T = 525$ K can significantly reduce this doping and even eventually reverse it (from hole to electron for example).

We experimented two slightly different doping procedures: the first consists in heating the sample to the doping temperature and then increasing the gate voltage to a desired value and waiting for the doping to be accomplished; in the second approach, the gate voltage is applied at room temperature and then the sample is heated to the desired temperature. We found the second method to be more efficient in terms of maximum doping reached.

We will now show some representative results obtained on a graphene sample realized with the anodic bonding technique. The substrate is soda-lime glass and the bonding process was done using the anvil as top electrode. The parameters for the deposition of the sample are $T = 225^\circ\text{C}$, $V = -1250$ V and $t = 15$ minutes. Figures 3.12 and 3.13 shows two different doping procedures performed on this sample. As we can see, several parameters can be monitored and controlled during the doping, like the sheet resistance R_S , the gate voltage, the gate current and the temperature. An annealing was performed for an overnight period in the cryostat at a temperature of 420 K. The carrier density measured after the annealing at room temperature with the Hall effect was $4.02 \times 10^{12} \text{ cm}^{-2}$ and $R_S = 1180 \Omega/\square$. Vacuum annealing is expected to remove impurities from

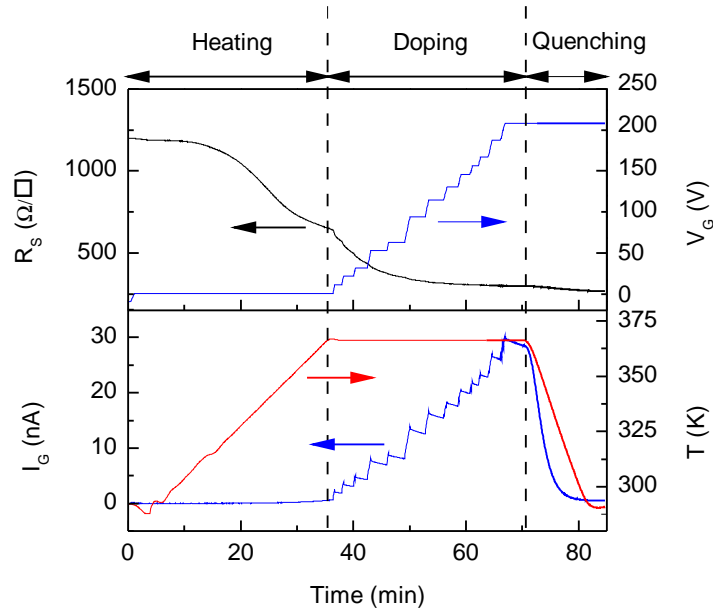


Figure 3.12: Doping of an anodic bonded graphene with a positive gate voltage. The sample was found to be slightly n -doped after a vacuum annealing in the cryostat. It was then heated to the doping temperature and the voltage increased up to 210 V.

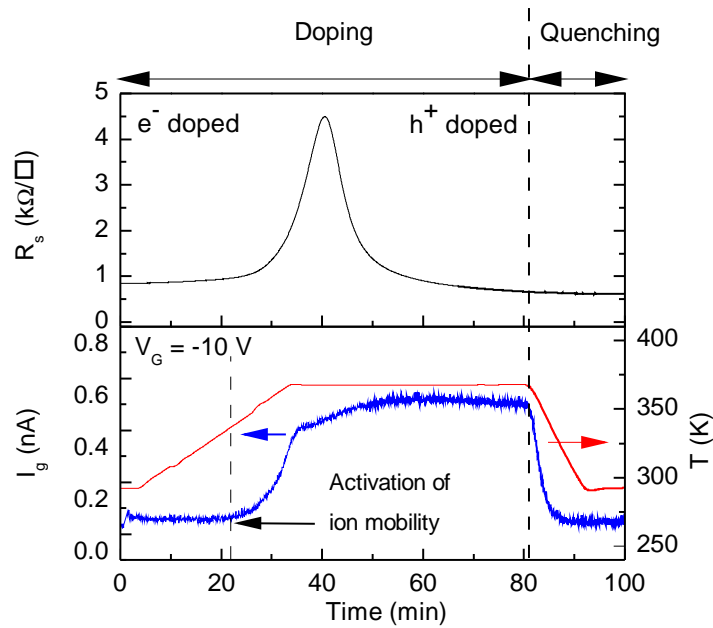


Figure 3.13: The same sample of Figure 3.12 is p -doped by applying $V_G = -10$ V at room temperature and then heated to 370 K. The space charge is progressively formed by uncompensated O^{2-} ions as Na^+ ions drift away from the interface and the sample is p -doped.

the surface of graphene and also neutralize the space charge created with the anodic bonding fabrication process in the glass substrate.

As we can see from Figure 3.12 the sample is heated to 365 K with a constant applied voltage $V_G = 10$ V. We see a decrease in R_S with the temperature indicating that the sample is being electrostatically doped due to the accumulation of sodium ions at the interface. Once the 365 K value is attained, the gate voltage is progressively increased to +210 V. R_S immediately decreases due to the increasing space charge at the interface. When R_S does not change anymore the process can be stopped. The sample is then cooled down rapidly ('quenched') to room temperature where the ion mobility is negligible. The space charge is then 'frozen' and conserved even with $V_G = 0$ V (not shown in the figure). The electron concentration measured at room temperature is 10^{14} cm⁻², an extremely high value compared to the usual carrier concentrations attained with conventional electrostatic techniques in graphene and also with respect to some chemical approaches. The corresponding sheet resistance due to residual resistance from defects or impurities is 270 Ω/\square at room temperature.

We now focus on Figure 3.13 where the doped sample of Figure 3.12 is first annealed for an overnight period at 420 K with no V_G to neutralize the previous doping and "reset" the glass. The same effect could also have been achieved by inverting the polarity of the gate voltage at high temperature. The starting conditions are $R_S = 850$ Ω/\square and the electron concentration is 8.82×10^{12} cm⁻², meaning that there is still a residual space charge at the glass/material interface (a longer annealing would have still reduced this space charge). This time we apply a constant gate voltage of -10 V corresponding to hole doping. In the bottom part of Figure 3.13 it can be seen that the gate current increases exponentially as the temperature increases as a consequence of the ion mobility and drift. As a result the graphene layer is progressively hole doped. The Na⁺ accumulation is progressively reduced finally leaving a negative oxygen ion space charge (figure 3.11) and resulting in the typical bell-shaped curve in the top part of Figure 3.13 as the Fermi level in graphene is progressively shifted from the conduction band, through the neutrality point to the valence band. Figure 3.14 shows the Hall measurements performed before and after the doping process. The sign of the slope of the Hall resistance curve with respect to the applied magnetic field indicates that the charge carriers in the sample are changed from electrons to holes, the final carrier concentration being 10^{13} cm⁻².

Fine doping and doping limit

Following the procedure illustrated in Figure 3.12 or 3.13 it is possible to reproduce the well known bell-shaped R_S vs n_S characteristic of graphene (see Section 1.3.1), as depicted in Figure 3.15. Each point of the curve has been reproduced after a doping step and a Hall measurement (shown all

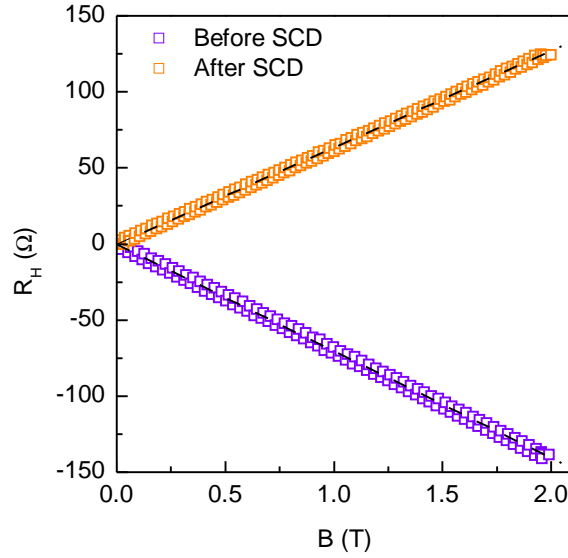


Figure 3.14: Hall measurement performed before and after space charge doping showing that the charge carrier type in the graphene sample is changed.

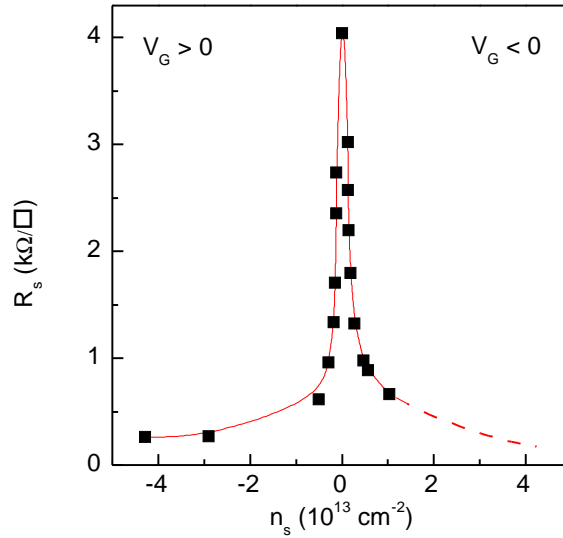


Figure 3.15: A large CVD graphene sample on a borosilicate glass substrate doped at different carrier concentrations. Each point of the curve is obtained with the process described in Figure 3.12 or 3.13. The red line is a guide for the eyes.

together in Figure 3.16 in the 0 – 2 T range). It is clear that the carrier density can be finely controlled by the space charge at the interface.

We found experimentally that in the case of graphene the maximum reachable carrier density is higher for electrons than for holes. This could be related to the technique itself and space charge creation in the glass. Indeed the n -doping process is due to Na^+ accumulation at the interface

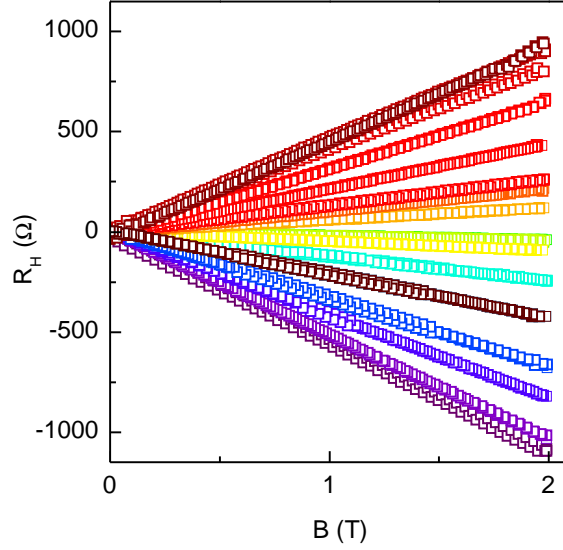


Figure 3.16: The Hall measurements done in each point of the curve of Figure 3.15 from 0 to 2 T showing the wide range of achievable doping.

while p -doping is due to Na^+ depletion and therefore due to the uncompensated and non-mobile oxygen ions. The width of the space charge could thus be different, being smaller in the case of ion accumulation and therefore the capacitance associated to the space charge could also be different. Like in a FET device, the higher the capacitance the higher the charge accumulation at the interface. This would then be a direct consequence of the fact that Na^+ ions are mobile while O^{2-} ions are covalently bound to the atomic structure of the glass. This observation needs direct confirmation though and eventually also needs to be correlated with the material to be doped. The highest achievable carrier density is determined by another parameter: the Na^+ content in the glass. Higher Na^+ content in glass implies a more dense space charge at the interface and thus a higher electric field. In table 3.2 we compare the maximum electronic carrier concentrations achieved borosilicate and soda-lime glass substrates on graphene. A carrier density three times higher is achieved with soda-lime glass. At the highest carrier density attained the shift of the Fermi energy from the Dirac point is calculated through the expression $\Delta E_F = \hbar |v_F| \sqrt{\pi n_S}$ [99], with $v_F \approx 10^8$ cm/s being the Fermi velocity and \hbar the reduced Planck constant. With $n_S = 10^{14} \text{cm}^{-2}$ we obtain $\Delta E_F = 1.17$ eV.

| | Na ⁺ density (mm ⁻³) | Max carrier density (cm ⁻²) |
|--------------|---|---|
| Borosilicate | 1.4×10^{18} | 4×10^{13} |
| Soda-lime | 3.4×10^{18} | 1.2×10^{14} |

Table 3.2: Maximum reached carrier concentration in graphene.

The limiting value for doping limit is not always due to the Na⁺ concentration in the glass and it is sometimes necessary to stop the doping process in order to avoid damage to the sample. When the space charge appears and the sample begins to be doped, a strong attraction arises between the sample and the glass surface because they have opposite charges. The electrostatic pressure on the sample can reach 1 MPa [16, 79], possibly inducing deformation. This would degrade its quality and the mobility of the charge carriers in the material as shown schematically in Figure 3.17. Well polished substrates and finely prepared surfaces are thus a key to avoid this degradation. We have probed this aspect by pushing the doping process beyond

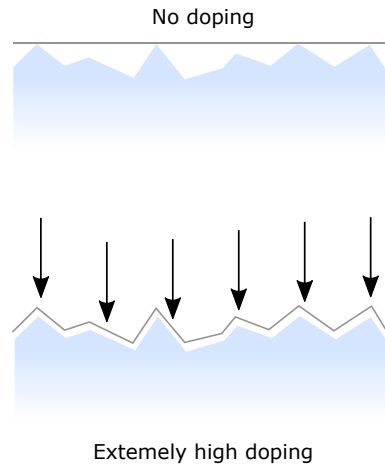


Figure 3.17: Illustration of the mechanical stress to which graphene is subjected in extremely high doping conditions.

the value for which R_S no longer decreases. In these conditions we observe that R_S , after attaining a minimum value, starts to increase meaning that the mobility of the charge carriers decreases possibly because of sample deformation. An example is shown in Figure 3.18, where a CVD graphene sample on a soda-lime glass substrate is doped at 375 K at a gate voltage of 130 V. As highlighted in orange in the figure, the resistance attains a mini-

mum and then starts to increase. At this point, quenching the temperature is necessary in order limit damage in the sample. The carrier concentration that was measured later at room temperature for this particular sample was $1.2 \times 10^{14} \text{ cm}^{-2}$.

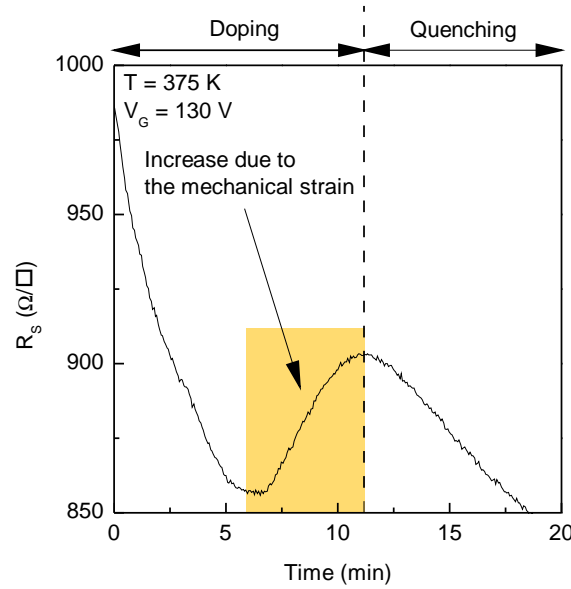


Figure 3.18: Mechanical strain induced increase of sheet resistance at very high doping values.

Reversibility

Outside of conditions leading to sample damage, space charge doping ensures perfect reversibility of the doping process. It is thus always possible to achieve a carrier concentration previously induced in the sample by simply performing space charge doping and quenching the system at the proper value of R_S . This fact is presented in Figure 3.19, where a $70 \times 70 \mu\text{m}^2$ CVD graphene sample is doped at different carrier concentration values going in the n to p direction (black circles) and then is doped back from the p to n direction (red crosses) by stopping the doping process at the same R_S value found before. Clearly, the same carrier concentration is found for all the points, meaning that the process is fully reversible. A detailed analysis of the graphene quality after the doping process will be done later in this chapter.

Substrate surface quality

We showed above that the substrate surface quality can induce mechanical deformation in the sample at high doping. We now take a closer look at the influence of this substrate surface quality on the sample mobility. As

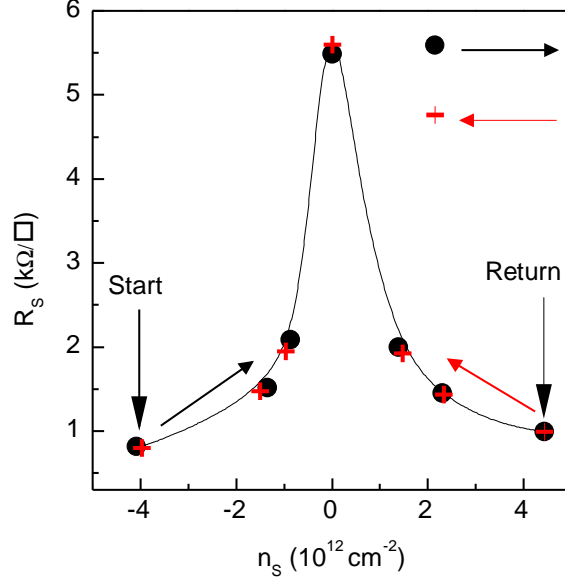


Figure 3.19: Space charge doping is performed on a $70 \times 70 \mu\text{m}^2$ CVD graphene sample (delimited with a micromanipulator tip) in a cycle to demonstrate the reversibility of the doping process. The black circles represent the doping performed in the n to p direction while the red crosses are the doping in the p to n direction.

reported in Table 3.2, soda-lime glass allows to reach carrier concentration levels exceeding 10^{14} cm^{-2} thanks to the higher sodium ion content. But for a transparent conducting electrode application the carrier concentration is not the only factor which is relevant. The sheet resistance of the TCE should be below a certain threshold value which depends on the application. For the most demanding applications the threshold of $\sim 100 \Omega/\square$ [100] is often cited. The Drude resistivity in a material depends both on the carrier concentration and the mobility of the charge carriers.

$$R_S = \frac{1}{e\mu n_S} \quad (3.1)$$

where e is the electron charge, n_S is the carrier density in the material and μ is the mobility. Mobility is affected in particular by defects or deformations. In a one atom thick material like graphene the interaction with the substrate can play a role in modifying electronic properties. In order to quantify this aspect we compared the results of the measured Hall mobility taken from several samples and for different carrier densities (both in the n and p side) deposited on borosilicate or soda-lime glass. They are reported in Figure 3.20. Both in the electron and the hole side we observe a reduction on the mobility with increasing carrier concentration, which is normal because the charge carriers experience an incremented carrier-carrier scattering, which

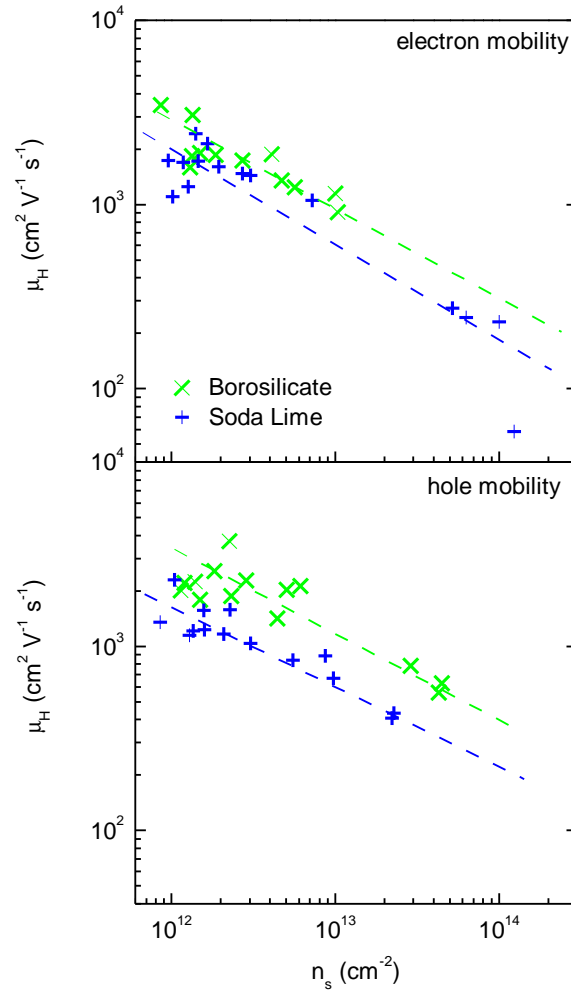


Figure 3.20: Hall mobility of several graphene samples deposited on the two glass substrates used in this thesis at different carrier concentration values.

lowers the mobility. However, the mobility of the samples deposited on the borosilicate glass is systematically higher than the mobility of the samples on soda-lime at every carrier density value. AFM scans of the surfaces of the borosilicate and soda-lime glasses revealed that the root-mean-square (RMS) roughness is significantly lower in the borosilicate glass than in the soda-lime (0.227 nm against 0.734 nm) as Figure 3.21 shows. The difference is due to the polishing procedure carried out by the manufacturer, since no polishing step was performed by us. This difference in the RMS roughness (see Figure 3.17) explains why graphene doped on borosilicate glass reached a minimum R_S comparable with the minimum R_S on soda-lime glass notwithstanding the lower n_S values obtained in the former. The minimum value of sheet resistance measured at room temperature after the doping were $224 \Omega/\square$

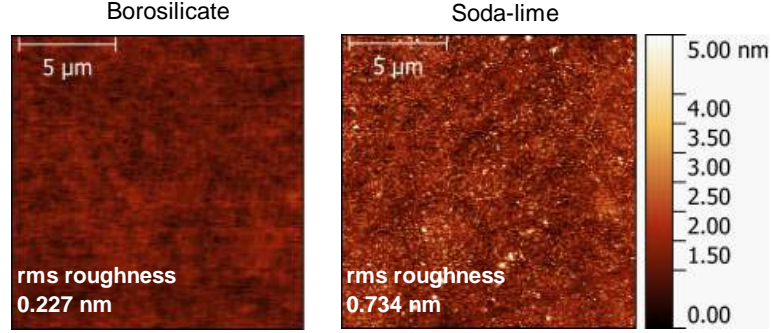


Figure 3.21: AFM topography performed on the surface of clean borosilicate (left) and soda-lime (right) glass. The flatter nature of the borosilicate glass substrate is visible from the topography. The scan is performed on an area of $15 \mu\text{m} \times 15 \mu\text{m}$ and RMS roughness of 0.227 nm for borosilicate and 0.734 nm for soda-lime extracted by software analysis.

for CVD graphene on borosilicate glass and $268 \Omega/\square$ for anodic bonded graphene on soda-lime glass.

Transmittance

For transparent conducting electrodes (TCE) the transparency of the material is a fundamental aspect. TCE are used in many devices like solar cells, diodes or displays and are essential for the proper functioning of the device: they provide electricity to the active part of the device and at the same time let the light go in or out of it. The problem in producing such materials is that the transparency of a material decreases with increasing conductivity. The transparency is measured through the transmittance. The transmittance is defined as the portion of light at a certain wavelength which is not absorbed by a material and passes through it. The transmittance spectrum of doped graphene was measured by illuminating the graphene layer through the substrate using a white lamp in several points and analyzing the transmitted spectrum with the spectrometer of our Raman system. The same thing is done on clean glass adjacent to the graphene sample. The ratio between the two intensities at every wavelength gives the transmittance spectrum of doped graphene:

$$T(\lambda) = \frac{I_{\text{graphene}}(\lambda)}{I_{\text{glass}}(\lambda)} \times 100 \quad (3.2)$$

where $I_{\text{graphene}}(\lambda)$ is the intensity of light passing through graphene and the space charge above it and $I_{\text{glass}}(\lambda)$ is the intensity of light passing through the clean glass close to the graphene sheet. The range of wavelengths in which the measurement is done is 535 – 800 nm (the lower limit is imposed by the filter in our Raman system, the upper limit is the limit of the visible range).

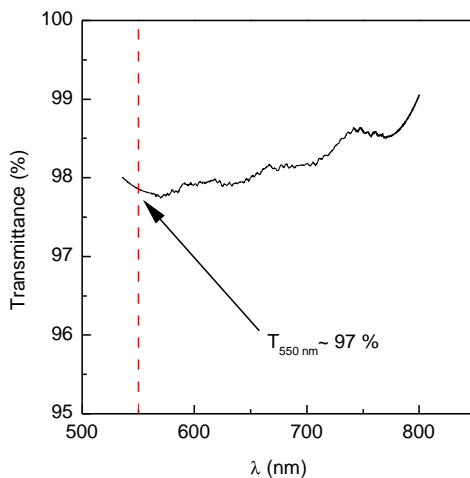


Figure 3.22: Transmittance of a doped CVD graphene sample in the wavelength range between 535 and 800 nm.

Monolayer graphene has a transmittance of $\sim 97.6\%$ at a wavelength of 550 nm [81]. In Figure 3.22 are shown our measurements on doped CVD graphene performed immediately after high doping. As we can see, the transmittance is not altered by the doping process.

Quality of the doped samples

The graphene samples like the one showed in Figure 3.10 were used to monitor a given area with μ -Raman mapping before and after the doping process. As described in Section 1.3.3, the Raman signal of graphene gives useful information about its quality [22] through the D peak and about carrier concentration [23] through the ratio of the intensity of the 2D peak to the G peak. Raman mapping allows to monitor both aspects simultaneously over a big area. The step size we used for the mapping was $1.3 \mu\text{m}$ over an area of $30 \times 30 \mu\text{m}^2$. The ratio 2D/G was mapped (Figure 3.23) before and after the doping in the same area. The sample was routinely doped both in the electron and in the hole side, the last value of carrier concentration before Raman mapping being $4.28 \times 10^{13} \text{ cm}^{-2}$ on the electron side and $R_S = 260 \Omega/\square$. It is clear that the 2D/G ratio decreases remarkably after the doping and in a uniform way on the whole area of the sample. This is consistent with the results found in [23] and [35] where the effects of doping was monitored with μ -Raman measured *in situ*. The spectra collected during the mapping are also used to monitor the quality of the graphene layer before and after the doping. In Figure 3.24 10 representative spectra extracted from the Raman mappings are shown. The curves are shifted for clarity. We note that there is no increase in the D peak, confirming that the graphene layer has not been damaged by the multiple doping steps. It can

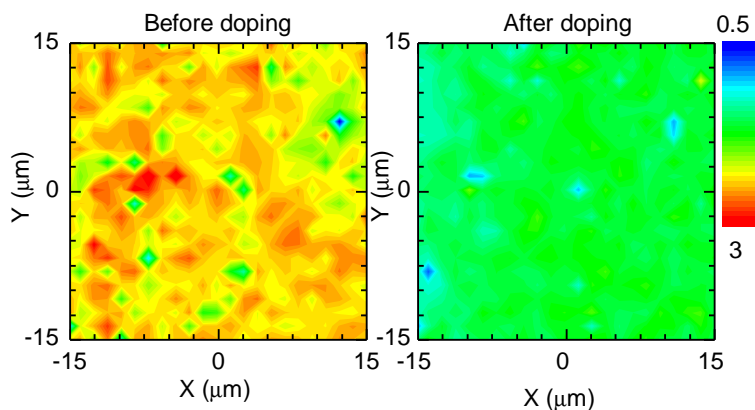


Figure 3.23: Map of the 2D/G ratio measured before and after the doping showing a remarkable and uniform decrease as indication of the homogeneity of the doping all over the sample area.

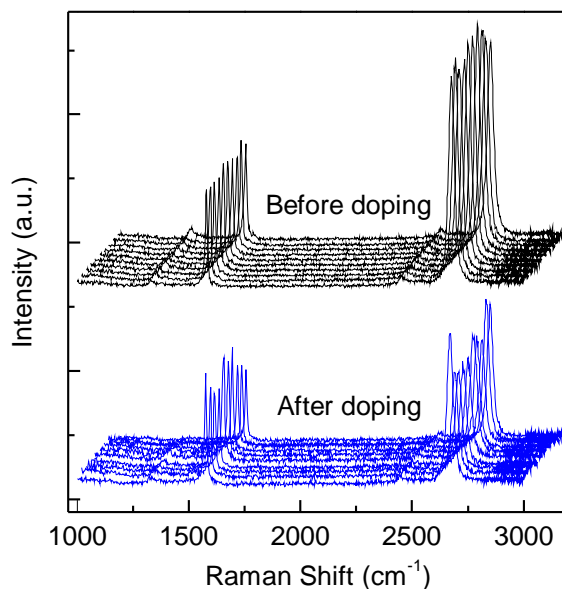


Figure 3.24: Raman spectra of undoped and doped graphene extracted randomly from the Raman mapping. The insignificant D peak demonstrates that no defects are introduced during the doping process.

again be seen that the ratio of the intensity of the 2D over the G peak is significantly reduced after the doping.

3.3 Comparison with other doping methods

Published literature furnishes a wide variety of methods to dope graphene. The first ever used is the electrostatic doping through a dielectric in a field effect transistor (FET) configuration using an exfoliated graphene sample

deposited on an SiO₂/Si [2] substrate which is also used as gate electrode. The advantage of using this technique is that it is relatively straightforward to implement and it allows to change the carrier concentration in the sample simply by changing the gate voltage. On the other hand, the maximum achievable carrier concentration is relatively low for certain applications, being of the order of 10¹² cm⁻². This is due to the low capacitance associated with the SiO₂ dielectric and also the thickness of the oxide layer routinely achievable. Moreover, a graphene sample in this configuration can obviously not be used as a TCE because of the non transparency of the SiO₂/Si substrate and the gate voltage needs to be maintained to maintain doping.

Other techniques involving chemical doping of the graphene sheet have been proposed. One of these which is also promising for the large scale production of graphene was presented in Reference [14]. Here, a roll-to-roll method was used to transfer large area CVD graphene onto a PET substrate and graphene sheets with diagonal dimension up to almost 80 cm have been repetitively transferred. During the transfer process the graphene layer is doped with nitric acid (HNO₃) and the authors found it to efficiently *p*-dope the graphene layer. Sheet resistivity as low as 125 Ω/□ on mono-layer graphene were obtained with a slightly altered transmittance. For TCE applications the advantages offered by this method are many (the minimum value of R_S, the transmittance of doped graphene, the applicability to very large areas) but on the other hand, this kind of doping is not stable in time thus imposing severe limitations to this technique [43]. Another example of chemical doping can be found in Reference [43], where the authors used a graphene layer *p*-doped with AuCl₃ as TCE for solar cells applications but they found that the process is not always reproducible. The two methods mentioned above have also the disadvantage of not being reversible.

Substitutional doping has also been used to dope graphene. In particular, in Reference [49] the electron and hole doping capability of substitutional boron (acceptor) or nitrogen (donor) in graphene are explored. The amount of B or N determines the amount of doping and it is thus possible to tune the carrier concentration in the sample. This interesting technique has the obvious disadvantage of not being reversible and the graphene structure is damaged because the substitutional atoms break the perfect hexagonal network of graphene, as seen by Raman spectroscopy. In another work in our group [48] nitrogen doping of graphene was performed during the growth of graphene onto a SiC substrate. It was found that the nitrogen induced carrier density can be as high as 2.6 × 10¹³ cm⁻², higher than the aforementioned electrostatic doping but the process is still irreversible, introduces defects and in the case of SiC graphene, remain incompatible with TCE applications.

Highest efficiency, in terms of maximum doping achievable, can be obtained by means of a polymer electrolyte gate as presented in Reference [23]. Here the principle is to use a polymer containing mobile ions in order

to create an ion accumulation at the interface with graphene (similarly to the space charge doping). The associated electric field dopes the graphene layer. With this method a charge carrier concentration of $5 \times 10^{13} \text{ cm}^{-2}$ can be obtained, but the graphene layer is contaminated by the polymer, an aspect that can significantly alter the electronic transport properties of graphene. Moreover, its transparency is greatly diminished by the presence of the polymer. Another example can be found in Reference [101], where the same method is used to dope CVD graphene. Liquid electrolyte has also been used to highly dope graphene and control the Raman scattering properties of the sample through doping, like is shown in Reference [35]. Again, there is no practical use of this technique due to the presence of the liquid electrolyte which can significantly alter the transport properties of graphene as well its transparency.

Space charge doping can overcome many of the disadvantages which characterize the doping techniques mentioned above. The substrate used is commercial glass, which is perfectly compatible with all applications especially those needing a transparent substrate like transparent conductive electrodes. It allows to reach a considerably higher carrier concentration than all the techniques known for doping graphene ($> 10^{14} \text{ cm}^{-2}$). Space charge doping does not involve the use of any extra layer or other technological steps. This ensures no contamination or unwanted doping of the sample and the preservation of its optical properties. Moreover, no defects are introduced during the standard doping process, which is really important to maintain unaltered the electronic properties of the sample. Especially for large scale applications, the uniformity of the doping is important to ensure the correct functioning of the device. During our experiments we dedicated particular attention to this aspect. We uniformly doped samples of 1 cm^2 maximum size, but conceptually the technique applies to samples of arbitrary size provided that the applied electric field necessary for the ion drift is uniform all over the sample area. Finally, the carrier concentration in the sample can be finely controlled. Moreover at room temperature or lower the doping is permanent without the need to maintain a gate voltage which is a very important criterion for energy saving. On the other hand, some drawbacks can be identified. First of all, tuning the carrier concentration in the sample requires heating the sample, achieving the required doping through ion drift and cooling down the system. These steps could be inconvenient in some applications. Also, if the sample is heated above the temperature where ion mobility is activate and the gate voltage is not applied the space charge will gradually disappear and the doping will be lost. This also can be not convenient for some applications like solar cells for example, but choosing or designing glasses with a higher activation temperature can overcome this problem.

If we consider space charge doped graphene as a TCE many of the problems mentioned above for other doping techniques can be overcome, but

others remain. Doped graphene is sensitive to ambient contamination because, being a charged material, it attracts charged impurities from the air which neutralize the doping induced by the space charge. For potential TCE use the graphene layer needs to be protected which is also a mechanical requirement. In this thesis, the standard value for TCEs of $100 \Omega/\square$ could not be achieved. As mentioned before this problem can be overcome by using more polished glasses and higher quality graphene. In the field of TCE space charge doping is thus an innovative method to increase the conductivity of transparent materials. One can for example investigate materials more mechanically robust than graphene. The answer could be found in transparent oxides. They are usually very resistive and, like in the case of graphene, many techniques have been used to lower the resistivity. As described in Chapter 4, we applied the space charge doping to zinc oxide and we will show it to be a valid alternative to what is commonly done to dope this material.

3.4 Control measurement on quartz

We made a cross-check to verify the microscopic mechanism that we use to justify the doping process. For this we used a substrate with similar dielectric properties and size as the glass substrate used, except that it contains no alkali ions. We performed a test measurement on a CVD graphene sample deposited on a quartz substrate. Quartz is formed by a crystalline network of SiO_2 and we can think about it as a glass without Na^+ ions or other foreign species. For our control measurement we used a quartz substrate of same thickness (0.5 mm) as our soda-lime and borosilicate glass substrates and of similar RMS roughness. In Figure 3.25 we compare doping performed on a CVD graphene sample deposited on borosilicate glass and a measurement of a CVD graphene on quartz. The two samples were subjected to a procedure which consists of

- (a) raising the temperature to 350 K and then applying a gate voltage of +210 V (red line),
- (b) leaving the system at that temperature for a fixed time (black line),
- (c) then decreasing to room temperature followed by switching off of the gate voltage (blue line).

The initial R_S of the samples depends on the impurities due to the transfer process of the CVD graphene from the copper substrate to the glass or quartz substrate. The bottom part of the graph corresponds to the doping procedure applied to the sample on glass. We can see that as soon as the gate voltage is applied a drop in the resistivity is observed, as a consequence of the electrostatic doping induced by ion drift. After a certain time and a

lowering of R_S of nearly $1 \text{ k}\Omega/\square$ the system is quenched to room temperature in order to freeze the ion space charge.

The top part of Figure 3.25 shows the same procedure applied to the graphene sample deposited on quartz. After the application of the gate

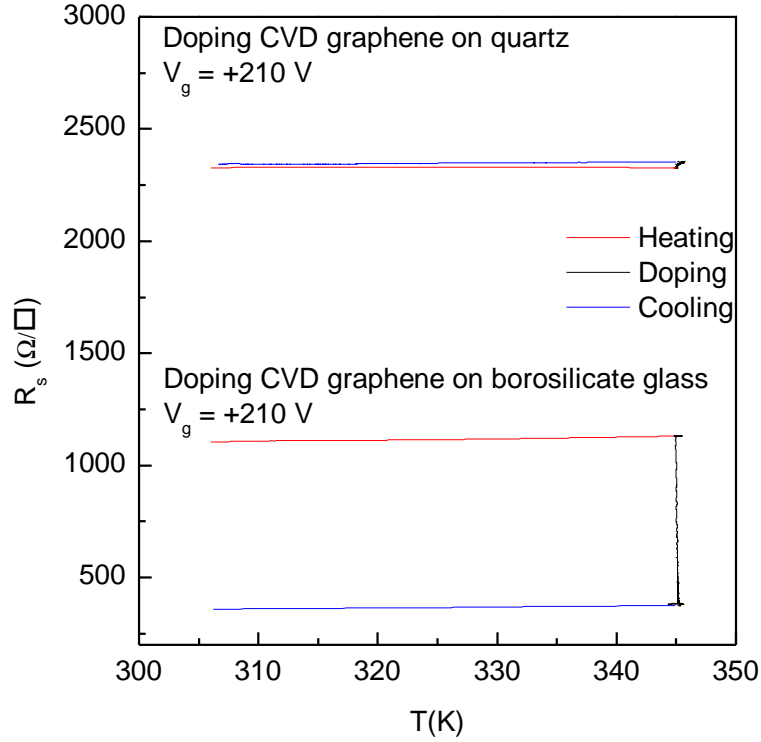


Figure 3.25: Space charge doping performed on CVD graphene on borosilicate glass compared to the doping attempted on CVD on quartz in the same conditions. We see that no effect is produced on the sample deposited on quartz due to the absence of sodium ions in the quartz.

voltage, only a small shift of the sheet resistance of $\sim 20 \text{ }\Omega/\square$ is observed due to the standard field effect across the quartz substrate. The R_S of the graphene layer remains unaltered after quenching the system to room temperature, giving a direct confirmation of the fact that the doping of the sample deposited on glass is due to the space charge formed by Na^+ ion accumulation or depletion. Since no ions are present in the quartz substrate, no space charge can be formed and the sample can not be doped with space charge doping method.

3.5 Conclusions on space charge doping

In this chapter we have introduced *space charge doping*, a technique for doping ultra-thin layers of materials deposited on a glass substrate. The first material to be doped with this technique is graphene. The choice of

graphene is justified by many factors, like the possibility to dope it *n* or *p*, the availability of big area or good quality samples and the ample bibliography present in literature on this material, useful to analyse our results.

The process of sodium ion drift (the key element of space charge doping) is exploited in order to form a space charge at the interface between the glass and the graphene deposited on its surface. Ion mobility is activated above 330 K and an electric field across the glass causes the Na^+ ions to migrate towards the cathode. The space charge layer can be formed either by Na^+ ion accumulation or depletion which creates a positive or negative electric field, respectively. The graphene sheet will accordingly be doped *n* or *p*.

Space charge doping was characterized in terms of maximum achievable carrier concentration, how finely the doping can be controlled, the effect of the doping process on the sample quality and the dependence of the space charge doping efficiency on the glass substrate. It turns out that, as expected, the maximum reachable carrier concentration in the sample can be obtained with glass substrates which have a higher ion concentration, but the minimum value of sheet resistance is strongly affected by the glass surface quality (an important aspect for transparent conducting electrode applications). Moreover, the carrier concentration in the sample can be finely controlled by quenching the system at the proper value of sheet resistance and it is found that the doping process is fully reversible and does not alter graphene transparency.

Compared to the most used techniques for doping graphene, space charge doping offers a valid and for many aspects a much better alternative. Simply involving a glass substrate and without the need of other technological steps, space charge doping is able to induce carrier concentrations in graphene well beyond the techniques mentioned before (exceeding 10^{14} cm^{-2}) without damaging the sample. Space charge doped graphene could be used in applications like TCE, but graphene as a TCE has not fulfilled the expected promise in the last years, probably because of a bottleneck related to production, quality and processing of large area graphene. Other alternatives like transparent oxides can be the answer to find new transparent electrodes based on the space charge doping as we will see in Chapter 4.

Concluding, we invented the *space charge doping* as an efficient and reliable method for doping graphene and potentially other ultra-thin materials deposited on glass, allowing a fine control of the carrier density to values exceeding 10^{14} cm^{-2} , much higher than most other doping techniques.

Chapter 4

Ultra-high doping of ZnO_{1-x} thin films

Chapter 4 and Chapter 5 are partially based on our submitted paper: A. Paradisi, J. Biscaras and A. Shukla, Magneto-conductance in nearly degenerate ZnO thin films: space charge doping and localization

In the second part of this thesis I study ultra-thin zinc oxide films deposited on glass. The transport and magneto-conductance properties of these are investigated as a function of electrostatic doping using the space charge doping technique. Why zinc oxide? As we have seen the space charge doping technique is readily applicable to a well-defined single crystalline material deposited onto a substrate, which is the case of graphene. However as discussed in the earlier chapter, graphene also has shortcomings as a TCE material. Furthermore if our doping technique is versatile, we should be able to apply it to a variety of polycrystalline or even eventually amorphous thin films deposited on glass by standard deposition techniques. This was the reason to choose a large gap semiconductor like ZnO which is quite different from graphene as far as material and electronic properties are concerned, as we shall see below. We had the possibility to produce high quality samples thanks to the magnetron sputtering facility at the Institut des NanoSciences de Paris. Moreover doped ZnO, like graphene, is a widely studied material in many fields and in particular in the field of Transparent Conducting Electrodes (TCEs) and spintronics, making it easy to compare results obtained by our method with other results in literature.

Zinc oxide is a wide band-gap semiconductor with a direct band-gap of $E_g \sim 3.3$ eV at 300 K [51, 52] which makes it practically transparent in the visible range. Accordingly single crystal ZnO samples show very high resistivity of the order of $10^5 \Omega \cdot \text{cm}$ [61, 63]. The most widespread technique for the doping of ZnO, especially for TCE applications, is substitutional doping with Al atoms [62, 67, 102], though easily formed oxygen defects also

provide a route to doping and increasing conductivity. This technique can significantly lower the resistivity of ZnO to values of the order of $10^{-4} \Omega \cdot \text{cm}$, but the atomic structure and the transparency of the aluminium-doped ZnO are altered by this process. Moreover chemical doping is not reversible.

Regarding the spintronics applications, ZnO (and in general II-VI semiconductors) have obtained the attention of the scientific community thanks to the possibility of manipulating the spin-dependent magnetic phenomena in thin film systems.

Our study of zinc oxide concerns ultra-thin ($< 40 \text{ nm}$) films of ZnO_{1-x} deposited on soda-lime glass. As in most oxide films, these thin films were non-stoichiometric, containing oxygen defects. Oxygen vacancies are responsible for the n -type conductivity in ZnO [62, 63, 64] and their number can be increased by vacuum annealing thus increasing the conductivity of the material. The transport properties of the thin films are studied as a function of the carrier concentration, temperature and magnetic field. We find that space charge doping significantly alters electronic properties of the thin film and that electrostatic doping can induce an electron concentration as high as $2 \times 10^{14} \text{ cm}^{-2}$, bringing the ZnO_{1-x} thin film close to the insulator-metal transition. As in the case of graphene (Chapter 3) the carrier concentration can be finely tuned in a wide range allowing us to study the evolution of the transport properties with the respect to the carrier concentration.

4.1 ZnO_{1-x} device fabrication

We fabricated ZnO ultra-thin films on soda-lime glass with the RF magnetron sputtering method at room temperature using a Zn target in an atmosphere composed of Ar and O, following the procedure described in Section 2.1.3. The total pressure in the chamber during the deposition was kept at 10^{-2} mbar while the partial pressure of Ar and O was varied to vary the number of oxygen defects and the stoichiometry of the deposited ZnO thin film. In our experiments the partial pressures were fixed by varying the composition of gases in the range Ar= 50% - O= 50% to Ar= 80% - O= 20%. We did not perform a chemical analysis on our deposited thin films to determine the exact amount of Zn and O contained in the samples but as an indication of the initial stoichiometry obtained we cite data from Reference [103]. In this work it was found that annealing ZnO thin films produced with the same partial pressure of Ar and O (*i.e.* Ar= 50% - O= 50%) results in quasi stoichiometric ZnO. As the O partial pressure is reduced with respect to the Ar partial pressure, the ratio O/Zn decreases, for example Ar= 70% - O= 30% results in a stoichiometry of $\text{ZnO}_{0.73}$ with $x = 0.27$. The determination of the stoichiometry with wet chemical analysis on such ultra-thin films is not realistic and for our purposes the initial value of x is not crucial since we are concerned with the maximum carrier

concentration and the minimum value of R_S we can attain with space charge doping. Moreover, we found that our results are independent of the initial stoichiometry of the samples, as we shall see later. The sputtering time determines the thickness of the sample. The samples are characterized with X-ray diffraction and AFM in order to determine the crystalline properties and the exact thickness. The characterization is followed by shaping of the sample and contact deposition to fabricate the device used in transport measurements.

4.1.1 Zinc oxide deposition on glass

Our samples were deposited using a gas mixture formed by Ar= 76% - O= 24% or Ar= 80% - O= 20% which, as we saw from Reference [103], should result in ZnO_{1-x} with $x \approx 0.3$ and higher. These samples should thus have an initial defect induced carrier concentration which was our aim since stoichiometric samples have resistances beyond our measuring range. The deposition time is varied between 25 s and 120 s, so as to obtain samples with different thickness. After the deposition an annealing process in high vacuum at a temperature of $\sim 350^\circ\text{C}$ is eventually performed. The annealing further increases the oxygen vacancies in the sample through oxygen desorption from the thin film and increases the grain size at the same time through a sintering process.

The zinc oxide thin films are deposited on $\sim 1 \text{ cm}^2$ clean soda-lime glass substrates. For a given set of deposition parameters two to three substrates are used, since samples are needed for measurements as well as for characterization. Once the gases are injected in the chamber, the RF power is turned on and an Ar plasma is created causing the deposition of ZnO on the glass surface (see Section 2.3.2). A total of 15 sets of samples were made, each one characterized by a different gas mixture and deposition time. To study the effects of space charge doping on thin film ZnO samples, the deposition parameters were varied in order to modify the stoichiometry and the thickness of the samples. For a detailed study we chose to focus on four samples labelled A, B, C and D whose deposition parameters and thickness are listed in Table 4.1. The samples were intentionally deposited with a certain degree of non-stoichiometry in order to decrease the initial resistivity with some chemical doping. Then, the Ar/O ratio and the deposition time were varied to see the effect of the space charge doping on samples with different characteristics (stoichiometry and thickness). From the samples of Table 4.1 we obtained the most representative results of our study which will be analyzed in this chapter. The characterization of the samples is described in the following.

| Sample | Ar/O | Deposition time (s) | Thickness (nm) |
|--------|-------|---------------------|----------------|
| A | 76/24 | 120 | 40 |
| B | 76/24 | 66 | 23 |
| C | 80/20 | 66 | 27 |
| D | 80/20 | 25 | 7.5 |

Table 4.1: The deposition parameters of the different samples studied

4.1.2 X-ray diffraction, AFM and transmittance

Obtaining an X-ray diffraction signal on our ZnO samples was difficult because of the ultra-thin nature of the samples. The spectra are collected using a grazing geometry with an incident angle of 4° from a Cu source with a wavelength of the incident beam of $\lambda = 0.15405980$ nm. In Figure 4.1 are shown the XRD spectra obtained from the four analysed samples as deposited. Comparing Figure 4.1 (the XRD spectra of our samples) with

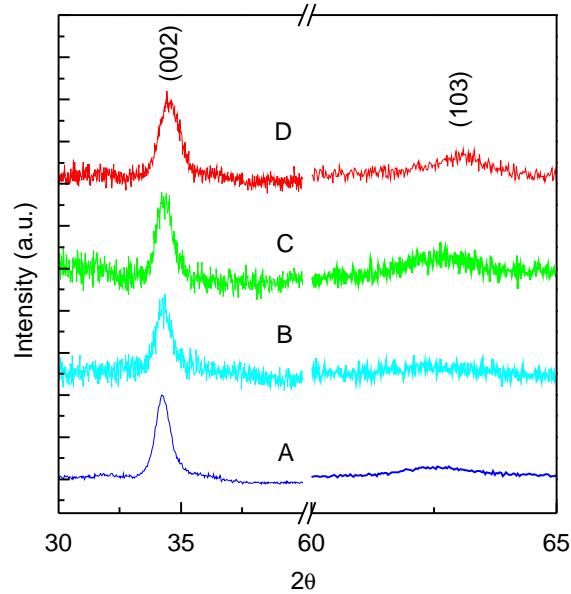
Figure 4.1: XRD spectra of samples A, B, C and D. Background due to the glass has been removed and the spectra are normalized with respect to the peak at $\approx 34^\circ$.

Figure 4.2 (the spectrum of ZnO powder) we can see that the visible peaks obtained from our samples located at $34.2^\circ < 2\theta < 34.6^\circ$ correspond to the crystalline orientation in the (002) direction [58]. We see also a small peak located at $2\theta \approx 63^\circ$ corresponding to the (103) crystalline orientation. Our thin films are thus textured with a preferential (00 l) orientation.

As explained earlier an initial carrier concentration is induced by creating oxygen defects. This facilitates the practical application of space charge

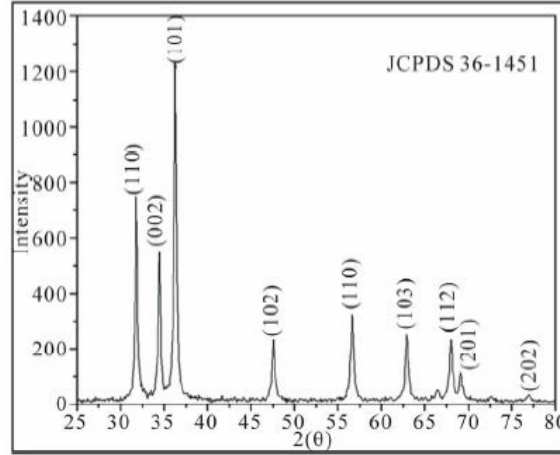


Figure 4.2: The XRD spectrum of the ZnO powder reprocessed from Chapter 1. Re-printed from [59].

doping since the sample resistivity which can be very high initially, can thus be measured over the whole process. We performed the annealing step on samples B, C and D for 15 hours at a temperature of $\sim 350^\circ\text{C}$. XRD reveals that the annealing step has an effect on the grain size, as shown in Figure 4.3. We see clearly that there is a sharpening of the peaks associated to the (002) and (103) crystalline orientations indicating a bigger grain size. We notice also that the peaks show a slight shift due to a change in the stress in the film. The average grain size of the samples has been estimated from the Scherrer formula [88] (see also Section 2.2.4) and the calculated average grain sizes calculated after the annealing step are 12.9 nm for Sample A and 12.8 nm, 11.2 nm and 10.3 nm for sample B, C and D respectively. As we saw from Section 2.2.4, performing the XRD analysis in a grazing geometry (as it is the case of our samples) while increasing count-rate through an enhanced footprint on the sample surface, can degrade the angular resolution due to the augmented source size as seen from the detector. Thus, the effective X-ray coming from coherent scattering from the sample which hits the detector can be emitted from an effective surface which is, in the worst case, as big as the sample surface [89] ($\sim 1 \text{ cm}^2$ in our case). The result is a broadening of the peaks in the diffraction pattern. However we verified that this error does not contribute significantly in our measurements and can thus be neglected.

The annealing increases the grain size of the sample. For example the full width half maximum (FWHM) of the peak associated to the (002) direction was 0.723 before the annealing and 0.583 after the annealing for sample B, while for sample C the FWHM changed from 0.755 to 0.591 after the

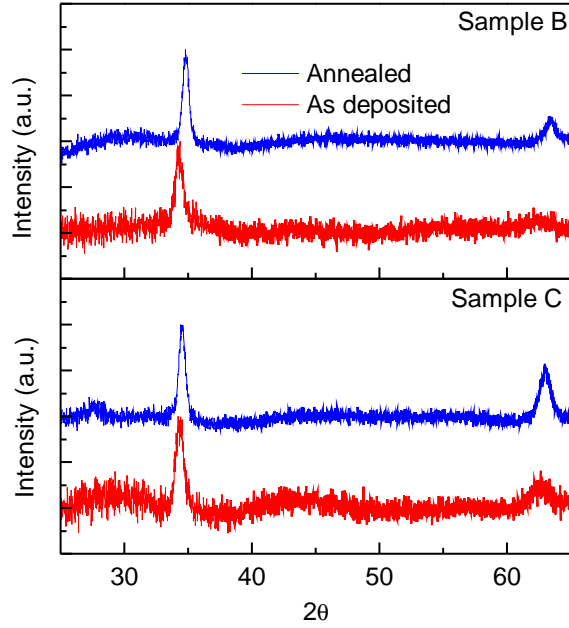


Figure 4.3: Effect of the annealing on the sample crystalline structure analysed by XRD. It is clear that the characteristic peaks of the thin film are sharper after the annealing, meaning that the grain size has increased. The spectra are normalized with respect to the peak at $\sim 34^\circ$.

annealing step. The peak position also changed, meaning a change in the strain in the film. In particular, in sample B the position of the peak changed from 34.29° to 34.81° and in sample C from 34.33° to 34.54° . This shift of the peak position to higher angles is a consequence of compressive stress caused by the annealing [62].

AFM analysis is used to scan the surface of the samples in order to obtain topographic data and compare the results with those obtained from the XRD. An example of the grain size analysis performed with AFM on sample A is presented in Figure 4.4. The height mapping of the scanned area (upper part of Figure 4.4) reveals the grains of the sample but a more accurate information about the grain size can be obtained from the mapping of the phase, presented in the lower part of the figure. However, the estimation of the average size of the grains obtained from the AFM scans is higher than that obtained from the XRD (≈ 28 nm instead of 12.9 nm calculated from XRD). Since the XRD gives information on the coherent diffraction domains related to the $(00l)$ reflections which also represent the dominant texture of the sample, we can assume that grains have an average dimension perpendicular to the sample surface of about 12 nm. The AFM measurement on the other hand gives us an average dimension of 28 nm for the grain dimension in the plane of the sample surface. The grains are thus on the average, flat discs of thickness about 12 nm and diameter about 28 nm and roughly oriented with the flat surface on the substrate surface. In Figure 4.5

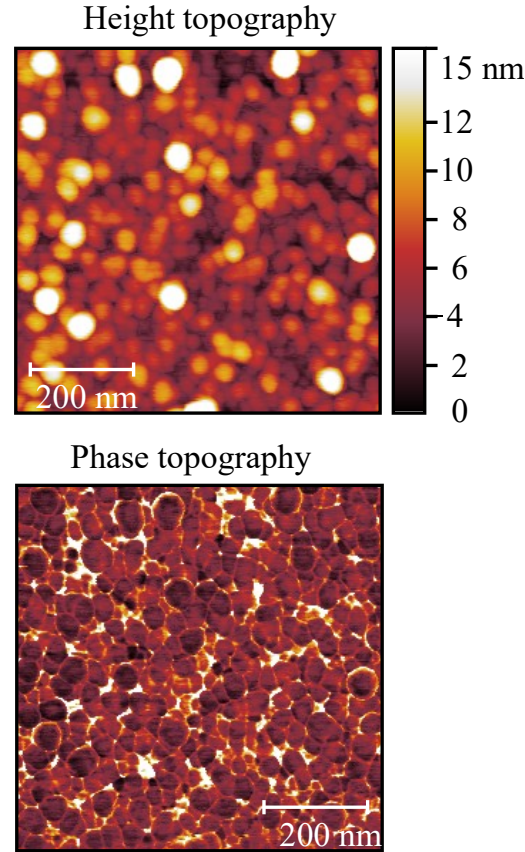


Figure 4.4: Topography of the height measured from the AFM scan (upper part) and the corresponding phase topography (bottom part). The height scan of the surface enables to see very well the grains and measure their height, but the topography of the phase displays in a clearer way the shape and the size of the grains.

it is shown from a schematized lateral view the deduced shape of the grains of our ZnO samples.

The thickness of the ZnO samples is also estimated with AFM. A part of the sample must be etched away in order to obtain a sharp step. The edge of the sample is thus scanned with the AFM and the height of the step between the glass and the top of the sample can be measured. An example is shown in Figure 4.6 where the thickness of sample C is measured.

The RF-magnetron sputtering method is a standard way to produce ZnO thin films. ZnO thin films are mainly used to fabricate transparent devices or for the study of their electronic properties. Our results on the fabrication and characterization of the samples are in excellent agreement with published data. The crystalline orientation of the film usually depends

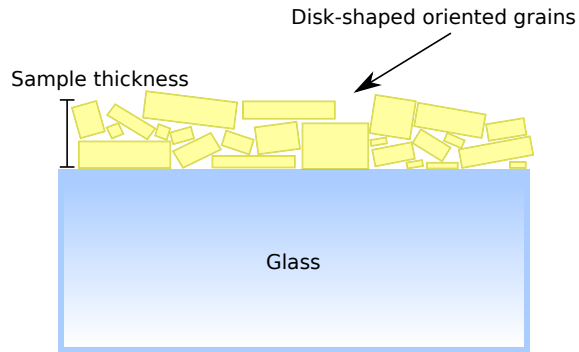


Figure 4.5: Schematization of the shape of the grains of our ZnO thin-films in a lateral view. The grains lateral size is bigger than their height are suggested from the AFM and XRD measurements.

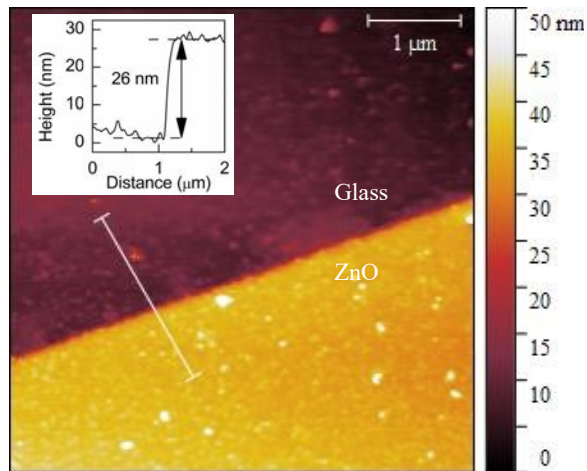


Figure 4.6: Thickness measurement of the sample. The edge of the sample is very sharp after the etching in the aqueous solution of HCl.

on the substrate used and the deposition technique. With the RF sputtering method it is often found that the preferred crystalline orientation of the film is the $(00l)$ direction [60, 63, 69, 83, 104]. The grain size of our films is generally lower than what is found in literature. The grain size estimated in Reference [61] for example is 32 – 38 nm. Our films are ultra-thin and grown

on an amorphous substrate. The samples of the aforementioned references are in fact thicker than our samples ranging from ~ 70 nm to $1 \mu\text{m}$ and in general grown on crystalline substrates.

Transmittance measurements were also used to characterize the ZnO thin-films. ZnO absorbs a really small fraction of the visible light thanks to its wide band-gap. ZnO transmittance in the visible range can exceed 90% [105] and vary with the thickness. Our ZnO samples show a transmittance $> 94\%$ in the visible range of wavelengths as shown in Figure 4.7.

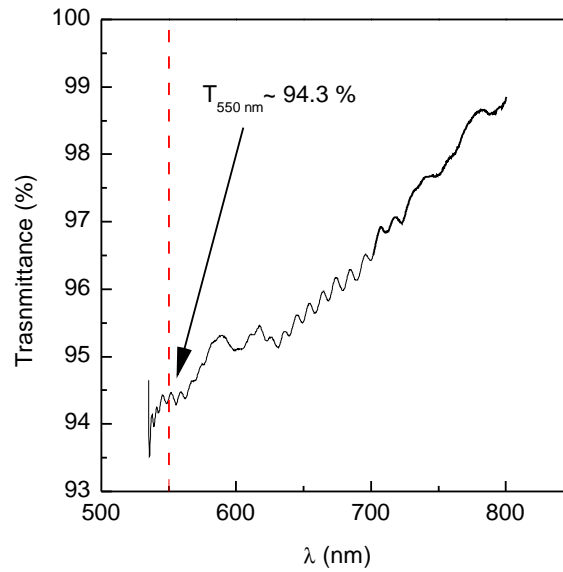


Figure 4.7: Transmittance of sample C measured after the annealing process..

We briefly mention the characterization of our ZnO thin film with μ -Raman spectroscopy. ZnO presents some characteristic peaks dominated by a peak at 570 cm^{-1} and other characteristic peaks around it [106]. We attempted the characterization of our ultra-thin films by means of μ -Raman spectroscopy by performing very long acquisitions with an excitation laser wavelength of 532 nm and by doing multiple acquisitions in order to filter the noise. The results were not encouraging since our samples are very thin and transparent and the obtained spectra are dominated by the substrate background. Raman spectroscopy is thus not adapted for the characterization of our samples.

4.1.3 Sample shaping and contact deposition

As in the case of graphene, the ZnO samples must be shaped and contacted for the transport measurements. As described in Section 2.3, to give the zinc oxide the proper shape it is necessary to cover the sample with a drop of PMMA, leaving uncovered the parts of the sample which have to be etched

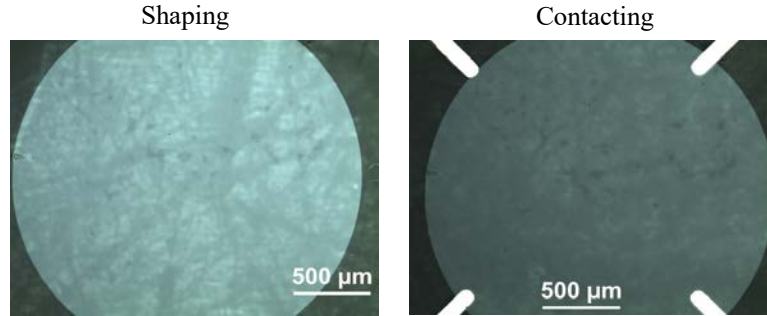


Figure 4.8: A typical ZnO sample after the etching process and before the contact deposition.

away. A rapid immersion (7 s) in an aqueous solution of HCl at 15% will corrode the ZnO which is not protected by the polymer. A successive bath in warm (50°C) acetone for about 30 minutes will remove the PMMA leaving the etched zinc oxide on the surface of the glass. In the left part of Figure 4.8 sample C is shown after the etching step. The sample has a diameter of about ~ 2 mm and an area of ~ 3.2 mm². After this step a stencil mask like the one used for the CVD graphene (Section 3.2.1) is aligned to the sample and gold is evaporated through it. The result is presented in the right part of Figure 4.8.

4.2 Space Charge Doping applied to the ZnO thin film

This section is dedicated to the space charge doping of the ZnO samples. The samples are doped with the procedures described in Section 3.2.2, *i.e.* either by heating the sample and applying the gate voltage once T is stable, or by applying V_G at room temperature and then heating the sample to the target doping temperature, with this latter technique allowing for the highest values of carrier concentration to be reached, as in the case of graphene.

4.2.1 Fine control of doping in the thin film

The initial resistivity of ZnO can vary considerably from sample to sample due to the different initial carrier concentration determined by the oxygen vacancies. The initial sheet resistance of the four samples under examination are listed in Table 4.2. Sample A shows a considerably high initial sheet resistance since no post-deposition annealing is performed on this sample and the oxygen vacancy induced carrier concentration is relatively low. Samples B and C present an initial R_S of the order of few tens of $\text{k}\Omega/\square$ as a result of a higher oxygen vacancy induced carrier concentration due to post-deposition

| Sample | Initial R_S (Ω/\square) |
|--------|------------------------------------|
| A | $\sim 10^8$ |
| B | 6.2×10^4 |
| C | 4.0×10^4 |
| D | 3.2×10^6 |

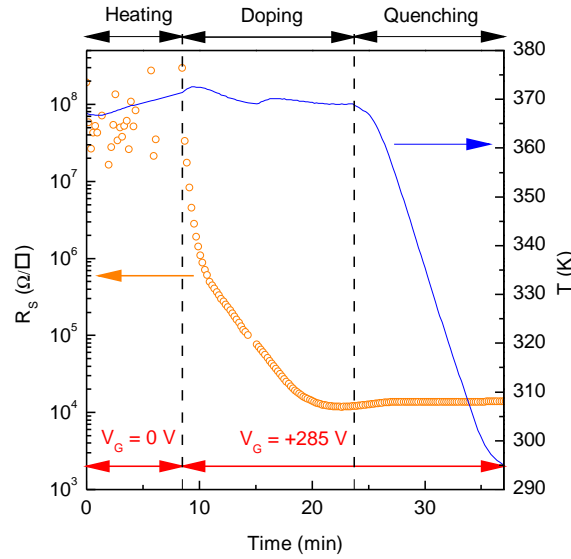
Table 4.2: R_S values of the four ZnO samples examined before space charge doping.

Figure 4.9: Space charge doping applied to Sample A. The initial sheet resistance of the sample was $R_S \approx 10^8 \Omega/\square$. The sample is first heated at ~ 370 K and then a gate voltage $V_G = +285$ V is applied. As observed, the space charge of Na^+ ions forming at the interface between the glass and the ZnO thin film cause a massive drop in R_S of ~ 4 orders of magnitude in just 10 minutes.

annealing. We notice also that the initial R_S of sample B is slightly higher than sample C, as a consequence of the initial oxygen stoichiometry of the samples as determined by the partial pressures of argon and oxygen during deposition. From Table 4.1, in sample B $P_{\text{Ar}}/P_{\text{O}} = 76/24$ while in sample C $P_{\text{Ar}}/P_{\text{O}} = 80/20$. This difference persists after the annealing and this is reasonable since the annealing time and temperature for the two samples are the same. Sample D which was subjected to the same annealing process as samples B and C, shows a relatively high initial R_S of the order of $10^6 \Omega/\square$. This is because it is the thinnest film.

The effect of space charge doping on ultra-thin ZnO films is impressive and clear. It lowers R_S by 4 orders of magnitude or more. As an example, in Figure 4.9 we show sample A which had the highest initial R_S of $10^8 \Omega/\square$ of our four samples. This is at the upper limit of our measurement apparatus and falls in a spectacular way during the doping procedure. The sample is heated to the doping temperature of ~ 370 K and at that point a gate

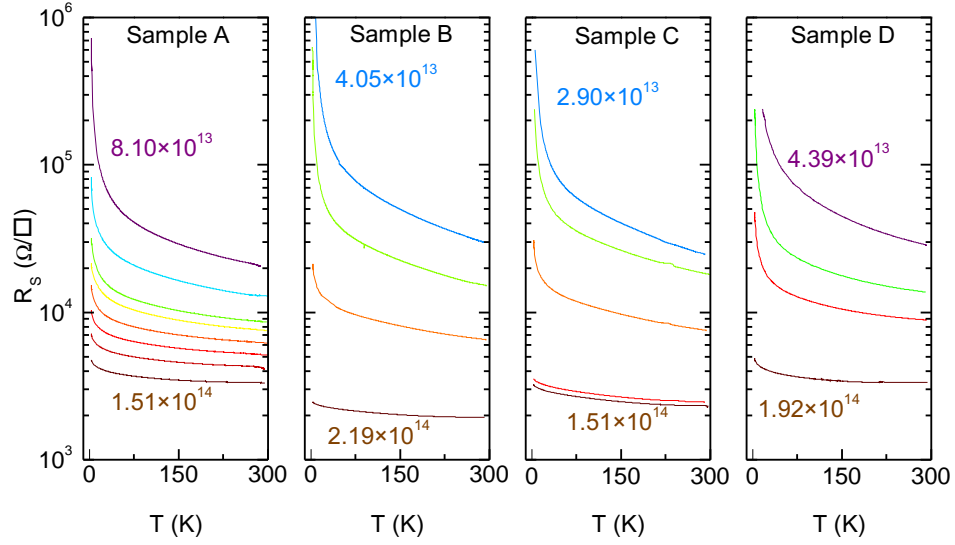


Figure 4.10: R_S vs T characteristics in a wide range of carrier concentrations for sample A, B, C and D. Even at the highest carrier density (which is always higher than 10^{14} cm^{-2}) the samples show an insulating behaviour.

voltage of +285 V is applied. An abrupt drop in the resistivity is observed as the consequence of the space charge forming at the interface. As the doping increases, the resistivity drop rate slows to zero after about 10 minutes. At this point the temperature is quenched to room temperature where $R_S = 14 \text{ k}\Omega/\square$. Thus a drop in resistivity of a factor 10^4 is produced with space charge doping. The carrier concentration measured with the Hall effect at room temperature after the doping is $5.4 \times 10^{13} \text{ cm}^{-2}$.

The carrier density can be finely controlled, exactly like it was done for graphene, by quenching the system at the desired sheet resistance value. In Figure 4.10 are shown several R_S vs T characteristics in the range $4\text{K} < T < 300\text{K}$ at several values of carrier density. The first thing to be noticed in these graphs is that the maximum reached carrier concentration is very similar for all the samples. The maximum carrier concentration attained always exceeds 10^{14} cm^{-2} electrons, ranging from 1.51 to $2.19 \times 10^{14} \text{ cm}^{-2}$ independent of the initial carrier concentration. Space charge doping thus induces charges in a similar manner to chemical doping as confirmed by the similarity between the curves obtained at different doping from the four samples. The sheet resistance showed by the four samples at the highest doping is also very similar being $2 - 3 \text{ k}\Omega/\square$ at room temperature in all cases. The variation is attributed mainly to the difference in the carrier mobility of the samples. We also notice that, like in the case of graphene, the space charge doping is able to induce in ZnO an extremely high doping in a reversible way. In fact, the doping procedure is usually carried out by first inducing the highest possible carrier density in the thin film and

then progressively reducing the doping. Moreover, like in graphene, the transmittance of the sample measured after the doping process is not altered and it shows a behaviour similar to that shown in Figure 4.7.

Chemical doping with Al is the most widely used technique for doping ZnO, especially for practical applications like transparent conducting electrode (TCE). This technique is very effective for reducing the resistivity of ZnO. In Reference [62] aluminium doped ZnO is produced with RF sputtering using a Zn target mixed with Al. They found that the maximum carrier concentration induced in the sample is $9.2 \times 10^{20} \text{ cm}^{-3}$ which is equivalent to a carrier concentration in two dimensions (in a 1 nm thick sample) of almost 10^{14} cm^{-2} and the corresponding resistivity of the film is $\sim 4 \times 10^{-4} \Omega \cdot \text{cm}$. To compare the resistivity of our 2D samples with the published data we have to calculate the resistivity starting from the sheet resistance of the samples. In Reference [72] the thickness of a quantum well induced on the surface of ZnO is calculated to be of the order of few nanometers. We can thus assume that in our ZnO samples the thickness which is effectively doped by the space charge is of the order of the nanometer. The resistivity can be calculated from $\rho = R_S \cdot t$, with t the thickness of the doped ZnO. The lowest R_S in all the analyzed ZnO samples is of the order of the $\text{k}\Omega/\square$, thus the resistivity of our doped samples is of the order of $\rho \sim 10^{-4} \Omega \cdot \text{cm}$. This value is comparable with the one found for Al doped ZnO in Reference [62]. In Reference [68] slightly different results are found with a resistivity of the Al doped ZnO being $\sim 4 \times 10^{-3} \Omega \cdot \text{cm}$ at a doping of $2 \times 10^{20} \text{ cm}^{-3}$. Space charge doping is thus as effective as aluminium doping of ZnO, but with the immense advantage of being reversible and not altering the transparency (which can be as low as 80% for Al doped ZnO) and quality of the thin film. The resistance of our thin film still remains high for TCE applications as a consequence mostly of low electronic mobility which could be improved by improving the crystalline quality. In the aforementioned papers the thickness of ZnO varies from 100 nm to 0.8 mm, with bulk conduction.

Polymer electrolyte doping has been described in References [70, 71]. Similarly to the space charge doping, polymer electrolyte doping exploit the mobile ions present in the polymer to create a space charge at the interface of the material which dopes it. In those papers, carrier densities up to $4 \times 10^{14} \text{ cm}^{-2}$ or more have been measured on the surface on ZnO. The authors claim that this kind of doping is reversible, but the doping procedure raises many questions about intercalation of foreign species in the ZnO structure and on the reliability of the measured data since the ions of the polymer electrolyte responsible for the doping are considerably mobile in a wide range of temperatures and can thus alter the measurements. As seen in Figure 5 of Reference [70] we can see that the carrier density induced by the polymer electrolyte varies considerably with the temperature. Moreover polymer electrolyte is not suitable for practical applications because it alters the transparency of the film and contaminates it.

We mention also the results obtained in References [60, 63] where transparent transistors using ZnO as active material have been used. The whole transistor structure (gate electrode, source and drain electrodes and gate dielectric) has been realized using transparent materials but does not allow to reach very high carrier concentration levels.

Despite the really high doping (always exceeding 10^{14} cm^{-2}) we are able to induce, we do not observe an insulator-metal transition in our samples. This behaviour is coherent with results from literature [70, 107]. In Reference [107] impurity doped ZnO thin films $\sim 400 \text{ nm}$ thick are deposited on glass with the spray pyrolysis technique with carrier concentration of $10^{18} - 10^{20} \text{ cm}^{-3}$ (corresponding to $10^{12} - 10^{13} \text{ cm}^{-2}$ in a 1 nm thick material). An insulating material is characterized by a dependence of the conductivity of the temperature like $\partial\sigma/\partial T > 0$ and the transition to the metallic state is observed when $\partial\sigma/\partial T < 0$ (*i.e.* $\partial\rho/\partial T > 0$). In the aforementioned paper this transition is not observed since only a flattening of the R_S vs T characteristic is observed and not a clear transition to the metallic state. This is similar to what we observe in our sample at the highest carrier concentration and, as we'll see in Chapter 5, the increase of the sheet resistance at low temperature is due to the Weak Localization phenomenon. In Reference [70] (Figure 5a) at the highest carrier concentration it appears that a metallic-like behaviour ($\partial\rho/\partial T > 0$) is observed at high temperature ($150 \text{ K} < T < 250 \text{ K}$) for polymer electrolyte doped ZnO. However in this range of temperature the authors state that the mobility of the ions in the polymer is still significant and contributes to charge transport. In fact, below 150 K where ion mobility is negligible, the sample shows insulating behaviour. Thus we conclude that the insulator-to-metal transition in ZnO is not easy to induce and to date has not been clearly observed. Later in this chapter we examine this problem with the concept of mobility edge.

Space charge doping can thus induce really high electron density in ZnO thin films to values comparable with the most used techniques like chemical doping. Furthermore the process is perfectly reversible and the transparency of the thin film is not altered. In a mechanically stable material like ZnO even an extremely doping does not induce material damage and allows perfect reversibility of the doping process.

4.2.2 Carrier scattering mechanism

The understanding of the main scattering process in ZnO thin films, doped or not, is essential for understanding the transport properties exhibited by these samples. Generally speaking, in a polycrystalline thin film there are three main scattering mechanisms: scattering from grain boundaries, from thermal lattice vibrations and from ionized and neutral impurities [108]. However, the scattering cross section of neutral impurities scattering is small compared to that of ionized impurities and can be neglected. Thus we can

express the total mobility of the carriers as:

$$\frac{1}{\mu} = \frac{1}{\mu_{gb}} + \frac{1}{\mu_{ph}} + \frac{1}{\mu_i} \quad (4.1)$$

where μ_{gb} is the mobility limited by the grain boundaries, μ_{ph} is the mobility limited by phonons and μ_i is the mobility limited by the ionized impurities.

Lattice phonon scattering

Scattering from lattice vibration can be the dominating scattering mechanism in polycrystalline thin films at high temperature. The dependence of the mobility at high temperature [108] should then be such that

$$\mu_{ph} \propto \frac{1}{T} \quad (4.2)$$

thus μ should decrease with increasing temperature at high temperature.

However this behaviour is not relevant to our data since we shall analyze data collected at low temperature (< 50 K).

Grain boundary scattering

Our ZnO samples are, as we saw, formed by aggregated crystalline grains. The junction between two crystallites is characterized by lattice defects-induced trapping states which compensate the doping in the material by trapping the electrons in the conduction band. Thus a depletion region is formed around the grain boundaries to which is associated a potential barrier which can strongly affect the motion of conduction electrons. According to the Peritz equation [109] the expression for the mobility in the presence of grain boundary scattering is

$$\mu_{gb} = \mu_0 T^{-1/2} e^{-\phi_b/k_B T} \quad (4.3)$$

where μ_0 can be considered as the mobility inside the grain, ϕ_b is the potential barrier height at the grain boundary and k_B is the Boltzmann constant.

If the main scattering mechanism is grain boundary related, a plot of $\ln(\mu T^{1/2})$ vs $1/T$ should give a straight line. Figure 4.11 shows such a plot for our samples. The mobility is the Hall mobility extracted from the Hall measurements performed at 50, 25, 10 and 4 K. Two sets of data are displayed for each sample, one corresponding to high doping and one corresponding to low doping (relatively to the range of doping we studied). In our thin film samples grain boundaries do not play a dominant role in the carrier scattering mechanism, since in the plot of Figure 4.11 all the curves deviate from a linear behaviour.

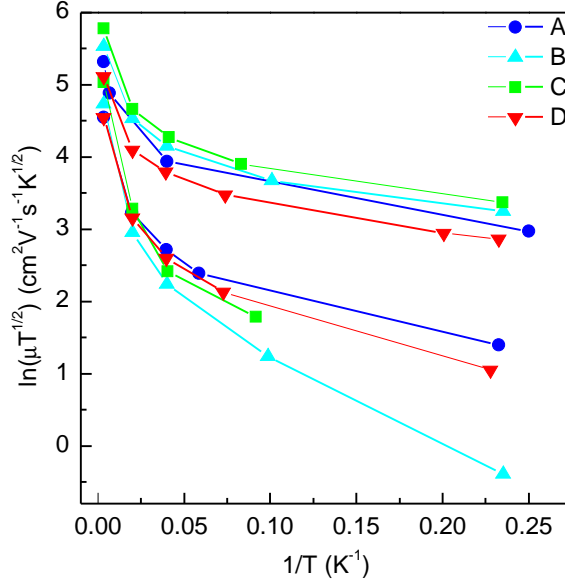


Figure 4.11: $\ln(\mu T^{1/2})$ vs $1/T$ plot for the four analysed samples. For each sample we display two curves: one corresponding to high doping and one to low doping. The non linearity of the curves suggests that grain boundaries are not the main scatterers in the carrier transport.

However, even if not dominant, grain boundaries do play a role in the transport properties of our ZnO thin films. According to the discussion in Reference [110], the expression of ϕ_b in Equation 4.3 has the form:

$$\phi_b = \begin{cases} \frac{e^2 Q_t^2}{8\epsilon\epsilon_0 n_s}, & Ln_s > Q_t \\ \frac{e^2 L^2 n_s}{8\epsilon\epsilon_0}, & Ln_s < Q_t \end{cases} \quad (4.4)$$

where L is the grain size, Q_t is the charge carrier trap density at the boundary and n_s is the carrier density. Thus we have two limiting cases: (i) at high carrier density, where at a fixed temperature the barrier height decreases with increasing n_s , (ii) at low carrier density the barrier height increases with increasing carrier density. Thus in case (i) the mobility increases with n_s , in case (ii) it decreases with n_s . Figure 4.12 shows the dependence of the mobility with respect to the carrier density in our samples at 25 K. We see that the mobility increases for all the samples with carrier concentration. This effect is however secondary in our thin film as shown in Figure 4.11 and as explained in the following.

Ionized impurity scattering

In (conducting) oxides in general ionized impurities play an essential role in the scattering mechanism of charge carriers. Generally speaking, ionized

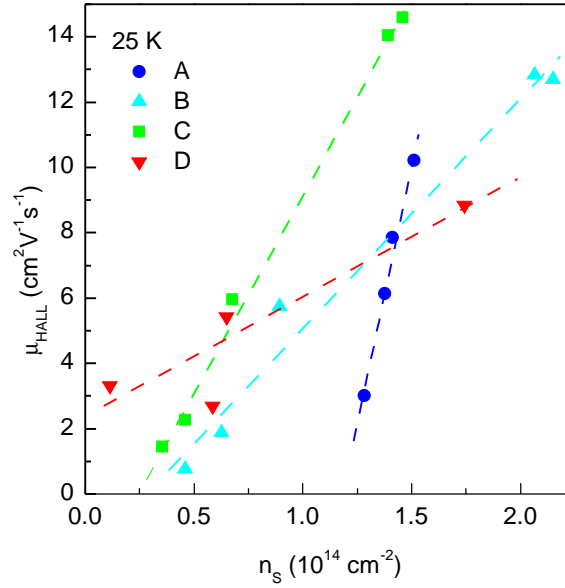


Figure 4.12: Dependence of the mobility on the carrier concentration for sample A, B, C and D measured at 25 K. The increase of μ with n_s indicates that the samples are in the condition of high doping as highlighted in Equation 4.4 and that the grain boundaries do influence transport properties of the ZnO thin films without dominating them.

impurities can be represented by foreign atoms introduced in the crystalline network like dopants (in doped films) or oxygen vacancies (like in our ZnO samples). This scattering mechanism can be recognized again by the temperature dependence of the mobility which should vary like [111, 112]

$$\mu_{ii} \propto T^{3/2} \quad (4.5)$$

Figure 4.13 shows μ vs $T^{3/2}$ of the Hall mobility of the four analysed samples measured at 50, 25, 10 and 4 K. The carrier density indicated in the plot for each curve is measured at room temperature.

The linear behaviour of the Hall mobility with respect to $T^{3/2}$ clearly suggests that the ionized impurities govern the scattering process in the ZnO thin film. Since no foreign atoms are added as dopants, the ionized impurities can only be the oxygen vacancies in the ZnO thin film.

4.3 Variable Range Hopping and mobility edge

The transport properties of disordered systems (like our ZnO thin films) can be studied in terms of localized and extended states [113]. A very simplified picture in one dimension can be used to argue that in an ordered system, the potential profile experienced by the charges in the material will be like the one showed in the upper part of Figure 4.14. B is the tight-binding bandwidth in the absence of disorder. If disorder is present in the system,

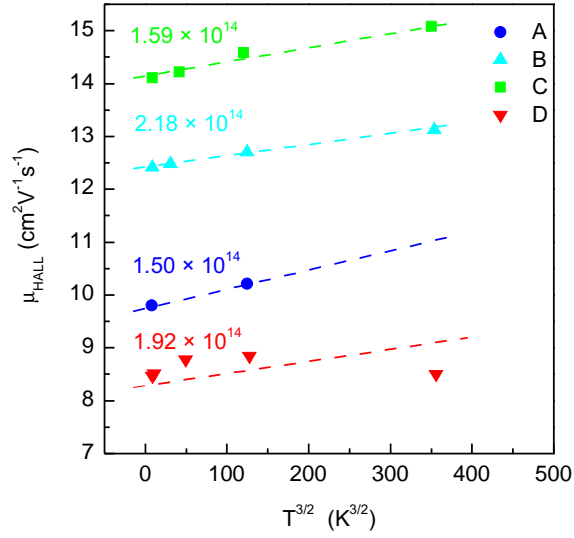


Figure 4.13: Linear dependence of the mobility with respect to $T^{3/2}$, indicating that the main scattering mechanism is due to ionized impurities.

the potential wells instead of being uniform will be spread over a range of energies V_0 , as shown in the lower part of Figure 4.14. It has been shown

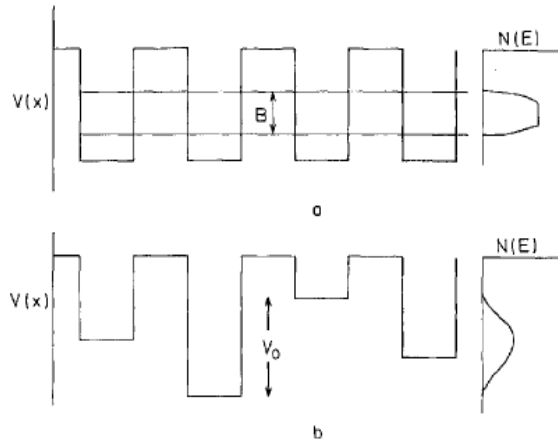


Figure 4.14: Simplification in one-dimension of the shape of the potential in a materials in the ordered (upper part of the figure) and disordered (lower part) case. Re-printed from [113].

by Anderson [114] that if $V_0/B \gg 1$ all the states in the band are localized and take the form

$$\Psi = \left[\sum C_n e^{i\phi_n \psi_n} \right] e^{-\alpha r} \quad (4.6)$$

where the part of Equation 4.6 in the brackets is the wavefunction of the electrons in the absence of disorder and the exponent outside the brackets shows how the wavefunction decays exponentially with the distance from the well. Thus when states are localized conduction can be obtained only by thermally activated hopping between the wells.

In terms of energy, the localized states are separated from extended states by a particular energy value E_c which is called the *mobility edge*. We can distinguish two cases: (i) the Fermi energy lies above E_c , thus the mobility will depend slightly on the phonons and in general the conductivity will have a metallic like behaviour ($\partial\sigma(T)/\partial T < 0$); (ii) if $E_F < E_c$ the electrons will have a thermally activated mobility and the behaviour of the conductivity with the temperature will have the form [115] at high temperature

$$\sigma(T) = \sigma_0 \exp(-(E_c - E_F)/kT) \quad (4.7)$$

with k the Boltzmann constant. At low temperature the conductivity takes the form

$$\sigma(T) = \sigma_0 \exp(-A/T^{1/(1+D)}) \quad (4.8)$$

where D is the dimensionality of the system. Thus in three dimensions the dependence of $\ln(\sigma(T))$ with respect to the temperature would be linear with respect to $T^{-1/4}$, while in the 2D case it would be linear with respect to $T^{-1/3}$.

4.3.1 Variable range hopping in ZnO thin films

Our ZnO thin films can be considered as disordered systems since they are characterized by a strong polycrystallinity. It is thus reasonable to analyze the scattering phenomena in our samples in terms of variable range hopping (VRH). As said before, VRH is a consequence of disorder in materials. In this situation the potential seen by an electron travelling through the material is characterized by potential well of unpredictable depth where the electrons are trapped. Only thermal energy can help the electrons to get out of the well. VRH thus manifests itself with an important increase in the resistivity at low temperature as described by Equation 4.8. In principle it is possible to discriminate if the electronic transport is confined in two dimensions or if it is in 3D by plotting the $\ln(R_S)$ vs $T^{-1/(1+D)}$ (with D the dimensionality of the system) as shown in Figure 4.15. The upper part of the figure shows the 2D case, while the lower part the 3D case. We see that it is quite hard to discriminate between 2D or 3D transport since all the curves (both in the 2D and 3D case) have a linear behaviour in the low temperature part.

VRH is thus not a good tool to understand the dimensionality of our system. Hence it is not possible to determine the dimensionality of the

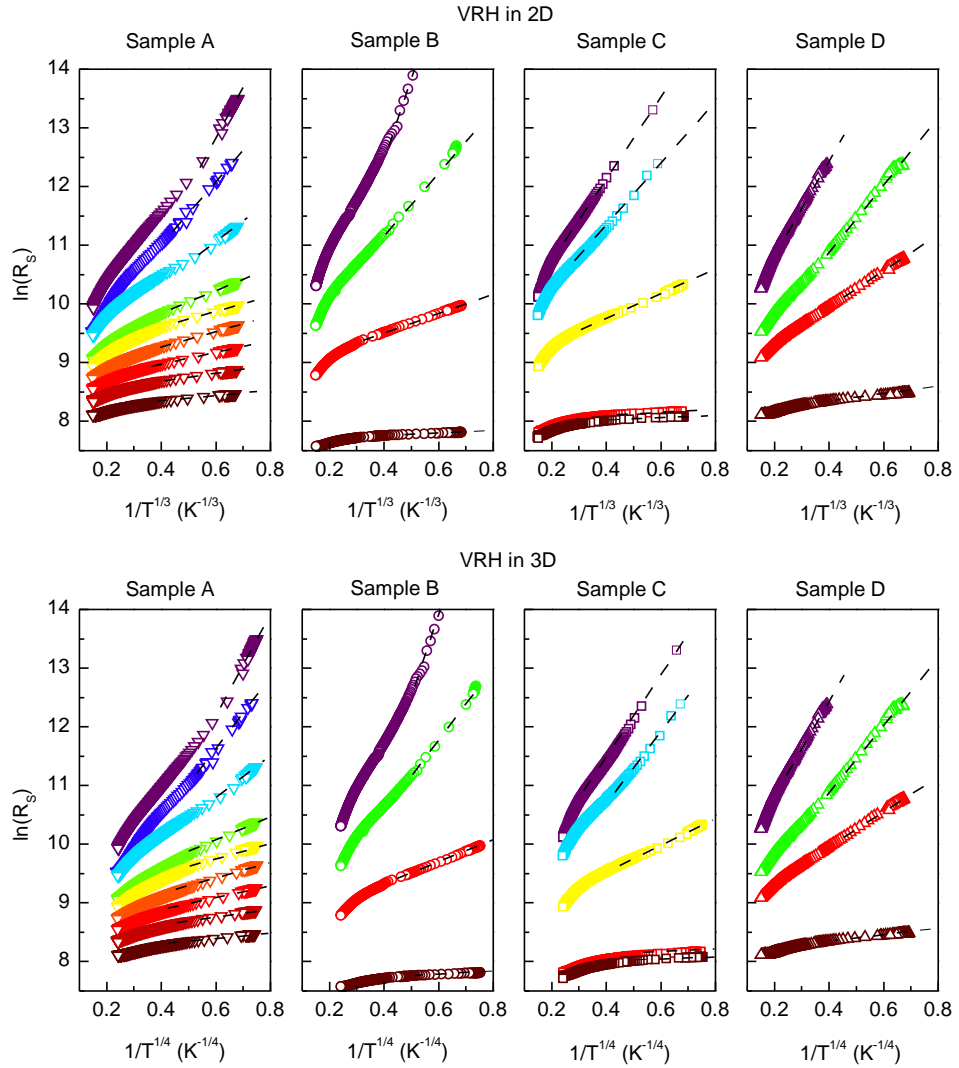


Figure 4.15: Variable range hopping in ZnO. Upper part of the figure: VRH in the 2D case. Lower part of the figure: VRH in the 3D case. We can see that for both types of behaviour the data appears linear in the low temperature part making it impossible to discriminate the dimensionality from this argument.

transport mechanism with these considerations. However since we do observe variable range hopping in both graphs through the obvious linear dependence of $\ln(R_S)$ vs $T^{-1/(1+D)}$, the transport can be assumed to be of the VRH type.

4.3.2 Mobility edge

Equation 4.6 affirms that the electrons are spatially localized around the potential wells. In the conduction band of a disordered material it is possible

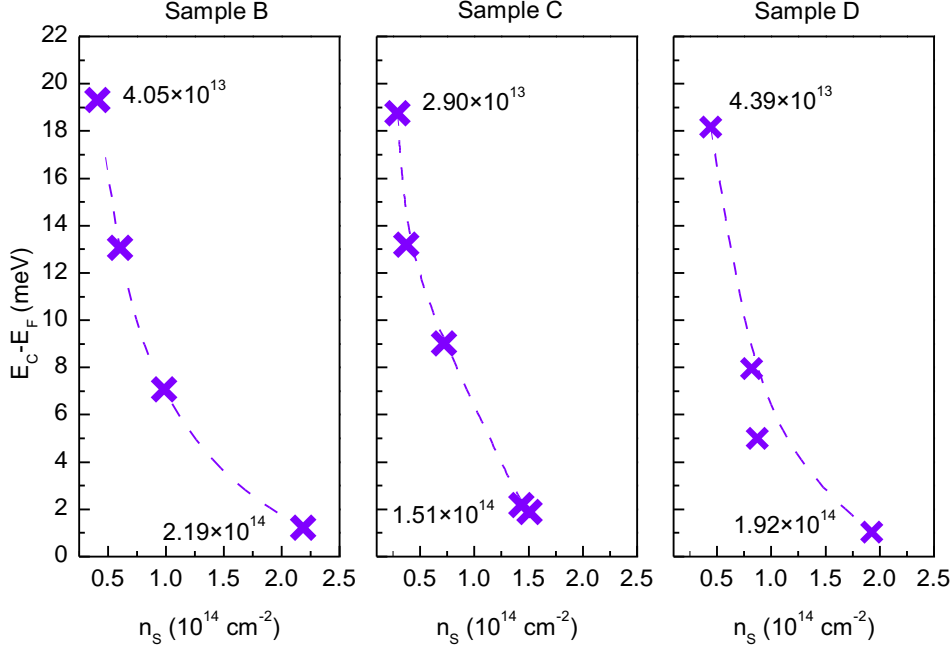


Figure 4.16: Value of ΔE extrapolated from Equation 4.7 for samples B, C and D for various carrier concentrations.

to identify a certain energy E_c which marks the transition from localized to extended states which is called *mobility edge*. If the Fermi energy is smaller than E_c the mobility of the charge carriers is thermally activated while it becomes independent of temperature if $E_F > E_c$. In the words of Mott [116]: *A mobility edge is defined as the energy separating localised and non-localised states in the conduction or valence bands of a non-crystalline material, or the impurity band of a doped semiconductor.* It thus marks the transition from the insulating to the metallic state. In Figure 4.10 we see that all samples show insulating behaviour because resistance increases as temperature decreases. However clearly, with increasing doping a metal-insulator transition is approached without being reached at the highest doping values attained. In other words the Fermi energy remains below the mobility edge.

From Equation 4.7 it is in principle possible to evaluate the energy ΔE separating the Fermi level from the mobility edge E_c by plotting $\ln(\sigma(T))$ as a function of $1/T$ and taking the slope of the straight line obtained in the high temperature part of the curve. This was done for samples B, C and D and the result is shown in Figure 4.16. We see that the ΔE is very small, of the order of a few meV for the highest doping. This is not realistic since thermal excitation would delocalize electrons but the absolute value of ΔE is probably not of significance. ΔE is positive, indicating that E_F is below the mobility edge and it becomes smaller when the doping increases, confirming that E_F is approaching the region of delocalized states. This is an aspect

which should be investigated more in detail because in all probability the transition to the metallic state is not sharp but gradual (as mentioned in [113]).

The study of the electronic transport properties inside transparent oxides is important for practical applications. In fact, the understanding of the scattering mechanisms involved during the electron motion is crucial for the design of efficient devices. Our conclusions on the scattering mechanisms in ZnO are consistent with previous published work. For instance, in Reference [117] the authors conducted a study on oxygen deficient ZnO thin films and concluded that the electronic transport is dominated at low temperature by VRH. The same conclusions are drawn for chemically doped samples like in References [118, 119] where the resistivity of ZnO doped respectively with Y and Mn are studied as a function of the temperatures and the VRH was found to be active in all the cases. However, as shown before the transition to the metallic state (thus the transition from localized to extended states) is not an easy task to accomplish in ZnO and no evidence has yet been cited in literature.

We can thus conclude that in (electrostatically or chemically) doped ZnO thin film VRH is a key element in the electronic transport. Eventually, an extremely high doping can bring the system in a condition where the mobility is independent of temperature *i.e.* where the states occupied by the electrons are delocalized, but this situation has not been experimentally found as yet. In our study on space charge doped ultra-thin ZnO films we were able to induce carrier concentrations such that the transition to the metallic state was very close.

4.3.3 2D nature of the doped film

Even if the phenomenon of the VRH discussed in Section 4.3.1 does not allow to uniquely confirm that the carrier transport is done in two dimensions, it is anyway reasonable to think that it is so. First of all, as discussed before, calculations on the width of ZnO quantum wells done in Reference [72] suggest that the accumulation of the electrons at the surface of a ZnO crystal is of the order of few nanometers. We can thus imagine that the Na^+ space charge formed at the glass/ZnO interface induces a strong accumulation layer at the interface itself. Moreover, and most importantly, the results we obtained from the four representative samples are independent on the sample thickness and stoichiometry being very similar in terms of maximum n_s , minimum R_S , values of mobility and, as it will be shown in Chapter 5, behaviour of the resistivity under the effect of a magnetic field.

4.4 Conclusions on space charge doping of ZnO

Zinc oxide thin film samples were deposited on glass substrates with the RF magnetron sputtering technique at room temperature, fully characterized using XRD and AFM measurements and prepared as devices ready for space charge doping and transport measurements.

The results presented in this chapter show that space charge doping can be used to dope ultra-thin films of ZnO to extremely high carrier concentration exceeding $2 \times 10^{14} \text{ cm}^{-2}$. This fact is of particular interest because it opens a completely new perspective in the use of this doping technique, firstly for a wide variety of materials deposited by diverse techniques on glass substrates and secondly for a variety of applications, for example in the field of Transparent Conducting Electrodes where transparent oxides are normally doped exclusively by chemical means in order to increase their conductivity. We showed that space charge doping can obtain results superior to other techniques in terms of maximum doping of the ZnO thin film without altering the sample quality and transparency in particular with respect to chemical or polymer electrolyte doping. The resistivity of the space charge doped samples is also comparable with the lowest reported resistivity, but the ultimate resistance of our samples is still high for TCE applications and this problem could be eventually overcome with the use of higher quality thin films.

Hall measurements were performed at different temperatures in the range 4 – 50 K for all the carrier densities in each sample in order to determine the variation of the Hall mobility (μ_H) with the temperature. The study of μ_H vs T revealed that the main scattering mechanism for electrons is charged impurity scattering which we identified with the oxygen vacancies present in the ZnO. Grain boundaries have also an effect on the transport properties, but they do not provide the dominant scattering mechanism in the material.

The carriers in our ZnO thin films obey the variable range hopping mechanism at low temperature. In fact, the random potential induced by the disordered lattice of ZnO is such that the electrons wavefunctions are localized for all doping levels that we can attain. An insulator-metal transition should be observed if E_F crosses a certain energy value E_C called *mobility edge* separating localized states from delocalized states. Our measurements show that with space charge doping we attained doping values which place our samples at the threshold of this transition. Moreover, the perfect similarity of the results on samples of different thickness and stoichiometry suggests that the electronic transport is confined in two dimensions at the interface with the glass substrate.

Chapter 5

Magneto-transport and spin orbit coupling

In Chapter 4 we have detailed the procedure for doping ZnO thin films to very high carrier concentrations and discussed scattering mechanisms which can intervene to explain the transport properties that we observe. These properties are principally determined, we found, by the impurity scattering mechanism. At low temperatures and eventually in the presence of a magnetic field electronic transport in a disordered medium can exhibit some specific quantum interference effects related to coherent transport and the electronic spin. These effects can significantly change conductivity. The first aspect gives rise to negative magnetoresistance through the phenomenon of *Weak Localization* and the second aspect can suppress this behaviour through the phenomenon of *Weak anti-Localization*. The measurement of both these phenomena can give access to information of the dimensionality of the observed phenomenon and quantities like the spin relaxation time. Spin orbit coupling in ZnO is thought to be small, because the valence band splitting is of the order of a few meV, almost two orders of magnitude less than in GaAs for example [120]. Nevertheless experiments [76, 78, 120, 121] have found significant effects of spin orbit coupling in ZnO. This could be justified by the wurtzite structure of ZnO as argued in [122]. ZnO is also widely studied because of predictions of possible applications in spintronic devices with appropriate doping. It is known that quantum interference phenomena like the aforementioned weak localization exist in ZnO and more rarely weak anti-localization has also been observed. In the work found in Reference [72] for instance, the magneto-transport properties of high carrier concentration (up to $5 \times 10^{14} \text{ cm}^{-2}$) ZnO surface layers produced with a variety of methods are studied and the authors found that the samples show the weak localization phenomenon up to room temperature. Spin-related phenomena have also been studied [120, 123, 124] and it was found that in ZnO system the spin coherence time can be of the order of 10 ns and can

be measured up to room temperature.

This chapter is dedicated to the study of the magneto-transport properties of space charge doped zinc oxide thin-films as a function of the temperature and doping. We analyse conductivity as a function of the magnetic field and temperature and derive information about the mean free path, inelastic scattering times and spin-coherence time.

5.1 Weak localization

Weak localization (WL) is a quantum interference phenomenon experienced by charges moving in a disordered medium at low temperature. WL gives rise to a negative correction to the conductivity due to quantum interference effects, causing a change of sign in the slope of the conductivity with respect to the temperature of a metallic sample at low temperatures. The characteristic signature of this phenomenon is the suppression of these quantum effects on the application of a magnetic field. In Figure 5.1 is shown an example one of our macroscopic CVD graphene sample on borosilicate glass having a carrier concentration of $1.7 \times 10^{12} \text{ cm}^{-2}$. We see that the sample is metallic and that its resistance decreases with temperature ($\partial R_S / \partial T > 0$) till $\sim 80 \text{ K}$. Below 50 K the sample appears to be insulating as the resistance now increases as the temperature decreases. The behaviour in this specific case was shown to be weak localization in graphene.

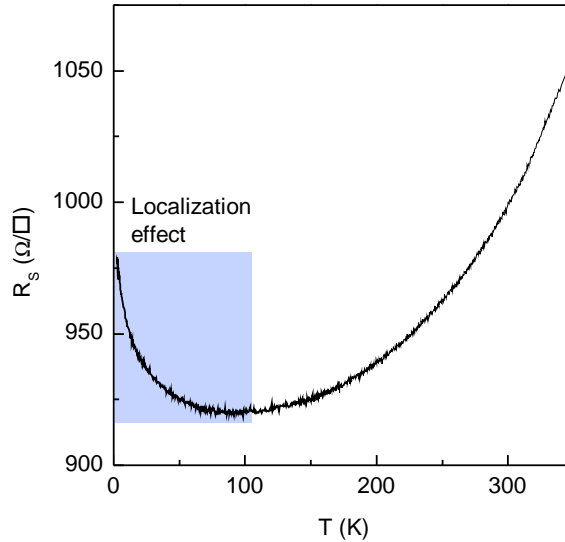


Figure 5.1: WL effect on the R_S vs T characteristic of a doped CVD graphene sample deposited on borosilicate glass.

5.1.1 Backscattering

In the classical treatment of the motion of a particle, an electron starting at the time $t = 0$ and position $\mathbf{r} = 0$ has a certain probability to be found at point \mathbf{r} , after a time $t \gg \tau$, with τ the transport relaxation time. A quantum mechanical treatment however results under certain conditions in an enhanced probability for the wavefunction at the starting point $\mathbf{r} = 0$ after a time t . Following the classical treatment, the probability w for the electron to travel from one point to another is given by the sum of the squares of the probability amplitudes A_i of all the possible paths connecting the two points, while in a quantum mechanical treatment where the wave function has a phase as well as an amplitude, it is the square of the sum of the probability amplitudes of all the possible paths [125]. In other words we have:

$$w = \begin{cases} \sum |A_i|^2, & \text{classical case} \\ |\sum A_i|^2, & \text{quantum mechanical case} \end{cases} \quad (5.1)$$

Since the possible paths an electron can travel are random, the phase acquired during a given path is also random. Most terms in the second row of Equation 5.1 thus cancel each other out. Paths travelled along opposite directions of a closed loop however will sum up. Thus in our simple model the probability of finding an electron at the starting point is increased by a factor of 2 with respect to the classical case:

$$w = \begin{cases} |A_1|^2 + |A_2|^2 = 2A^2, & \text{classical case} \\ |A_1|^2 + |A_2|^2 + 2|A_1A_2| = 4A^2, & \text{quantum mechanical case} \end{cases} \quad (5.2)$$

With A_1 and A_2 being the probability amplitudes that the electron travel along the same path in opposite direction and A is the modulus of A_1 and A_2 . This is the *Weak Localization* effect.

Figure 5.2 illustrates schematically the WL phenomenon. An electron, being subjected to various elastic scattering events can follow the path illustrated in Figure 5.2 by solid lines. As we saw from Equation 5.2, when we consider the phase of the electrons the times-reversed path (dashed lines) gives rise to a positive interference, thus making the closed loop the preferred path for the electrons and increasing the probability of finding it at the starting point.

The total effect is that the electron is backscattered *decreasing* the mobility of the charge carriers and, thus, provoking a negative correction to the conductivity.

5.1.2 Temperature dependence of the conductivity

At low temperature, the correction to the conductivity due to the weak localization effect is dependent on the dimensionality of the system. The

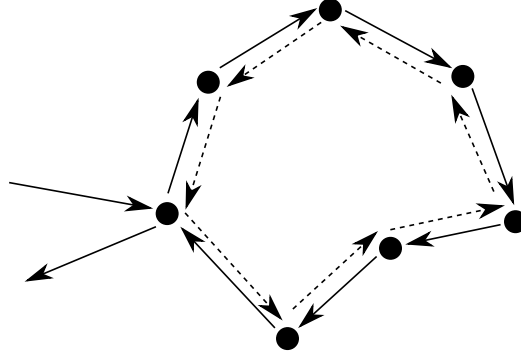


Figure 5.2: Illustration of the backscattering phenomenon by several scattering centers along opposite directions.

temperature dependence of the inelastic scattering time is $\tau_\phi \propto T^{-p}$, where p depends on the inelastic scattering mechanism. Thus from theoretical considerations the conductivity takes the form [126]:

$$\begin{aligned}
 \sigma(T)_{3D} &= \sigma_0 + \frac{e^2}{a\pi^2\hbar} T^{p/2} \\
 \sigma(T)_{2D} &= \sigma_0 + \frac{p}{2} \frac{e^2}{\pi^2\hbar} \ln\left(\frac{T}{T_0}\right) \\
 \sigma(T)_{1D} &= \sigma_0 - \frac{ae^2}{\pi\hbar} T^{-p/2}
 \end{aligned} \tag{5.3}$$

In our doped ZnO samples the temperature dependence of the conductivity is clearly representative of 2D transport. From the 2D case in Equation 5.3, plotting the conductivity with respect to the $\ln(T)$ should give a straight line. As a representative case of what is measured in our samples we show the behaviour of sample B at high doping ($n_S = 2.2 \times 10^{14} \text{ cm}^{-2}$) and at low temperature in Figure 5.3. A linear dependence is observed indicating the 2D nature of our samples. We now have clearer experimental verification of this 2D behaviour as opposed to the more ambiguous results shown in Figure 4.15.

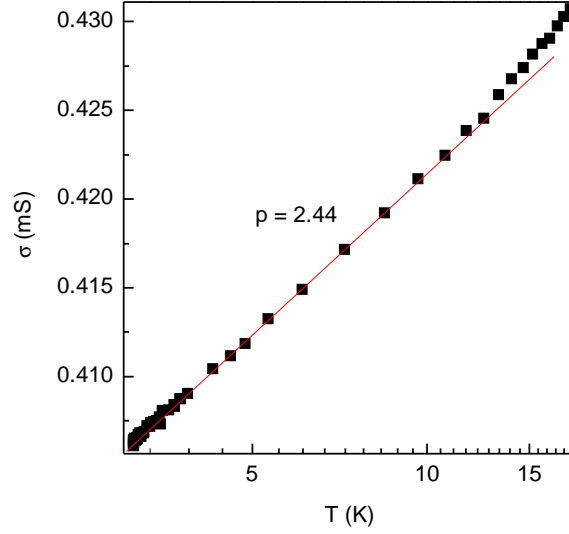


Figure 5.3: Conductivity of sample B at high doping as a function of $\ln(T)$. The linear behaviour is indicative of 2D transport for the electrons in the sample.

5.2 Magneto-conductivity

5.2.1 Theoretical considerations

Effect of the weak localization

Without quantum interference phenomena, *i.e.* for example at high temperature, conductivity has a quadratic dependence on the magnetic field [127]. However in two-dimensions, when quantum interference due to the weak localization takes place, the conductivity of the sample deviates from this value by a positive logarithmic value [126]. As pointed-out before, localization is due to the constructive interference of the wavefunctions along the same closed path in opposite directions. These will be in phase at the starting point of the closed loop and interfere constructively, increasing the probability of a carrier to ‘stay in the same place’ or localize. The application of a magnetic field B perpendicular to the current flux introduces a dephasing term $\delta\phi = 2\pi BS/\Phi_0$, where S is the surface of the closed loop and Φ_0 is the flux quantum. At low B , the dephasing is small and the quantum interference is still strong. But as B increases the constructive interference becomes smaller due to the increasing dephasing. This results in a reduction of the resistivity as a function of the magnetic field or *negative magnetoresistance*, which is a signature of weak localization. The rigorous expression for the correction to the conductivity coming from theoretical treatment can be found in Reference [128]

$$\frac{\Delta\sigma(B)}{G_0} = -\Psi\left(\frac{1}{2} + \frac{B_{tr}}{B}\right) + \Psi\left(\frac{1}{2} + \frac{B_\phi}{B}\right) \quad (5.4)$$

where Ψ is the digamma function, $G_0 = e^2/2\pi^2\hbar$ is the conductance quantum, $B_{tr} = \hbar/4eD\tau$ (τ is the scattering time associated to the mean free path L_{tr} and D is the diffusion coefficient), $B_\phi = \hbar/4eD\tau_\phi$ with τ_ϕ the inelastic scattering time. $\Delta\sigma(B)$ is the correction to the conductivity due to the interference phenomenon and is related to the magneto-conductivity by the expression $\Delta\sigma(B) - \Delta\sigma(0) = \sigma(B) - \sigma(0)$, where $\Delta\sigma(0)$ and $\sigma(0)$ are respectively the correction to the conductivity and the conductivity at zero applied magnetic field. The scattering time τ associated to the mean free path can be considered as the elastic scattering time only at very low temperature and in the following discussion this consideration will be taken into account.

Influence of spin-orbit coupling on the magneto-conductivity

In a material with spin-orbit coupling, that is coupling between the spin and the momentum of the carrier, the above picture undergoes further change. The rotation of the spin along the paths in opposite directions of the closed loop is also opposite, introducing a dephasing which leads to *destructive* interference. Spin-orbit coupling can thus have a significant effect on the low temperature magneto-conductivity. Spin-flip scattering (or spin relaxation and spin-lattice relaxation) can be due to different mechanisms the most important of which are the Elliott-Yafet mechanism, the D'Yakonov-Perel' mechanism and the Rashba effect. They will all be discussed in details later in this chapter. As discussed above, in the presence of spin-orbit coupling, the temperature dependence of the conductivity is still subject to a quantum correction arising from the altering of the constructive interference at the starting point of the closed path. In this case the correction is still logarithmic but is now positive (rather than negative as in the case of weak localization) [125] and is a direct consequence of the fact that the spin-flip time is shorter than the inelastic scattering time, $\tau_{SO} \ll \tau_\phi$.

The expression of the magneto-conductivity is radically altered by spin-orbit coupling. The correction to the magneto-conductivity taking into account this additional correction has been examined by several authors. In the case of a perpendicular magnetic field Zeeman coupling can be neglected and a general expression is given for example in Reference [129]:

$$\frac{\Delta\sigma(B)}{G_0} = -\Psi\left(\frac{1}{2} + \frac{B_{tr}}{B}\right) + \frac{3}{2}\Psi\left(\frac{1}{2} + \frac{B_\phi + B_{SO}}{B}\right) - \frac{1}{2}\Psi\left(\frac{1}{2} + \frac{B_\phi}{B}\right) \quad (5.5)$$

where $B_{SO} = \hbar/4eD\tau_{SO}$ is the characteristic field associated with the spin-flip time.

Equation 5.5 then describes the behaviour of the magneto-conductivity in the presence of WAL. However though very general because all scattering processes are explicitly taken into account, the practical application of this expression to analyze experimental data can be hazardous because it

depends on as many as three parameters (B_{tr} , B_ϕ and B_{SO}). The mathematical problem thus can be overdetermined and the extraction of the three parameters unstable. Another problem that must be confronted is the need to estimate a diffusion coefficient to extract characteristic scattering times and lengths.

As a first step we used Equation 5.5 to fit our data. We could thus extract three characteristic fields but in some cases the characteristic field B_{tr} was found to be of the order of the applied magnetic field or B_ϕ or B_{SO} . This translates to a time τ associated to the mean free path of the order of τ_ϕ and τ_{SO} , which is questionable.

Another expression for the magneto-conductivity can be found in References [130, 131]:

$$\begin{aligned} \frac{\Delta\sigma(B)}{G_0} = & \Psi\left(\frac{1}{2} + \frac{B_\phi + B_{SO}}{B}\right) + \frac{1}{2}\Psi\left(\frac{1}{2} + \frac{B_\phi + 2B_{SO}}{B}\right) \\ & - \frac{1}{2}\Psi\left(\frac{1}{2} + \frac{B_\phi}{B}\right) - \ln\left(\frac{B_\phi + B_{SO}}{B}\right) \\ & - \frac{1}{2}\ln\left(\frac{B_\phi + B_{SO}}{B}\right) + \frac{1}{2}\ln\left(\frac{B_\phi}{B}\right) \end{aligned} \quad (5.6)$$

In this expression only two parameters, B_ϕ and B_{SO} appear, making their extraction from experimental data more stable. This reduction of the number of parameters is based on the hypothesis that the characteristic field B_{tr} is much higher than the applied magnetic field in the measurement. This translates to a time τ associated to the mean free path which is much smaller than τ_ϕ and τ_{SO} . τ can be estimated by the expression of the mobility (or conductivity) in terms of τ and the effective mass of the charge carriers in ZnO $m_{eff} = 0.25$ obtained from Reference [132]:

$$\tau = \frac{\mu m}{e}. \quad (5.7)$$

As we shall see later the condition $\tau \ll \tau_\phi, \tau_{SO}$ is indeed satisfied.

This brings us to the problem of the extraction of these characteristic times from experimental data. An expression for a diffusion coefficient is needed. One can be tempted to use the Einstein relation ($D = \mu k_B T / e$, with μ the mobility of the charge carriers, k_B the Boltzmann constant, T the temperature and e the electron charge), but in our case a more appropriate expression is $D = v_F^2 \tau / 2$ [125], with v_F being the Fermi velocity which is estimated in the approximation of a perfect two-dimensional electron gas and a single parabolic conduction band. In this case, $v_F = \hbar k_F / m$ where \hbar is the reduced Planck constant and $k_F = \sqrt{8\pi n_S}$ is the Fermi wavevector and n_S the carrier concentration.

5.2.2 Magneto-conductivity of ZnO

We measure the magneto-conductivity of our ZnO thin films as a function of temperature and doping. The range of doping is the one shown in Figure 4.10 *i.e.* from $\sim 10^{13}$ to over 2×10^{14} cm^{-2} while the measurements under magnetic field are usually carried out at 50, 25, 10 and 4 K. Our electromagnet facility allows us to apply a magnetic field of up to 2 T. The 2 T field is sufficient to observe significant changes in magnetoconductivity.

Given the small spin-orbit coupling in ZnO one could ask if weak anti-localization would be visible in our samples. We show that in a certain domain of doping, temperature and magnetic field we do observe weak anti-localization. More interestingly in all our samples we observe a transition from weak localization to weak anti-localization. This transition can be observed at fixed carrier concentration as temperature decreases, or at fixed temperature by lowering the carrier concentration. This transition is a textbook case of a change in the dominant scattering mechanism as a function of an external parameter.

WL to WAL transition as a function of temperature

Let us examine the correction to the magneto-conductivity $\Delta\sigma(B)/G_0$ calculated in Equation 5.6 for our data. For clarity we restrict ourselves to data from sample C but as we have mentioned before, all our samples show similar behaviour. In Figure 5.4 is shown the relative variation of the magneto-resistance and its evolution in temperature in the range 4 K to 50 K while in Figure 5.5 we show the calculated $\Delta\sigma(B)/G_0$. The carrier concentration of the sample which stays fixed throughout this measurement is measured at room temperature to be 7.2×10^{13} cm^{-2} . In the figure, the grey circles correspond to the correction to the conductivity calculated from $\Delta\sigma(B)/G_0 = (\sigma(B) - \sigma(0))/G_0$ and the coloured lines are the parametrized fits obtained from Equation 5.6. The parameters are the characteristic fields B_ϕ and B_{SO} .

A deviation from zero in this figure indicates a modification of the conductivity in presence of the magnetic field due to the WL or WAL phenomena. Even at the relatively high temperature of 50 K we detect weak localization: the conductivity *increases* with the magnetic field. Since the inelastic scattering time increases with decreasing temperature weak localization increases between 50 and 10 K. However at 4 K the correction $\Delta\sigma(B)/G_0$ to the conductivity switches sign becoming negative. This is the signature of weak anti-localization and implies that the spin relaxation time τ_{SO} is now lower than τ_ϕ . This is the crossover between dominating scattering mechanisms that we mentioned above, which is controlled by temperature. It can be seen from the figure that the parametrized fits are of good quality and permit us to extract characteristic parameters of the scattering experienced

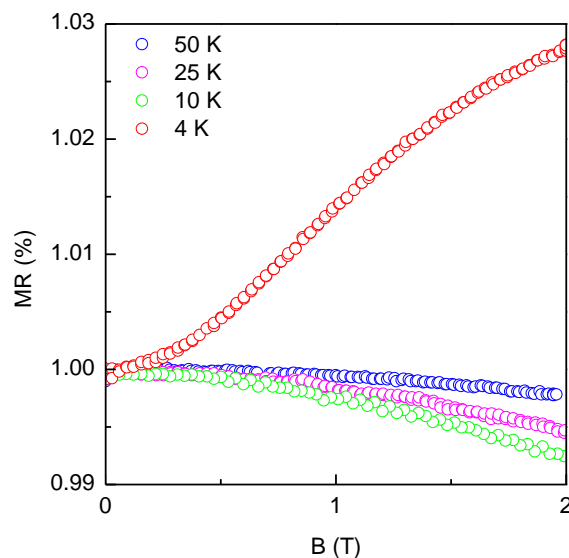


Figure 5.4: Normalized magneto-resistance ($R_S(B)/R_S(0)$) as a function of the temperature showing the relative variation of the resistance of the sample with the magnetic field.

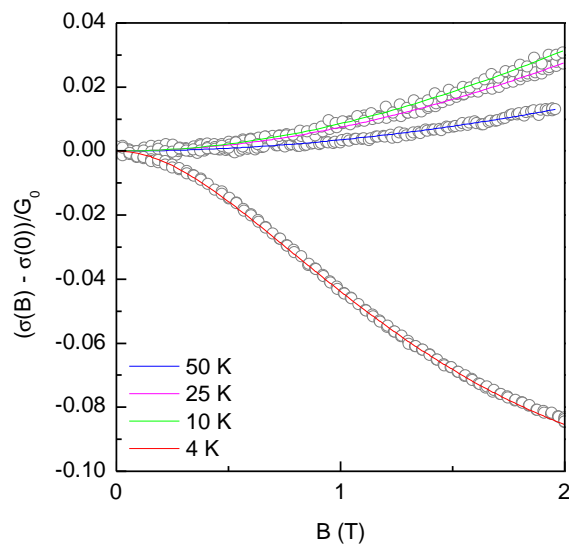


Figure 5.5: Correction to the magneto-conductivity of sample C at a carrier concentration of $7.2 \times 10^{13} \text{ cm}^{-2}$. The grey circles are the calculated data of the correction of the conductivity from the measured data of magneto-resistance while the coloured lines are the fit obtained from software analysis using Equation 5.6 and using as the characteristic fields B_ϕ and B_{SO} as fitting parameters. We observe a transition from weak localization to Weak Anti-Localization occurring between 10 and 4 K.

by the carriers in each case, notably the characteristic fields which are related to the characteristic transport times τ_ϕ and τ_{SO} , while τ is estimated from Equation 5.7. We are confident that the positive magnetoresistance ob-

served in our measurements is effectively due to the WAL effect and not to the classical magnetoresistance due to the Kohler effect which manifest itself as a quadratic dependence of the resistivity as a function of the magnetic field. In the first place, the Kohler effect is relevant when the charge carriers in the material have relatively high mobility, which is not the case of our ZnO samples. Secondly, the Kohler effect is visible at very high magnetic field, which again is not our case since we are able to apply a magnetic field of maximum 2 T. Classical magnetoresistance is proportional to $1 + (\mu \times B)^2$ [133] so for $\mu = 5 \text{ cm}^2\text{V}^{-1}\text{s}^{-1}$ and $B = 2 \text{ T}$, we get $10^{-6}\%$ which is four orders of magnitude smaller than what we see.

We use Equation 5.6 to fit our data as it allows for a comprehensive description of the magneto-conductivity and can be used to extract the necessary information required for the understanding of the scattering mechanisms in the samples. Other alternatives are proposed in literature to describe the magneto-conductivity in the presence of quantum interference phenomenons like in References [72, 104, 134] where an approximation of Equation 5.5 is used. In the equation for the correction $\Delta\sigma(B)/G_0$ used in those works the only fitting parameters is the inelastic scattering time τ_ϕ (thus neglecting the spin relaxation time τ_{SO}) and the phenomenon of the weak anti-localization in Reference [134] is not treated in terms of τ_{SO} but a negative prefactor is simply added in order to change the sign of the curve. In Reference [77] instead a semiempirical expression is used in order to fit the negative magneto-resistance data.

In Figure 5.6 are shown B_ϕ and B_{SO} obtained from the fits of Figure 5.5. As expected, B_ϕ decreases with the temperature ($B_\phi \propto 1/\tau_\phi \propto T^p$). B_{SO} does not vary with T except at the lowest measured temperature at 4 K where B_{SO} becomes larger than B_ϕ . This transition manifests itself as the weak anti-localization effect.

The process of fitting the data with Equation 5.6 must be done with care since the values of the two parameters are dependent on each other. Several pairs of valid values can be found which gives a domain of validity for each parameter. Thus several alternative sets of parameters were tried to establish the domain of existence of the fits which determine the error bars shown in Figure 5.6. By software analysis, after the initial parameters are fitted with the least square method and the unphysical values are discarded, the parameters are varied in order to find the range in which the fit is still valid. We are thus confident of the values extracted by this procedure and the interpretation that we deduce from them.

The characteristic fields extracted from the fits can be translated into a more physically intuitive quantity by using the diffusion coefficient D discussed above. Indeed the fields are related to characteristic relaxation times (see Equation 5.4, Equation 5.5 and Equation 5.6) which we now show in Figure 5.7. The values of τ_ϕ and τ_{SO} are estimated using the *highest* values of the fields estimated in domain represented by the error bars of

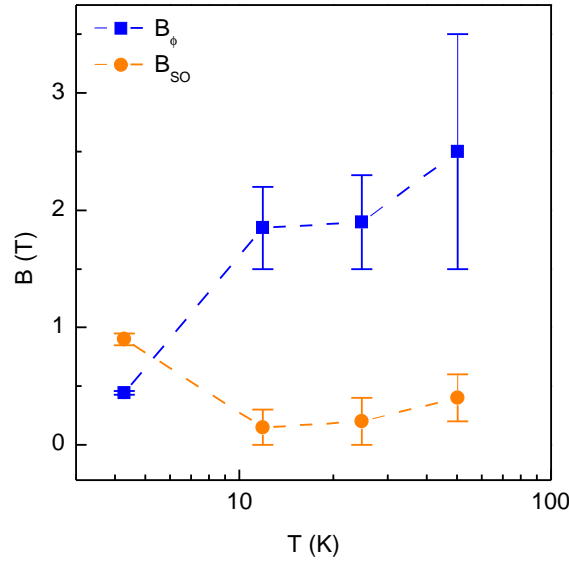


Figure 5.6: Evolution of the characteristic fields associated with the curves of Figure 5.5. Till 10 K, B_ϕ is higher than B_{SO} , as a consequence of the shorter inelastic scattering time with respect to the spin-flip time. Between 10 and 4 K we observe a crossover and the weak anti-localization takes place.

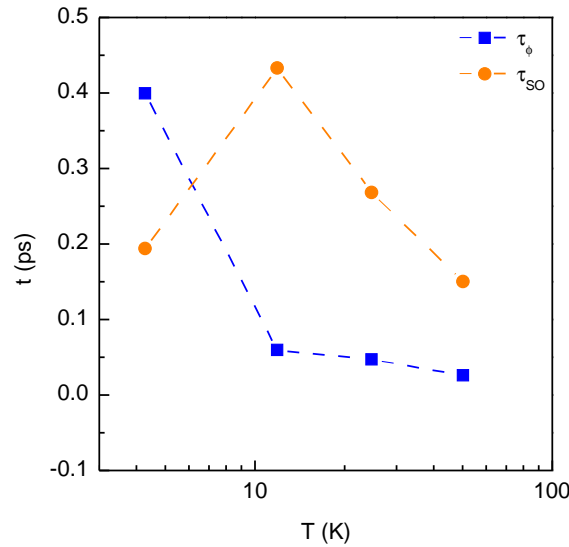


Figure 5.7: Inelastic scattering time and spin relaxation time as a function of the temperature calculated from the curves of Figure 5.5. A crossover can be observed between 10 and 4 K, such that at the lowest temperatures the spin relaxation time becomes shorter than the inelastic scattering time.

Figure 5.6. No error bars are consequently shown for these characteristic times. Corresponding to the behaviour already seen for the characteristic fields, while at higher temperature τ_ϕ is always smaller than τ_{SO} , there is

| Sample | $n_{S,4\text{ K}}$ (10^{14} cm^{-2}) | τ_{SO} (ps) |
|--------|---|------------------|
| A | 1.37 | 0.76 |
| B | 2.06 | 0.52 |
| C | 1.39 | 0.53 |
| D | 1.56 | 1.62 |

Table 5.1: Maximum spin relaxation time found in the measured samples in high doping conditions.

a crossover as T approaches 4 K where the spin relaxation time becomes smaller than the inelastic scattering time.

The values found for the different samples at 4 K and at high doping (*i.e.* where the spin relaxation is supposed to be slower) are listed in Table 5.1. We find values value of $\tau_{SO} \approx 0.5 - 1.6$ ps at 4 K in our samples. These are only indicative but consistently smaller than those found in earlier works. Ghosh *et al.* [124] measure electron spin dynamics in 100 nm thick epilayer samples with Time Resolved Faraday Rotation. Prestgard *et al.* [120] measure spin relaxation times with spin polarized Hanle transport measurements in 200 nm thick films. The carrier concentrations in their highest doped samples when translated to our 2D case are well below those that we achieve. Ghosh *et al.* measure a spin relaxation time of 2 ns at 10 K rapidly decreasing with temperature. Prestgard *et al.* measure a spin relaxation time of 0.15 ns at 20 K. Finally Liu *et al.* [123] report a theoretical estimation of about 6 ns for ZnO. The values we found for τ_{SO} at low temperature and high doping in our samples are smaller than what are found in literature and could be attributed to the relatively low mobility in our polycrystalline samples compared to the other published works.

WL to WAL transition as a function of carrier concentration

The transition from weak localization to weak anti-localization can also be observed at a fixed temperature (4 K) by varying the carrier concentration as shown in Figure 5.8 for samples B and C. They are representative of all our samples where we systematically measure this transition from WL to WAL. Figure 5.9 shows the magneto-resistance corresponding to the curves in presented Figure 5.8 and normalized to the value of R_S at $B = 0$. We note the following points:

- the phenomenon we observe of increasing magneto-resistance (decreasing magneto-conductivity) is unambiguously associated to the weak anti-localization and not to the normal parabolic increase of the resistivity with the magnetic field because the latter is a phenomenon observable at higher values of B .

- weak anti-localization is present at relatively low carrier density, meaning that in this range of doping and at 4 K the spin relaxation time is shorter than the inelastic scattering time;
- τ_ϕ becomes smaller than τ_{SO} as n_S approaches 10^{14} cm^{-2} and the transition to weak localization occurs (Figure 5.10); in other words B_{SO} decreases with increasing doping;
- the discussion above is valid only if the B_{tr} , the characteristic field associated with the mean free path, is much larger than B_ϕ and B_{SO} , which is the assumption implicitly made in Equation 5.6. In fact, the parameter B_{tr} would appear in the equation if it would be comparable to the other characteristic fields (like in Equation 5.5 for example),

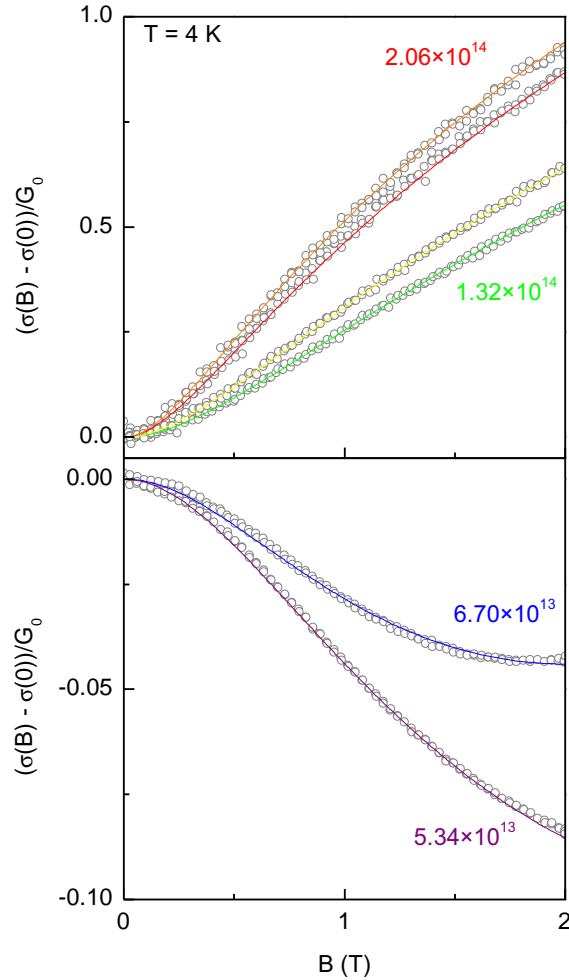


Figure 5.8: Combined data from sample B and C showing the transition from weak anti-localization to weak localization as n_S increases. The data from the two samples show perfect coherence.

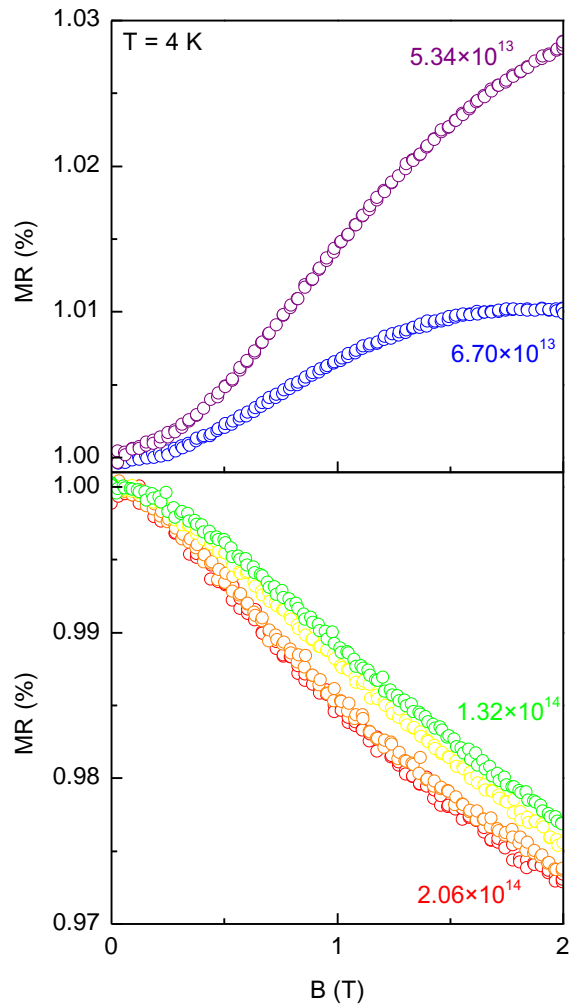


Figure 5.9: Combined magneto-resistances corresponding to the calculated corrections of magneto-conductivity shown in Figure 5.8.

but one obtains the actual expression of Equation 5.6 by considering B_{tr} much higher than the maximum applied magnetic field. Intuitively this translates the logical fact that the mean free path, which is related to the totality of scattering events, is smaller than the characteristic lengths associated to specific scattering events: inelastic or spin-flip scattering. Typical values obtained for τ corresponding to the mean free path are of the order of 10^{-15} s indicating once more that defect scattering is important.

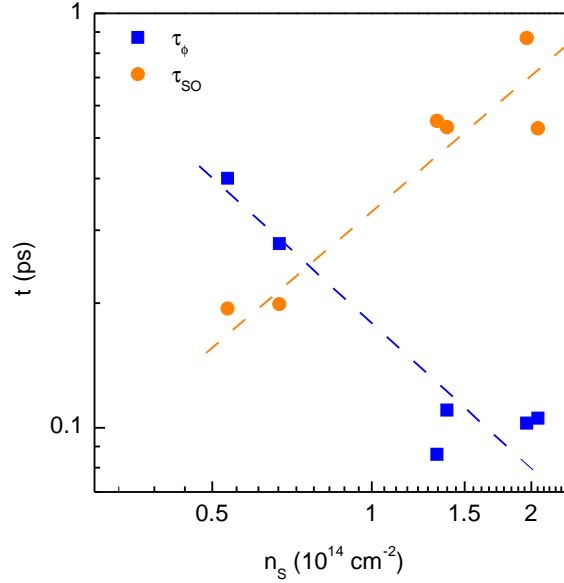


Figure 5.10: τ_{phi} and τ_{SO} as a function of n_s extracted from the fit of Figure 5.8.

Considerations on the characteristic transport lengths

From the characteristic fields obtained from the fit of the correction of the magneto-conductivity with Equation 5.6 it is possible to obtain the values of the phase-coherence length L_ϕ and the spin-coherence length L_{SO} . Since $L = \sqrt{D\tau}$, with D the diffusion coefficient and τ the characteristic transport times associated with L , we can estimate the characteristic transport lengths from

$$L = \sqrt{\frac{\hbar}{4eB}} \quad (5.8)$$

with L being L_ϕ or L_{SO} and B respectively B_ϕ or B_{SO} . The mean free path L_{tr} is derived from τ by the expression $L_{tr} = v_F\tau$, with v_F being the Fermi velocity.

The mean free path at 4 K calculated for the four analyzed samples ranges from ~ 1 nm at the lowest carrier concentration to ~ 6 nm at the highest carrier concentration. The increase of L_{tr} with the doping is due to the increasing overlap of the wavefunctions of the electrons in the material as the carrier concentration increases. As we saw in Section 4.3 the charge carriers are subjected to VRH especially at low carrier density well in the insulating regime. We notice also that at high carrier density where the maximum value of L_{tr} is attained, it is of the order of the lowest dimension of the grain-size. This is the thickness of the disk shaped grains (Section 4.1.2). This is to be expected because the mean free path cannot be longer than this minimum dimension of the crystalline grain.

The calculated phase-coherence lengths vary from 16 nm to 49 nm at 4 K

in going from low to high carrier concentrations. These values are higher than those of L_{tr} and most importantly at high carrier concentration they are bigger than the minimum dimension of the crystalline grain. This fact is coherent with the observation of WL and WAL. In fact the charge carriers need to remain inside a single crystal grain of the polycrystalline film to maintain phase coherence. The only way to maintain phase coherence for such a long path (50 nm) is to travel along a loop inside the same grain which is possible given the flat disk-like shape of the grains (Section 4.1.2) and the average diameter of about 30 nm. We could thus imagine that the situation depicted in Figure 5.2 to explain the WL effect actually happens inside one of the grains of the sample.

The values obtained for the spin-coherence length L_{SO} at 4 K vary from 10 nm to 128 nm. It is found in the regime of the WL that, as expected, L_{SO} is bigger than L_ϕ meaning that the electrons travel for a distance L_ϕ with the same phase but the spin is preserved until the distance L_{SO} is reached, inelastic scattering dominates. On the other hand, the value of L_{SO} is found to be smaller than L_ϕ when we observe the WAL, or in other words in this regime spin-flip scattering dominates.

5.3 Origin of the spin-orbit coupling

As mentioned above, spin-orbit coupling in semiconductors can originate from various mechanisms. Below we discuss the various possibilities briefly and from our data we isolate the dominant mechanism in our samples. The possibilities considered are the D'Yakonov-Perel' mechanism, the Rashba effect and the Elliott-Yafet mechanism.

5.3.1 D'Yakonov-Perel' mechanism

The D'Yakonov-Perel' mechanism is an efficient spin-relaxation mechanism in systems lacking an inversion symmetry resulting in an effective magnetic field. Indeed, without inversion symmetry, the spin-up and spin-down states are not degenerate: $E_{\mathbf{k}\uparrow} \neq E_{\mathbf{k}\downarrow}$ [135]. The conduction band states experience ordinary impurity and phonon scattering. The wavevector \mathbf{k} changes at every scattering event, as well as the effective magnetic field on the spin that comes from the spin-orbit coupling. The fluctuating magnetic field is responsible for the spin relaxation and its magnitude is proportional to the conduction-band spin splitting. The D'Yakonov-Perel' mechanism can be recognized to be active in the material if there is direct correlation between the inverse of the spin relaxation time τ_{SO} and the time associated to the mean free path τ [135]:

$$\frac{1}{\tau_{SO}} \propto \tau \quad (5.9)$$

In Figure 5.11 we show the plot of $1/\tau_{SO}$ vs τ for all samples analyzed and for different carrier concentrations. It can clearly be seen that the quan-

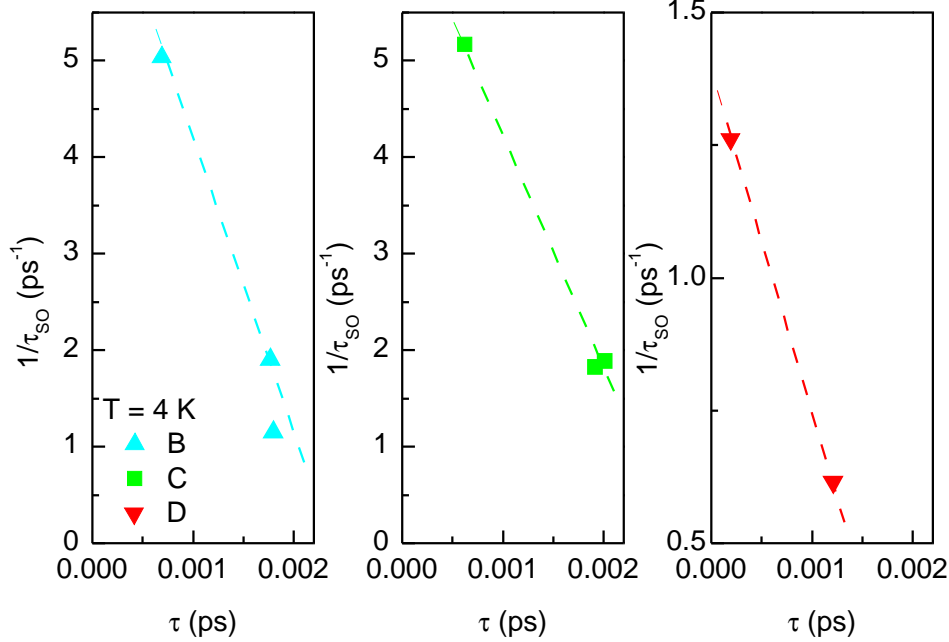


Figure 5.11: Plot of $1/\tau_{SO}$ with respect of τ clearly showing that the D'Yakonov-Perel' mechanisms is not active in our samples.

tity $1/\tau_{SO}$ is inversely and not directly correlated to τ and we can conclude that in our samples the D'Yakonov-Perel' mechanism is not the dominant mechanism for spin relaxation. Earlier published works used spin polarized transport Hanle experiments or optical orientation experiments [120, 122] to measure spin relaxation in ZnO. They identified the D'Yakonov-Perel' mechanism as the dominant mechanism, arguing that the conditions in ZnO (large band gap and small spin-orbit coupling) were compatible with it. Some differences exist between these experiments and our experiment in that they used samples with a very high degree of crystallinity and a thickness above 100 nm. However the main difference resides in the fact that our carrier concentrations are clearly higher than the ones in their samples. Secondly as shown by [122], the D'Yakonov-Perel' mechanism becomes dominant above 50 K while all our measurements pertain to temperatures below 50 K.

5.3.2 Rashba effect

The Rashba effect can be classified as a particular case of the D'Yakonov-Perel' mechanism. In a two-dimensional electron gas (2DEG) formed in an interfacial band bending of a semiconductor when the spin-orbit coupling is governed by the Rashba effect, a supplemental term is added to the Hamil-

tonian:

$$H_{SO} = \alpha(\sigma \times \vec{k}) \cdot \vec{n}_z \quad (5.10)$$

where σ are the Pauli matrices, \vec{k} is the quasi-wavevector of the electrons, \vec{n}_z is a unit vector perpendicular to the surface and α is the spin-orbit coupling constant [136] which is proportional to the electric field perpendicular to the 2DEG. The spin relaxation time is related to the spin-orbit coupling constant by the relation $1/\tau_{SO} \propto \alpha^2$.

It is reasonable to think that the Rashba effect can be present in the doped ZnO thin-films since the doping is electrostatically induced by the ions accumulated at the interface between the glass and the zinc oxide. In this particular case, the carrier density at the interface is proportional to the perpendicular electric field seen by the electrons, and hence, if the Rashba effect is active, we should see an increase in spin orbit scattering with increasing carrier density. However, we can exclude that this is the dominant effect since we can see from Figure 5.12 that B_{SO} (which is proportional to $1/\tau_{SO}$) decreases with increasing carrier concentration which is the opposite of the behaviour expected from the Rashba effect.

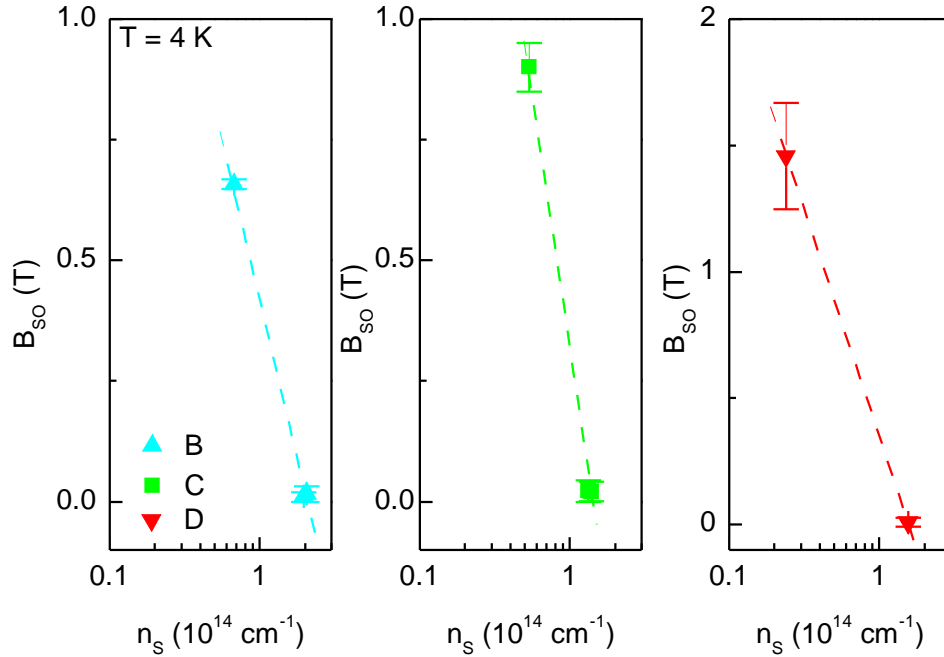


Figure 5.12: Evolution of B_{SO} as a function of the carrier density.

5.3.3 Elliott-Yafet mechanism

In the Elliott-Yafet mechanism spin relaxation is caused by scattering with the ions of the lattice or impurities at low temperature or phonons at high

temperature. At every scattering event there is a finite probability that the electron changes its spin orientation. It is thus reasonable to think that this mechanism is active in our ZnO thin films since oxygen vacancies (present in our samples) represent an important source of scattering.

From the rigorous treatment of the problem of the electrons travelling in a crystal in the presence of spin-orbit coupling [135, 137], one finds that the Hamiltonian describing the system has a component resulting from the spin-orbit coupling and the corresponding eigenfunctions will be a linear combination of spin-up \uparrow and spin-down \downarrow states

$$\begin{aligned}\Psi_{\mathbf{k}n\uparrow}(\mathbf{r}) &= [a_{\mathbf{k}n}(\mathbf{r})|\uparrow\rangle + b_{\mathbf{k}n}(\mathbf{r})|\downarrow\rangle] e^{i\mathbf{k}\cdot\mathbf{r}} \\ \Psi_{\mathbf{k}n\downarrow}(\mathbf{r}) &= [a_{-\mathbf{k}n}^*(\mathbf{r})|\downarrow\rangle - b_{-\mathbf{k}n}^*(\mathbf{r})|\uparrow\rangle] e^{i\mathbf{k}\cdot\mathbf{r}}\end{aligned}\quad (5.11)$$

The two functions are degenerate (same \mathbf{k} and energy) and are coupled by time reversal and spatial inversion. In other words, the Equations 5.11 describe a mixing of spin-up and spin-down states. Since spin mixing is usually small, we can assume that in Equations 5.11 $|a| \approx 1$ and $|b| \ll 1$. In the presence of such mixing of the eigenfunctions, the spin relaxation can be caused by any spin-independent event, while (in principle) in the absence of scattering the spin of the electrons remains unaltered. The Elliott-Yafet process is schematically shown in Figure 5.13.

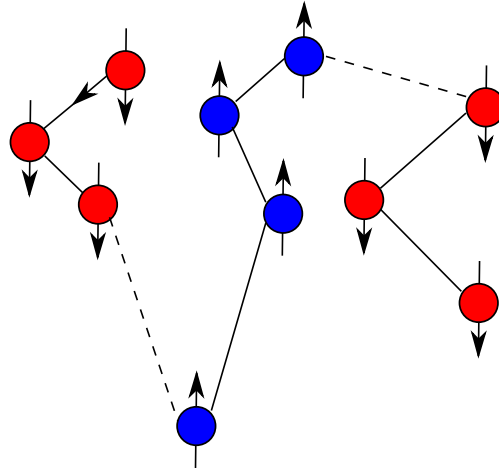


Figure 5.13: Illustration of the Elliott-Yafet mechanism showing that the spin of the electron can change during a scattering event. The electron possessing for example spin down (red circles) undergoes some scattering events until one of them causes a spin change (blue circles). This phenomenon is repeated after some collisions.

Since spin relaxation can occur only during a momentum scattering event, the spin relaxation time is related to the mean free path time by

a relation of proportionality [137]

$$\tau_{SO} \propto \tau. \quad (5.12)$$

Theoretically, the ratio τ/τ_{SO} (according to the Elliott relation [135]) should be equal to the shift Δg of the electronic g factor from the free electron value $g_0 = 2.0023$ [137]. However, experimentally the ratio τ/τ_{SO} also depends on the scattering source (impurities, grain boundaries or phonons).

To examine if the Elliott-Yafet mechanism is dominant in the experimental conditions of our samples we plot τ_{SO} as a function of τ . The plots for samples B, C and D are shown in Figure 5.14. The proportionality indicates

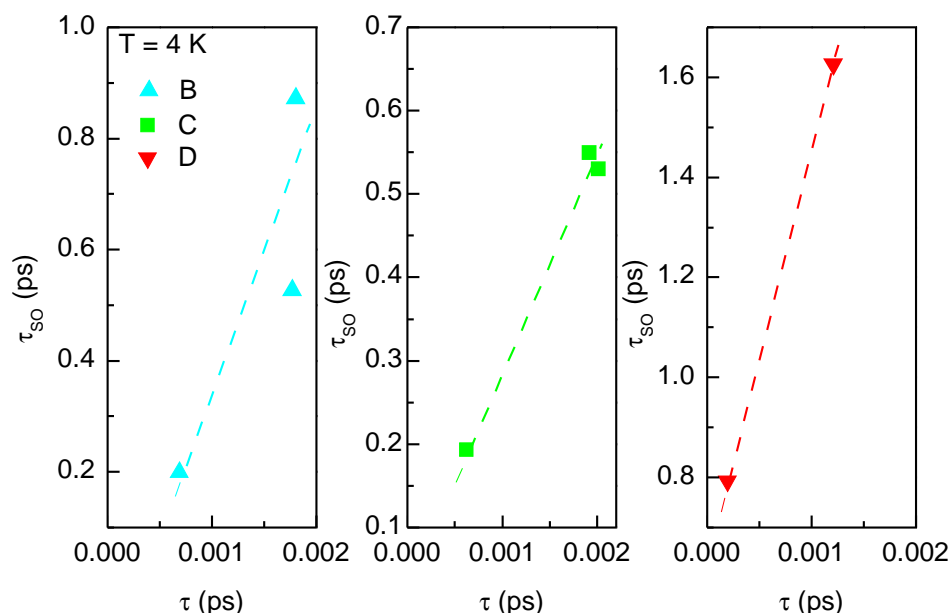


Figure 5.14: τ_{SO} vs τ for samples B, C and D at different electron concentrations. The proportional relationship seen confirms that the Elliott-Yafet mechanism is the dominant mechanism encountered.

dominance of the Elliott-Yafet mechanism. As there are no foreign atoms in our ZnO samples, the only scatterers which can be responsible for the spin relaxation are the oxygen vacancies. This is also in agreement with the discussion in Chapter 4.

5.4 Considerations on the metal-insulator transition

One could determine the transition from the insulating to the metallic state through what is called the Ioffe-Regel criterion [138]. According to this criterion the metal-insulator transition is marked by a critical carrier density

n_c for which the product $k_F l_{tr} = 1$, with k_F being the Fermi wavevector and l_{tr} the mean free path. If $k_F l_{tr} > 1$, the system is in the metallic state, while the system is insulating when $k_F l_{tr} < 1$.

We calculated the product $k_F l_{tr}$ for all our samples in order to determine if the sample could be considered a “metal” at high doping and an insulator at low doping according to the Ioffe-Regel criterion. For high doping, *i.e.* $n_S > 10^{14} \text{ cm}^{-2}$, we always obtain $k_F l_{tr} \gg 1$, with values varying between 21 and 42. At lower doping ($2.4 - 6.3 \times 10^{13} \text{ cm}^{-2}$) $k_F l_{tr}$ is of the order of unity, ranging between 0.5 and 5.4. This criterion indeed corresponds to such a transition in certain cases [139]. In our case at low doping the R_S vs T curves have a clear negative slope indicating that the sample is insulating (see Figure 4.10) even though the product $k_F l_{tr}$ is of the order of unity. In the high carrier density regime, where $k_F l_{tr} \gg 1$, we still observe non-metallic behaviour in our samples in the sense that $\partial R_S / \partial T < 0$.

The Ioffe-Regel criterion has been used to argue that the metal-insulator transition was achieved in polycrystalline ZnO with chemical doping [107]. Though the product $k_F l_{tr}$ becomes larger than unity as doping is increased, similar to our observations, the commonplace metallic criterion of $\partial \rho / \partial T > 0$ is not observed in the ρ vs T curves. To clarify the semantic aspects, our highly doped samples are thus metallic from the point of view of the Ioffe-Regel criterion but not from the point of view of the $\partial \rho / \partial T > 0$ criterion.

5.5 Conclusions of the magneto-transport in ZnO

This chapter was dedicated to the study of the magneto-transport properties of our doped non-stoichiometric ultra-thin ZnO samples deposited on soda-lime glass. Magneto-transport measurements revealed the scattering mechanisms active in our doped thin-films and helped determine the origin of the spin-flip observed in the samples. Many groups have studied spin relaxation in ZnO with the perspective of the use of ZnO in spintronics applications.

We observe the phenomenon of the weak localization associated to quantum interference and disorder in the sample. We also systematically observe at low temperature and at a certain carrier concentration a transition to the weak anti-localization meaning that the spin relaxation time τ_{SO} has become shorter than τ_ϕ .

The characteristic transport times are determined by a parametric fit of the correction of the magneto-conductivity curves using the equation found in [130, 131] (Equation 5.6) which is the result of the rigorous treatment of the problem of the magneto-transport in the presence of spin-orbit coupling. We have thus given a complete description of magneto-conductivity in polycrystalline ZnO when compared with other reports in literature.

The analysis of the evolution of the characteristic scattering times al-

lowed to identify the Elliot-Yafet mechanism to be responsible for the spin relaxation. In the presence of this mechanism there is a finite probability that the spin of the electrons can be reversed after a scattering event and the evidence that the Elliot-Yafet mechanism is active in our samples is in the linear relation between the scattering time τ which is essentially elastic at low temperatures and the spin relaxation time τ_{SO} . Another work cites the D'Yakonov-Perel' mechanism as the most important spin relaxation mechanism in ZnO, but as we have pointed out before their experimental conditions (carrier concentration and measurement temperature) are different.

The transition from WL to WAL can be also obtained at a certain temperature by decreasing the carrier concentration in our samples. At 4 K we observe a crossover as n_S approaches 10^{14} cm^{-2} from WAL to WL, meaning that below 10^{14} cm^{-2} the spin relaxation time is shorter than the inelastic scattering time ($\tau_{SO} < \tau_\phi$). We can thus tune the dominant scattering mechanism in our samples by changing the carrier density.

Concluding, we showed the relevance and efficiency of the space charge doping technique for polycrystalline thin films of a wide band gap semiconductor, ZnO. We could observe quantum interference phenomena in the low temperature magnetoconductivity of these films and extract characteristic values related to the scattering mechanisms. These are compatible with the crystalline structure and electronic properties of ZnO and were compared to recent literature. Finally we also showed that the dominant scattering mechanism can be tuned by external parameters like temperature but also, in our case an electrostatic field which changes carrier concentration.

Chapter 6

Conclusions and perspectives

In this thesis we have developed a new technique for ultra-high electrostatic doping of thin films of materials deposited on a glass substrate called *Space Charge Doping*. We have applied this technique to the prototype 2D material graphene which is a semi-metal and can easily be prepared in a monolayer. We have also applied this technique to polycrystalline films of the wide band gap semiconductor zinc oxide. We have successfully obtained carrier concentration levels beyond 10^{14} cm^{-2} in both materials in a reversible way. Reaching a high carrier concentration in these materials is of interest for a wide variety of reasons, a common one being the eventual application as a transparent conducting electrode. We applied our method to obtain very significant modification of carrier density and modification of the transport properties investigated as a function of temperature and magnetic field. The techniques and the results obtained were discussed in the light of material properties and the relevant theory.

Space charge doping has been shown to be a powerful and reliable method for doping materials deposited on a glass substrate, capable of inducing extremely high doping levels in a reversible way. Moreover, the doping level can be finely controlled allowing to study the properties of the materials in a wide range of doping without introducing defects. The space charge created at the glass surface with the sodium ions accumulation or depletion is able not only to dope two-dimensional materials like graphene, but also polycrystalline materials like ZnO. This fact opens a completely new perspective in many fields, going from the fundamental research to industrial applications.

The first experiments on space charge doping were performed on microscopic and macroscopic graphene samples. The fact that it is possible to dope graphene *n* or *p* makes it the ideal material for the characterization of our doping technique, both from a fundamental and from an applied point of view. We showed that with the space charge at the glass/graphene

interface it is possible to reproduce the well known bell-shaped R_S vs n_S characteristic of graphene demonstrating that the space charge doping can finely control the doping level in graphene. Moreover, the doping is reversible and doesn't introduce defects, as shown from Raman spectroscopy. The maximum reached doping level depends on the material and on the glass substrate and is higher for glasses containing a higher concentration of Na^+ ions. The maximum doping we reached is $1.2 \times 10^{14} \text{ cm}^{-2}$ in the electron side. The technique was also validated for large area CVD graphene samples ($\sim 1 \text{ cm}^2$), indicating that the doping process is uniform all over the glass surface.

For practical applications like TCE other important parameters are the minimum value of sheet resistance and the transparency of the material. Both the quality of the graphene sample and the glass surface play a role. In fact, the smoother the surface of the glass the higher the mobility of charge carriers in graphene and the lower the sheet resistance with a minimum measured value of R_S of $224 \Omega/\square$ on borosilicate glass. The transparency of the space charge doped graphene is also unaltered, as a further confirmation that the quality of the sample is preserved.

Space charge doping has thus been demonstrated to be a very efficient doping method for graphene and easily extensible to other two-dimensional materials. In the field of transparent conductors, the combination of graphene and space charge doping can be a valid alternative to the already used materials and doping techniques in this field. However, monolayer graphene is sensitive to air pollution especially when it is highly doped. Thus it requires packaging or it needs to be kept in vacuum. Other alternatives like transparent oxides combined with the space charge doping can be the answer for finding new transparent conductors.

The measurements performed on ultra-thin ($< 40 \text{ nm}$) films of ZnO_{1-x} were essential to expand the applicability of space charge doping to polycrystalline materials. Also, electrostatically doped ultra-thin ZnO could have potential applications as a TCE. We showed that space charge doping is able to induce a very high carrier density in ZnO with sheet resistance dropping from $\sim 10^8 \Omega/\square$ to $\sim 10^3 \Omega/\square$, a difference of 5 orders of magnitude. The maximum doping level attained was $2.2 \times 10^{14} \text{ cm}^{-2}$. Like in the case of graphene, the doping level can be finely controlled in the accumulation layer at the interface allowing us to study the electronic properties of the thin-film in wide range of carrier concentrations. The analysis of the Hall mobility in the $4 - 50 \text{ K}$ range at various doping levels showed that the main scattering mechanism for electrons is by charged impurities, *i.e.* the oxygen vacancies in the film. Magneto-transport measurements revealed that the same impurities are responsible for the spin relaxation in the system with the observation of a remarkable transition from weak localization to weak anti-localization under certain conditions.

A comparative table is shown in the following resuming the characteristics (in terms of R_S and carrier density) of the graphene and ZnO samples before and after the space charge doping is performed.

| | Undoped | | Doped | |
|----------|----------------------------|----------------------------|----------------------------------|----------------------------------|
| | R_S (Ω/\square) | n_S (cm^{-2}) | $R_{S,min}$ (Ω/\square) | $n_{S,max}$ (cm^{-2}) |
| Graphene | $\sim 10^3$ | $10^{12} - 10^{13}$ | 220 | 1.2×10^{14} |
| ZnO | $10^4 - 10^8$ | $< 10^{13}$ | $\sim 2 \times 10^3$ | 2×10^{14} |

The original work done in this thesis opens new perspectives in the field of fundamental research for the study of the materials in high doping conditions as well as for practical applications like TCE. At the moment, in our laboratory the space charge doping has been successfully used to induce an insulating-to-superconducting transition in few layers MoS₂ samples [139] or in high-temperature superconductors (on-going work). Very interesting informations could be obtained from the samples if Raman spectroscopy could be performed *in situ* in order to monitor, the evolution of the Raman spectrum as a function of doping. This particular equipment has been designed and will be available in our laboratory in the next months.

Regarding potential applications of space charge doping in the future, an interesting way of using our doping method could be by local doping of the samples, *i.e.* by creating space charges of different magnitude and polarity in different areas of the same sample giving the possibility to fabricate, for example, diodes without chemical doping or chips with multiple devices on the same glass substrate. In the field of TCE the work done on ZnO could be improved by working on the crystalline quality of the thin film in order to reach the standard value of resistivity for a TCE of $100 \Omega/\square$. Eventually other oxides like SnO could be investigated. Generally speaking, the performances of space charge doping (both for fundamental research and practical applications) could be improved by working on the quality of the glass substrate. Both ultra-smooth surfaces and a higher Na⁺ content would provide an enhanced doping capability with respect to the glasses studied here.

During this thesis two articles [94, 139] have been published, another is under preparation and industrial patent on space charge doping has been obtained.

List of abbreviations and symbols

| | |
|-------------|---|
| 2D | two-dimensional |
| μ | Charge carriers mobility |
| σ | Conductivity |
| τ | Mean free path time |
| τ_ϕ | Phase coherence time |
| τ_{SO} | Spin relaxation time |
| APS | Ammonium persulfate |
| AFM | Atomic force microscopy |
| B_{tr} | Magnetic field associated to the mean free path |
| B_ϕ | Magnetic field associated to the spin relaxation time |
| B_{SO} | Magnetic field associated to the phase coherence time |
| CVD | Chemical vapour deposition |
| DC | Direct current |
| FET | Field effect transistor |
| FWHM | Full width half maximum |
| G_0 | conductance quantum |
| L_{tr} | Mean free path |
| L_ϕ | Phase coherence length |
| L_{SO} | Spin relaxation length |
| MOSFET | Metal-oxide-semiconductor field effect transistor |
| n_S | Sheet carrier density |
| PMMA | Polymethyl-methacrylate |
| R_H | Hall resistance |
| R_S | Sheet resistance |
| RF | Radio-frequency |
| RMS | Root mean square |
| TCE | Transparent conducting electrode |
| VRH | Variable range hopping |
| XRD | X-ray diffraction |

Bibliography

- [1] T. Ando, A. B. Fowler, and F. Stern. Electronic properties of two-dimensional systems. *Reviews of Modern Physics*, 54(2):437–672, 1982.
- [2] K. S. Novoselov. Electric field effect in atomically thin carbon films. *Science*, 306(5696):666–669, 2004.
- [3] X. Liang, B. A. Sperling, I. Calizo, G. Cheng, C. A. Hacker, Q. Zhang, Y. Obeng, K. Yan, H. Peng, Q. Li, X. Zhu, H. Yuan, A. R. Hight Walker, Z. Liu, L. Peng, and C. A. Richter. Toward clean and crackless transfer of graphene. *ACS Nano*, 5(11):9144–9153, 2011.
- [4] Z. Chen, K. Gacem, M. Boukhicha, J. Biscaras, and A. Shukla. Anodic bonded 2D semiconductors: from synthesis to device fabrication. *Nanotechnology*, 24(41):415708, 2013.
- [5] C. H. Ahn, A. Bhattacharya, M. Di Ventra, J. N. Eckstein, C. D. Frisbie, M. E. Gershenson, A. M. Goldman, I. H. Inoue, J. Mannhart, A. J. Millis, A. F. Morpurgo, D. Natelson, and J.M. Triscone. Electrostatic modification of novel materials. *Reviews of Modern Physics*, 78(4):1185–1212, 2006.
- [6] S. Hurand, A. Jouan, C. Feuillet-Palma, G. Singh, J. Biscaras, E. Lesne, N. Reyren, A. Barthélémy, M. Bibes, J. E. Villegas, C. Ulysse, X. Lafosse, M. Pannetier-Lecoeur, S. Caprara, M. Grilli, J. Lesueur, and N. Bergeal. Field-effect control of superconductivity and Rashba spin-orbit coupling in top-gated LaAlO₃/SrTiO₃ devices. *Scientific Reports*, 5:12751, 2015.
- [7] J. T. Ye, S. Inoue, K. Kobayashi, Y. Kasahara, H. T. Yuan, H. Shimotani, and Y. Iwasa. Liquid-gated interface superconductivity on an atomically flat film. *Nature Materials*, 9(2):125–128, 2010.

-
- [8] S. Das, S. Adam, E. H. Hwang, and E. Rossi. Electronic transport in two-dimensional graphene. *Reviews of Modern Physics*, 83(2):407–470, 2011.
- [9] P. R. Wallace. The band theory of graphite. *Physical Review*, 71(9):622–634, 1947.
- [10] D. R. Cooper, B. D’Anjou, N. Ghattamaneni, B. Harack, M. Hilke, A. Horth, N. Majlis, M. Massicotte, L. Vandsburger, E. Whiteway, and V. Yu. Experimental review of graphene. *ISRN Condensed Matter Physics*, 2012:1–56, 2012.
- [11] C. Mattevi, H. Kim, and M. Chhowalla. A review of chemical vapour deposition of graphene on copper. *Journal of Materials Chemistry*, 21(10):3324–3334, 2011.
- [12] Q. Yu, J. Lian, S. Siriponglert, H. Li, Y. P. Chen, and S. Pei. Graphene segregated on Ni surfaces and transferred to insulators. *Applied Physics Letters*, 93(11):113103, 2008.
- [13] X. Li, W. Zhu, Y. and Cai, M. Borysiak, B. Han, D. Chen, R. D. Piner, L. Colombo, and R. S. Ruoff. Transfer of large-area graphene films for high-performance transparent conductive electrodes. *Nano Letters*, 9(12):4359–4363, 2009.
- [14] S. Bae, H. Kim, Y. Lee, X. Xu, J. Park, Y. Zheng, J. Balakrishnan, T. Lei, H. Ri Kim, Y. I. Song, Y. Kim, K. S. Kim, B. Özyilmaz, J. Ahn, B. H. Hong, and S. Iijima. Roll-to-roll production of 30-inch graphene films for transparent electrodes. *Nature Nanotechnology*, 5(8):574–578, 2010.
- [15] J. Hass, W. A. de Heer, and E. H. Conrad. The growth and morphology of epitaxial multilayer graphene. *Journal of Physics: Condensed Matter*, 20(32):323202, 2008.
- [16] G. Wallis. Field assisted glass-metal sealing. *Journal of Applied Physics*, 40(10):3946, 1969.
- [17] H. Mehrer, A. W. Imre, and E. Tanguet-Nijokep. Diffusion and ionic conduction in oxide glasses. *Journal of Physics: Conference Series*, 106:012001, 2008.
- [18] A. Shukla, R. Kumar, J. Mazher, and A. Balan. Graphene made easy: high quality, large-area samples. *Solid State Communications*, 149(17-18):718–721, 2009.

- [19] A. Balan, Rakesh Kumar, M. Boukhicha, O. Beyssac, J.C. Bouillard, D. Taverna, W. Sacks, M. Marangolo, E. Lacaze, R. Gohler, W. Escoffier, J.M. Poumirol, and A. Shukla. Anodic bonded graphene. *Journal of Physics D: Applied Physics*, 43(37):374013, 2010.
- [20] K. Gacem, M. Boukhicha, Z. Chen, and A. Shukla. High quality 2D crystals made by anodic bonding: a general technique for layered materials. *Nanotechnology*, 23(50):505709, 2012.
- [21] L.M. Malard, M.A. Pimenta, G. Dresselhaus, and M.S. Dresselhaus. Raman spectroscopy in graphene. *Physics Reports*, 473(5-6):51–87, 2009.
- [22] A. C. Ferrari, J. C. Meyer, V. Scardaci, C. Casiraghi, M. Lazzeri, F. Mauri, S. Piscanec, D. Jiang, K. S. Novoselov, S. Roth, and A. K. Geim. Raman spectrum of graphene and graphene layers. *Physical Review Letters*, 97(18):187401, 2006.
- [23] A. Das Sarma, S. Pisana, B. Chakraborty, S. Piscanec, S. K. Saha, U. V. Waghmare, K. S. Novoselov, H. R. Krishnamurthy, A. K. Geim, A. C. Ferrari, and A. K. Sood. Monitoring dopants by Raman scattering in an electrochemically top-gated graphene transistor. *Nature Nanotechnology*, 3(4):210–215, 2008.
- [24] P. Y. Huang, C. S. Ruiz-Vargas, A. M. van der Zande, W. S. Whitney, M. P. Levendorf, J. W. Kevek, S. Garg, J. S. Alden, C. J. Hustedt, Y. Zhu, J. Park, P. L. McEuen, and D. A. Muller. Grains and grain boundaries in single-layer graphene atomic patchwork quilts. *Nature*, 469(7330):389–392, 2011.
- [25] M. Sprinkle, D. Siegel, Y. Hu, J. Hicks, A. Tejada, A. Taleb-Ibrahimi, P. Le Fèvre, F. Bertran, S. Vizzini, H. Enriquez, S. Chiang, P. Soukiassian, C. Berger, W. A. de Heer, A. Lanzara, and E. H. Conrad. First direct observation of a nearly ideal graphene band structure. *Physical Review Letters*, 103(22):226803, 2009.
- [26] A. K. Geim and K. S. Novoselov. The rise of graphene. *Nature Materials*, 6(3):183–191, 2007.
- [27] Y.W. Tan, Y. Zhang, K. Bolotin, Y. Zhao, S. Adam, E. H. Hwang, S. Das, H. L. Stormer, and P. Kim. Measurement of scattering rate and minimum conductivity in graphene. *Physical Review Letters*, 99(24):246803, 2007.
- [28] N. M. R. Peres. The transport properties of graphene. *Journal of Physics: Condensed Matter*, 21(32):323201, 2009.

- [29] S. Adam, E. H. Hwang, V. M. Galitski, and S. Das Sarma. A self-consistent theory for graphene transport. *Proceedings of the National Academy of Sciences*, 104(47):18392–18397, 2007.
- [30] L. Banszerus, M. Schmitz, S. Engels, J. Dauber, M. Oellers, F. Haupt, K. Watanabe, T. Taniguchi, B. Beschoten, and C. Stampfer. Ultra-high mobility graphene devices from chemical vapor deposition on reusable copper. *Science advances*, 1(6):e1500222, 2015.
- [31] K. I. Bolotin, K. J. Sikes, J. Hone, H. L. Stormer, and P. Kim. Temperature-dependent transport in suspended graphene. *Physical Review Letters*, 101(9):096802, 2008.
- [32] H. Wang, T. Taychatanapat, A. Hsu, K. Watanabe, T. Taniguchi, P. Jarillo-Herrero, and T. Palacios. BN/Graphene/BN transistors for RF applications. *IEEE Electron Device Letters*, 32(9):1209–1211, 2011.
- [33] Y. Zhang, Y.W. Tan, H. L. Stormer, and P. Kim. Experimental observation of the quantum Hall effect and Berry’s phase in graphene. *Nature*, 438(7065):201–204, 2005.
- [34] A. Pirkle, J. Chan, A. Venugopal, D. Hinojos, C. W. Magnuson, S. McDonnell, L. Colombo, E. M. Vogel, R. S. Ruoff, and R. M. Wallace. The effect of chemical residues on the physical and electrical properties of chemical vapor deposited graphene transferred to SiO₂. *Applied Physics Letters*, 99(12):122108, 2011.
- [35] C.F. Chen, C.H. Park, B. W. Boudouris, J. Horng, B. Geng, C. Girit, A. Zettl, M. F. Crommie, R. A. Segalman, S. G. Louie, and F. Wang. Controlling inelastic light scattering quantum pathways in graphene. *Nature*, 471(7340):617–620, 2011.
- [36] F. Schwierz. Graphene transistors. *Nature Nanotechnology*, 5(7):487–496, 2010.
- [37] I. Meric, C. R. Dean, N. Petrone, L. Wang, J. Hone, P. Kim, and K. L. Shepard. Graphene field-effect transistors based on boron-nitride dielectrics. *Proceedings of the IEEE*, 101(7):1609–1619, 2013.
- [38] I. Meric, M. Y. Han, A. F. Young, B. Ozyilmaz, P. Kim, and K. L. Shepard. Current saturation in zero-bandgap, top-gated graphene field-effect transistors. *Nature Nanotechnology*, 3(11):654–659, 2008.
- [39] E. Pallecchi, Q. Wilmart, A. C. Betz, S.H. Jhang, G. Fève, J.M. Berroir, S. Lepillet, G. Dambrine, H. Happy, and B. Plaçais. Graphene nanotransistors for RF charge detection. *Journal of Physics D: Applied Physics*, 47(9):094004, 2014.

- [40] L. Wang, X. Chen, Y. Wang, Z. Wu, W. Li, Y. Han, M. Zhang, Y. He, C. Zhu, K. K. Fung, and N. Wang. Modification of electronic properties of top-gated graphene devices by ultrathin yttrium-oxide dielectric layers. *Nanoscale*, 5(3):1116–1120, 2013.
- [41] Y. Wu, C. La-o vorakiat, X. Qiu, J. Liu, P. Deorani, K. Banerjee, J. Son, Y. Chen, E. E. M. Chia, and H. Yang. Graphene terahertz modulators by ionic liquid gating. *Advanced Materials*, 27(11):1874–1879, 2015.
- [42] A. Pachoud, M. Jaiswal, P. K. Ang, K. P. Loh, and B. Özyilmaz. Graphene transport at high carrier densities using a polymer electrolyte gate. *EPL (Europhysics Letters)*, 92(2):27001, 2010.
- [43] H. Park, J. A. Rowehl, K. K. Kim, V. Bulovic, and J. Kong. Doped graphene electrodes for organic solar cells. *Nanotechnology*, 21(50):505204, 2010.
- [44] Y. Shi, K. K. Kim, A. Reina, M. Hofmann, L.J. Li, and J. Kong. Work function engineering of graphene electrode via chemical doping. *ACS Nano*, 4(5):2689–2694, 2010.
- [45] X. Dong, D. Fu, W. Fang, Y. Shi, P. Chen, and L.J. Li. Doping single-layer graphene with aromatic molecules. *Small*, 5(12):1422–1426, 2009.
- [46] L. Qu, Y. Liu, J.B. Baek, and L. Dai. Nitrogen-Doped Graphene as Efficient Metal-Free Electrocatalyst for Oxygen Reduction in Fuel Cells. *ACS Nano*, 4(3):1321–1326, 2010.
- [47] D. Wei, Y. Liu, Y. Wang, H. Zhang, L. Huang, and G. Yu. Synthesis of N-doped graphene by chemical vapor deposition and its electrical properties. *Nano Letters*, 9(5):1752–1758, 2009.
- [48] E. Velez-Fort, C. Mathieu, E. Pallecchi, M. Pigneur, M. G. Silly, R. Belkhou, M. Marangolo, A. Shukla, F. Sirotti, and A. Ouerghi. Epitaxial graphene on 4H-SiC(0001) grown under nitrogen flux: evidence of low nitrogen doping and high charge transfer. *ACS Nano*, 6(12):10893–10900, 2012.
- [49] L. S. Panchakarla, K. S. Subrahmanyam, S. K. Saha, A. Govindaraj, H. R. Krishnamurthy, U. V. Waghmare, and C. N. R. Rao. Synthesis, structure, and properties of boron- and nitrogen-doped graphene. *Advanced Materials*, 21(46), 2009.
- [50] T. Sun, Z. L. Wang, Z. J. Shi, G. Z. Ran, W. J. Xu, Z. Y. Wang, Y. Z. Li, L. Dai, and G. G. Qin. Multilayered graphene used as anode of organic light emitting devices. *Applied Physics Letters*, 96(13):133301, 2010.

- [51] A. Janotti and C. G. Van de Walle. Fundamentals of zinc oxide as a semiconductor. *Reports on Progress in Physics*, 72(12):126501, 2009.
- [52] U. Ozgur, Y. I. Alivov, C. Liu, A. Teke, M. A. Reshchikov, S. Dogan, V. Avrutin, S.J. Cho, and H. Morkoc. A comprehensive review of ZnO materials and devices. *Journal of Applied Physics*, 98(4):041301, 2005.
- [53] T. Minami, Y. Nishi, T. Miyata, and J. Nomoto. High-efficiency oxide solar cells with ZnO/Cu₂O heterojunction fabricated on thermally oxidized Cu₂O sheets. *Applied Physics Express*, 4(6):062301, 2011.
- [54] T. Yamamoto, T. Shiosaki, and A. Kawabata. Characterization of ZnO piezoelectric films prepared by rf planar-magnetron sputtering. *Journal of Applied Physics*, 51(6):3113, 1980.
- [55] X. Jiang, F. L. Wong, M. K. Fung, and S. T. Lee. Aluminum-doped zinc oxide films as transparent conductive electrode for organic light-emitting devices. *Applied Physics Letters*, 83(9):1875, 2003.
- [56] W. Water and S.Y. Chu. Physical and structural properties of ZnO sputtered films. *Materials Letters*, 55(1-2):67–72, 2002.
- [57] Y. Natsume and H. Sakata. Zinc oxide films prepared by sol-gel spin-coating. *Thin Solid Films*, 372(1-2):30–36, 2000.
- [58] L. Znaidi. Sol-gel-deposited ZnO thin films: A review. *Materials Science and Engineering: B*, 174(1-3):18–30, 2010.
- [59] Y. T. Prabhu, K. V. Rao, V. S. S. Kumar, and B. S. Kumari. Synthesis of ZnO nanoparticles by a novel surfactant assisted amine combustion method. *Advances in Nanoparticles*, 02(01):45–50, 2013.
- [60] E. M. C. Fortunato, P. M. C. Barquinha, A. C. M. B. G. Pimentel, A. M. F. Gonçalves, A. J. S. Marques, L. M. N. Pereira, and R. F. P. Martins. Fully transparent ZnO thin-film transistor produced at room temperature. *Advanced Materials*, 17(5):590–594, 2005.
- [61] P. F. Carcia, R. S. McLean, M. H. Reilly, and G. Nunes. Transparent ZnO thin-film transistor fabricated by rf magnetron sputtering. *Applied Physics Letters*, 82(7):1117, 2003.
- [62] M. Chen, Z. L. Pei, X. Wang, C. Sun, and L. S. Wen. Structural, electrical, and optical properties of transparent conductive oxide ZnO:Al films prepared by dc magnetron reactive sputtering. *Journal of Vacuum Science & Technology A: Vacuum, Surfaces, and Films*, 19(3):963, 2001.

- [63] E. M. C. Fortunato, P. M. C. Barquinha, A. C. M. B. G. Pimentel, A. M. F. Gonçalves, A. J. S. Marques, R. F. P. Martins, and L. M. N. Pereira. Wide-bandgap high-mobility ZnO thin-film transistors produced at room temperature. *Applied Physics Letters*, 85(13):2541, 2004.
- [64] E. Ziegler, A. Heinrich, H. Oppermann, and G. Stöver. Electrical properties and non-stoichiometry in ZnO single crystals. *Physica Status Solidi (a)*, 66(2):635–648, 1981.
- [65] J. C. Simpson and J. F. Cordaro. Defect clusters in zinc oxide. *Journal of Applied Physics*, 67(11):6760, 1990.
- [66] A. Janotti and C. G. Van de Walle. Oxygen vacancies in ZnO. *Applied Physics Letters*, 87(12):122102, 2005.
- [67] T. Minami, H. Nanto, and S. Takata. Highly conductive and transparent aluminum-doped zinc oxide thin films prepared by RF magnetron sputtering. *Japanese Journal of Applied Physics*, 23(Part 2, No. 1):L280–L282, 1984.
- [68] B.Y. Oh, M.C. Jeong, T.H. Moon, W. Lee, J.M. Myoung, J.Y. Hwang, and D.S. Seo. Transparent conductive Al-doped ZnO films for liquid crystal displays. *Journal of Applied Physics*, 99(12):124505, 2006.
- [69] R. L. Hoffman, B. J. Norris, and J. F. Wager. ZnO-based transparent thin-film transistors. *Applied Physics Letters*, 82(5):733, 2003.
- [70] H. Yuan, H. Shimotani, A. Tsukazaki, A. Ohtomo, M. Kawasaki, and Y. Iwasa. High-density carrier accumulation in ZnO field-effect transistors gated by electric double layers of ionic liquids. *Advanced Functional Materials*, 19(7):1046–1053, 2009.
- [71] H. Yuan, H. Shimotani, J. Ye, S. Yoon, H. Aliah, A. Tsukazaki, M. Kawasaki, and Y. Iwasa. Electrostatic and electrochemical nature of liquid-gated electric-double-layer transistors based on oxide semiconductors. *Journal of the American Chemical Society*, 132(51):18402–18407, 2010.
- [72] A. Goldenblum, V. Bogatu, T. Stoica, Y. Goldstein, and A. Many. Weak localization effects in ZnO surface wells. *Physical Review B*, 60(8):5832–5838, 1999.
- [73] Y. Shapira. Anomalous effect of UHV-component-generated atomic hydrogen on the surface properties of ZnO. *Journal of Vacuum Science and Technology*, 13(2):615, 1976.

- [74] G. Yaron, A. Many, and Y. Goldstein. Quantized electron accumulation layers on ZnO surfaces produced by low-energy hydrogen-ion implantation. *Journal of Applied Physics*, 58(9):3508, 1985.
- [75] Y. Goldstein, A. Many, D. Eger, Y. Grinshpan, G. Yaron, and M. Nitzan. Extreme accumulation layers on ZnO surfaces due to He⁺ ions. *Physics Letters A*, 62(1):57–58, 1977.
- [76] C. Lü and J. L. Cheng. Spin relaxation in n -type ZnO quantum wells. *Semiconductor Science and Technology*, 24(11):115010, 2009.
- [77] F. Reuss, S. Frank, C. Kirchner, R. Kling, Th. Gruber, and A. Waag. Magnetoresistance in epitaxially grown degenerate ZnO thin films. *Applied Physics Letters*, 87(11):112104, 2005.
- [78] T. Andrearczyk, J. Jaroszyński, G. Grabecki, T. Dietl, T. Fukumura, and M. Kawasaki. Spin-related magnetoresistance of n-type ZnO:Al and Zn_{1-x}Mn_xO:Al thin film. *Physical Review B*, 72(12):121309, 2005.
- [79] R. Anthony, T. Anodic bonding of imperfect surfaces. *Journal of Applied Physics*, 54(5):2419, 1983.
- [80] T. Moldt, A. Eckmann, P. Klar, S. V. Morozov, A. A. Zhukov, K. S. Novoselov, and C. Casiraghi. High-Yield production and transfer of graphene flakes obtained by anodic bonding. *ACS Nano*, 5(10):7700–7706, 2011.
- [81] J. W. Suk, A. Kitt, C. W. Magnuson, Y. Hao, S. Ahmed, J. An, A. K. Swan, B. B. Goldberg, and R. S. Ruoff. Transfer of CVD-grown monolayer graphene onto arbitrary substrates. *ACS Nano*, 5(9):6916–6924, 2011.
- [82] G. Jo. Etching solution for etching Cu and Cu/Ti metal layer of liquid crystal display device and method of fabricating the same. *US Patent*, 6,881,679, 2005.
- [83] I.S. Kim, S.H. Jeong, S. S. Kim, and B.-T. Lee. Magnetron sputtering growth and characterization of high quality single crystal ZnO thin films on sapphire substrates. *Semiconductor Science and Technology*, 19(3):L29–L31, 2004.
- [84] G. Binnig and C. F. Quate. Atomic force microscope. *Physical Review Letters*, 56(9):930–933, 1986.
- [85] E. Meyer. Atomic force microscopy. *Progress in Surface Science*, 41(1):3–49, 1992.

- [86] C. V. Raman. A new radiation. *Indian Journal of Physics*, (2):387–398, 1928.
- [87] P. Larkin. *Infrared and Raman Spectroscopy: Principles and Spectral Interpretation*. Elsevier Inc., 2011.
- [88] A. L. Patterson. The Scherrer formula for X-ray particle size determination. *Physical Review*, 56(10):978–982, 1939.
- [89] D. Simeone, G. Baldinozzi, D. Gosset, S. Le Caer, and J.F. Bérrar. Grazing incidence X-ray diffraction for the study of polycrystalline layers. *Thin Solid Films*, 530:9–13, 2013.
- [90] L. J. van der Pauw. A method of measuring specific resistivity and Hall effect of discs of arbitrary shape. *Philips Technical Review*, 20:220–224, 1958.
- [91] T. J. B. M. Janssen, A. Tzalenchuk, S. Lara-Avila, S. Kubatkin, and V. I. Fal’ko. Quantum resistance metrology using graphene. *Reports on Progress in Physics*, 76(10):104501, 2013.
- [92] S. Pang, Y. Hernandez, X. Feng, and K. Müllen. Graphene as transparent electrode material for organic electronics. *Advanced Materials*, 23(25):2779–2795, 2011.
- [93] O. Kluth, B. Rech, L. Houben, S. Wieder, G. Schöpe, C. Beneking, H. Wagner, A. Löffl, and H. W. Schock. Texture etched ZnO:Al coated glass substrates for silicon based thin film solar cells. *Thin Solid Films*, 351(1-2):247–253, 1999.
- [94] A. Paradisi, J. Biscaras, and A. Shukla. Space charge induced electrostatic doping of two-dimensional materials: Graphene as a case study. *Applied Physics Letters*, 107(14):143103, 2015.
- [95] W. H. Zachariasen. The atomic arrangement in glass. *Journal of the American Chemical Society*, 54(10):3841–3851, 1932.
- [96] Xuan Wang, Linjie Zhi, and Klaus Müllen. Transparent, conductive graphene electrodes for dye-sensitized solar cells. *Nano Letters*, 8(1):323–327, 2008.
- [97] J. Wu, H. A. Becerril, Z. Bao, Z. Liu, Y. Chen, and P. Peumans. Organic solar cells with solution-processed graphene transparent electrodes. *Applied Physics Letters*, 92(26):263302, 2008.
- [98] P. Blake, E. W. Hill, A. H. Castro Neto, K. S. Novoselov, D. Jiang, R. Yang, T. J. Booth, and A. K. Geim. Making graphene visible. *Applied Physics Letters*, 91(6):063124, 2007.

- [99] M. Sprinkle, M. Ruan, Y. Hu, J. Hankinson, M. Rubio-Roy, B. Zhang, X. Wu, C. Berger, and W. A. De Heer. Scalable templated growth of graphene nanoribbons on SiC. *Nature Nanotechnology*, 5(10):727–731, 2010.
- [100] D. S. Hecht, L. Hu, and G. Irvin. Emerging transparent electrodes based on thin films of carbon nanotubes, graphene, and metallic nanostructures. *Advanced Materials*, 23(13):1482–1513, 2011.
- [101] M. Kalbac, A. Reina-Cecco, H. Farhat, J. Kong, L. Kavan, and M. S. Dresselhaus. The influence of strong electron and hole doping on the Raman intensity of chemical vapor-deposition graphene. *ACS Nano*, 4(10):6055–6063, 2010.
- [102] A.E. Jiménez-González, J. A. Soto Urueta, and R. Suárez-Parra. Optical and electrical characteristics of aluminum-doped ZnO thin films prepared by solgel technique. *Journal of Crystal Growth*, 192(3-4):430–438, 1998.
- [103] Y. Min. *Properties and sensor performance of zinc oxide thin films*. PhD thesis, Massachusetts Institute of Technology, 2003.
- [104] D.F. Wang, Y. Ying, V.T.T. Thuy, J.M. Kim, M.S. Seo, F. Gao, T.J. Zhang, K.W. Kim, and Y.P. Lee. Temperature-dependent magnetoresistance of ZnO thin film. *Thin Solid Films*, 520(1):529–532, 2011.
- [105] A. a Mosquera, D. Horwat, A. Rashkovskiy, A. Kovalev, P. Miska, D. Wainstein, J. M Albella, and J. L. Endrino. Exciton and core-level electron confinement effects in transparent ZnO thin films. *Scientific Reports*, 3:1714, 2013.
- [106] M. Tzolov, N. Tzenov, D. Dimova-Malinovska, M. Kalitzova, C. Pizzuto, G. Vitali, G. Zollo, and I. Ivanov. Vibrational properties and structure of undoped and Al-doped ZnO films deposited by RF magnetron sputtering. *Thin Solid Films*, 379(1-2):28–36, 2000.
- [107] A. T. Vai, V. L. Kuznetsov, H. Jain, D. Slocombe, N. Rashidi, M. Pepper, and P. P. Edwards. The transition to the metallic state in polycrystalline n-type doped ZnO thin films. *Zeitschrift für anorganische und allgemeine Chemie*, 640(6):1054–1062, 2014.
- [108] D. H. Zhang and H. L. Ma. Scattering mechanisms of charge carriers in transparent conducting oxide films. *Applied Physics A Materials Science and Processing*, 62(5):487–492, 1996.
- [109] R. L. Petritz. Theory of photoconductivity in semiconductor films. *Physical Review*, 104(6):1508–1516, 1956.

- [110] K. Ellmer and R. Mientus. Carrier transport in polycrystalline transparent conductive oxides: a comparative study of zinc oxide and indium oxide. *Thin Solid Films*, 516(14):4620–4627, 2008.
- [111] S. A. Agnihotry, K. K. Saini, T. K. Saxena, K. C. Nagpal, and S. Chandra. Studies on e-beam deposited transparent conductive films of In₂O₃:Sn at moderate substrate temperatures. *Journal of Physics D: Applied Physics*, 18(10):2087–2096, 1985.
- [112] S. Bansal, S. C. Kashyap, and D. K. Pandya. Metal-semiconductor transition and negative magneto-resistance in degenerate ultrathin tin oxide films. *Journal of Alloys and Compounds*, 646:483–489, 2015.
- [113] N. Mott. Conductivity, localization, and the mobility edge. *The Physics of Hydrogenated Amorphous Silicon II*, pages 169–193, 1984.
- [114] P. W. Anderson. Absence of diffusion in certain random lattices. *Physical Review*, 109(5):1492–1505, 1958.
- [115] N. Mott, M. Pepper, S. Pollitt, R. H. Wallis, and C. J. Adkins. The Anderson transition. *Proceedings of the Royal Society A: Mathematical, Physical and Engineering Sciences*, 345(1641):169–205, 1975.
- [116] N. Mott. The mobility edge since 1967. *Journal of Physics C: Solid State Physics*, 20(21):3075–3102, 1987.
- [117] Y.L. Huang, S.P. Chiu, Z.X. Zhu, Z.Q. Li, and J.J. Lin. Variable-range-hopping conduction processes in oxygen deficient polycrystalline ZnO films. *Journal of Applied Physics*, 107(6):063715, 2010.
- [118] T. T. Lin, S. L. Young, C. Y. Kung, H. Z. Chen, M. C. Kao, M. C. Chang, and C. R. Ou. Variable range hopping and thermal activation conduction of Y-doped ZnO nanocrystalline films. *IEEE Transactions on Nanotechnology*, 13(3):425–430, 2014.
- [119] J. Han, M. Shen, W. Cao, A. M. R. Senos, and P. Q. Mantas. Hopping conduction in Mn-doped ZnO. *Applied Physics Letters*, 82(1):67, 2003.
- [120] M. C. Prestgard, G. Siegel, R. Roundy, M. Raikh, and A. Tiwari. Temperature dependence of the spin relaxation in highly degenerate ZnO thin films. *Journal of Applied Physics*, 117(8):083905, 2015.
- [121] J. Y. Fu and M. W. Wu. Spin-orbit coupling in bulk ZnO and GaN. *Journal of Applied Physics*, 104(9):093712, 2008.
- [122] N. J. Harmon, W. O. Putikka, and R. Joynt. Theory of electron spin relaxation in ZnO. *Physical Review B*, 79(11):115204, 2009.

- [123] W. K. Liu, K. M. Whitaker, A. L. Smith, K. R. Kittilstved, B. H. Robinson, and D. R. Gamelin. Room-temperature electron spin dynamics in free-standing ZnO quantum dots. *Physical Review Letters*, 98(18):186804, 2007.
- [124] S. Ghosh, V. Sih, W. H. Lau, D. D. Awschalom, S.Y. Bae, S. Wang, S. Vaidya, and G. Chapline. Room-temperature spin coherence in ZnO. *Applied Physics Letters*, 86(23):232507, 2005.
- [125] A. V. Germanenko. Spin effects and quantum corrections to the conductivity of two-dimensional systems. *Low Temperature Physics*, 35(1):24, 2009.
- [126] P. A. Lee and T. V. Ramakrishnan. Disordered electronic systems. *Reviews of Modern Physics*, 57(2):287–337, 1985.
- [127] A. Sommerfeld and N. H. Frank. The statistical theory of thermoelectric, galvano- and thermomagnetic phenomena in metals. *Reviews of Modern Physics*, 3(1):1–42, 1931.
- [128] S. Hikami, A. I. Larkin, and Y. Nagaoka. Spin-orbit interaction and magnetoresistance in the two dimensional random system. *Progress of Theoretical Physics*, 63(2):707–710, 1980.
- [129] S. Maekawa and H. Fukuyama. Magnetoresistance in two-dimensional disordered systems: effects of Zeeman splitting and spin-orbit scattering. *Journal of the Physical Society of Japan*, 50(8):2516–2524, 1981.
- [130] G.E. Iordanskii, S.V. and Lyanda-Geller, Y. B. and Pikus. Weak localization in quantum wells with spin-orbit interaction. *JETP Letters*, 60:199, 1994.
- [131] A. D. Caviglia, M. Gabay, S. Gariglio, N. Reyren, C. Cancellieri, and J.M. Triscone. Tunable Rashba spin-orbit interaction at oxide interfaces. *Physical Review Letters*, 104(12):126803, 2010.
- [132] Hadis Morkoç and Ümit Özgür. *Zinc oxide: fundamentals, materials and device technology*. John Wiley & Sons, 2008.
- [133] G. Giuliani. A general law for electromagnetic induction. *EPL (Europhysics Letters)*, 81(6):60002, 2008.
- [134] S. M. Choo, K. J. Lee, S. M. Park, J. B. Yoon, G. S. Park, C.Y. You, and M. H. Jung. Crossover between weak anti-localization and weak localization by Co doping and annealing in gapless PbPdO₂ and spin gapless Co-doped PbPdO₂. *Applied Physics Letters*, 106(17):172404, 2015.

-
- [135] I. Žutić, J. Fabian, and S. Das Sarma. Spintronics: Fundamentals and applications. *Reviews of Modern Physics*, 76(2):323–410, 2004.
- [136] Y. a Bychkov and E. I. Rashba. Oscillatory effects and the magnetic susceptibility of carriers in inversion layers. *Journal of Physics C: Solid State Physics*, 17(33):6039–6045, 1984.
- [137] R. J. Elliott. Theory of the effect of spin-orbit coupling on magnetic resonance in some semiconductors. *Physical Review*, 96(2):266–279, 1954.
- [138] S. Das Sarma and E. H. Hwang. Two-dimensional metal-insulator transition as a strong localization induced crossover phenomenon. *Physical Review B*, 89(23):235423, 2014.
- [139] J. Biscaras, Z. Chen, A. Paradisi, and A. Shukla. Onset of two-dimensional superconductivity in space charge doped few-layer molybdenum disulfide. *Nature Communications*, 6, 2015.